Doctoral Thesis

Rational Design of Swelling-suppression in Silicon Anode for Lithium-ion Battery

Taesoo Bok

Department of Energy Engineering

(Battery Science and Technology)

Graduate School of UNIST

2018

Rational Design of Swelling-suppression in Silicon Anode for Lithium-ion Battery

Taesoo Bok

Department of Energy Engineering
(Battery Science and Technology)

Graduate School of UNIST

Rational Design of Swelling-suppression in Silicon Anode for Lithium-ion Battery

A thesis/dissertation
submitted to the Graduate School of UNIST
in partial fulfillment of the
requirements for the degree of
Doctor of Philosophy

Taesoo Bok

11/29/2017

Approved by

Advisor
Soojin Park

Rational Design of Swelling-suppression in Silicon Anode for Lithium-ion Battery

Taesoo Bok

This certifies that the thesis/dissertation of Taesoo Bok is approved.

11/29/2017

signature

Advisor: Soojin Park

signature

Prof. Sang-Young Lee

signature

Prof. Hyun-Kon Song

signature

Prof. Nam-Soon Choi

signature

Prof. Ja-Hyoung Ryu

Abstract

To make provision for the depletion of fossil fuel, energy storage system (ESS) plays an important role as much as energy conversion devices. As recent energy consumption significantly increases, it is necessary to prepare energy shortage in advance. ESS exists in various forms such as thermal, chemical, mechanical, and electromagnetic storage system. Among numerous chemical storage devices, lithium-ion batteries (LIBs) have been used from mobile to electric vehicles owing to their suitable energy and power density. However, as the needs of battery are increasing every year, the present system should be systematically changed for longer use. In this situation, silicon (Si) as an anode material in LIBs is one of the most promising materials owing to its high theoretical capacity, low reduction potential, and earth-abundant material, if disadvantages of Si such as volume expansion and low kinetics can be controlled. To overcome the limitation of Si to commercialize, rational design of Si is required.

Herein, we focus on the material design and engineering to enhance the electrochemical performance of Si anodes. We mainly deal with chemical synthesis, characterization based on the advanced analysis tools, and evaluation from various methods. In case of Si synthesis, it is an acceptable approach that the length of Li^+ diffusion path should be shortened for fast kinetic parameters. It means that Si can be available after nanostructuring such as thermochemical reduction and chemical-vapor deposition (CVD). In addition, ionic diffusivity and electric conductivity should increase by making the composite such as coating and mixture, delivering the high coulombic efficiency. For the precise analysis, structural evolution during lithiation/delithiation is confirmed through the X-ray diffraction (XRD), photoelectron spectroscopy (XPS), Fourier transform infrared (FT-IR), Raman, EXAFS, and *in-situ* transmission electron microscopy (TEM), electrochemical impedance spectroscopy (EIS), differential electrochemical mass spectroscopy (DEMS). Moreover, electrochemical evaluation is contained such as *b*-value calculation *via* cyclic voltammetry (CV), operating voltage cut-off for understanding the redox couples.

In chapter II, we introduce a cross-linked polymeric binder for Si anode. The binder consists of two different polymers, in which one acts as the crosslinking agent while the other plays a role in providing the stability on Si surface after making the electrode. The binder has a high mechanical strength, resulting in the effective support to endure the stress derived from the lithiation on Si.

In chapter III, we present a gel polymer electrolyte (GPE) substituted for liquid one in LIB. The concept of this theme is that the GPE can provide the safety in the cell and act as mechanical

buffer to the expanded Si. Moreover, its mechanical property is confirmed through the long-term electrochemical test.

In chapter IV, we introduce two-dimensional Si (2D Si) as LIB anode material. In this system, 2D Si has nano-scaled thickness and a micro-scaled width. The thin layer delivers the fast kinetics, while spacious area provides a low surface area for high initial coulombic efficiency (ICE). Besides, carbon-coated 2D Si shows the unique electrochemical behavior which indicates the development of wrinkle surface after delithiation. Through the *in-situ* TEM, EIS and computational study in parallel, we demonstrate why the 2D Si@C is electrochemically good.

In chapter V, we introduce 3D Si with numerous pores as an anode material. Porous Si is synthesized from porous silica made of block-copolymer and silica precursor *via* thermochemical reduction. Furthermore, electrochemical performance can be improved by using the control of heat generated from exothermic reaction.

In chapter VI, we also demonstrate 3D Si with hollow and porous structure. It derived from metal-organic framework (MOF) such as nanocube type of ZIF-8. After silica coating, reduction into Si, and etching the MOF template, hollow Si nanocube is synthesized. The thermochemical reduction is applied for providing the mesopores into the sample without any changes in morphology. The inner void and pores can alleviate the stress by providing the available space to be expanded.

In chapter VII, we newly design the new concept of Si and C composite. Apart from the conventional Si/C composite such as physical blending, graphene-encapsulated Si, and carbon coating on Si, Si atom is surrounded with C atoms, forming amorphous phase. The randomly distribution of Si and C shows its own electrochemical performance unlike blending system or coating system. The amorphous Si-C bonding is broken at deep lithiation like a hetero-fission, then at delithiation step, Si clusters are formed to deliver additional capacities while C frames remain for fast kinetics. These kinds of phenomena are analyzed through the *in-situ* TEM, *ex-situ* EXAFS, and ReaxFF-MD simulation.

Contents

List of figures

List of tables

Nomenclature

0D Si	0-dimensional Si
1D Si	1-dimensional Si
2D Si	2-dimensional Si
3D Si	3-dimensional Si
BET	Brunauer-Emmett-Teller analysis
BPO	benzoyl peroxide
C_2H_2	acetylene gas
CE	coulombic efficiency
CMC	sodium carboxymethyl cellulose
CSM	continuous stiffness measurement
CTAB	(1-Hexadecyl)trimethylammonium bromide
CVD	chemical vapor deposition
DEC	diethyl carbonate
DEMS	differential electrochemical mass spectroscopy
DI water	deionized water
EC	ethylene carbonate
EDX	energy-dispersive X-ray spectroscopy
EIS	electrochemical impedance spectroscopy
ESS	energy storage system
ETEM	environmental transmission electron microscopy
EtOH	ethanol
ETPTA	trimethylopropane triacrylate
EVs	electric vehicles
EXAFS	extended X-ray absorption fine structure
FEC	fluoroethylene carbonate
FFT	fast Fourier transform
FT-IR	Fourier transform infrared
GPC	gel permeation chromatography
GPE	gel polymer electrolytes
HCl	hydrochloric acid
HMIM	2-Methylimidazole
HR-TEM	high resolution transmission electron microscopy
ICE	initial coulombic efficiency

LCO	$LiCoO_2$
LFP	$LiFePO_4$
LIB	Lithium-ion battery
Li-PAA	lithium polyacrylate
$LiPF_6$	lithium hexafluorophosphate
LMO	$LiMn_2O_4$
LTO	$Li_4Ti_5O_{12}$
MeOH	methanol
MOFs	metal-organic frameworks
MRR	magnesiothermic reduction reaction
m-Si HC	mesoporous Si hollow nanocube
MWCOs	molecular weight cut-offs
NMP	N-methyl Pyrrolinone
PAA	poly(acrylic acid)
PC	polycarbonate
PEO	poly(ethylene oxide)
PPO	poly(propylene oxide)
PVdF	poly(vinylidene fluoride)
PVdF-TFP	poly(vinylidene fluoride-tetrafluoroethylene-propylene)
SAED	selected area electron diffraction
SBR	styrene-butadiene rubber
SEI	solid-electrolyte-interface
SEM	scanning electron microscopy
Si HC	Si hollow nanocube
SiNP	Si nanoparticle
SINW	Si nanowire
SOC	state -of-charge
SSNMR	solid-state nuclear magnetic resonance
STEM	scanning/transmission electron microscope
TBA-TEVS	poly(*tert*-butyl acrylate-*co*-triethoxyvinylsilane)
TEM	transmission electron microscopy
TEOS	tetraethyl orthosilicate
TMS	tetramethylsilane
TMS	transition metal
XPS	X-ray photoelectron spectroscopy

XRD	X-ray diffraction
ZIF-8 NC	ZIF-8 nanocube
ZnO@SiO_2 HC	ZnO@SiO_2 hollow nanocube

1. Introduction

1.1 Lithium-ion battery in ESS

The global energy market has been focusing on research related to energy conversion technology, as it promotes the development of alternative materials for fossil fuels[1-4]. In specific, there are examples such as traditional wind turbines, solar cell, biomass, hydroelectric, geothermal system, rising tidal and wave generators[5]. Likewise, studies of energy storage system (ESS) have progressed a lot as much as conversion system. ESS can be classified into 4 groups: thermal[6-8], chemical[9-12], mechanical[13-15], and electromagnetic storage[16,17] according to energy sources. Additionally, ESS is available to each application due to its own storage mechanism, such as response time and duration.

Among them, lithium-ion batteries (LIBs) are one of the great success on energy storage technology based on the combination of high energy and power density for portable electronics, power tools, and electric vehicles[9,18,19]. The LIBs have several advantages over other devices. First, Li is the lightest metal and the smallest in the single charged ion in periodic table, exhibiting with high gravimetric/volumetric capacity, and high-power density. Second, Li has the lowest standard reduction potential, resulting in higher cell potential and energy density[18]. Finally, there is little memory effect that is a critical problem in Ni-Cd battery[20].

LIB cell has four main ingredients such as cathode, anode, electrolyte and separator. The principle of charging is as follows: Li-ion migrates from cathode through the electrolyte into anode, and meets electron from the current collector to make charge neutrality during charge, then reverse reaction happens on discharge process. Since the capacity is determined from the amount of lithiation into electrode material, these materials should be selected to store a lot of Li^+, be able to respond quickly, and move fast.

The cathode materials mainly stored guest Li^+ in the host network, and removed reversibly. The compounds for the host materials are transition metal oxides and polyanions; detailed layered structure, spinel and olivine structure. $LiCoO_2$ (LCO) is firstly introduced and successfully commercialized as a layered transition metal oxide for mobile and portable devices[21,22], while $LiMn_2O_4$ (LMO), or $LiFePO_4$ (LFP) has been focused for EV application due to the cost, high voltage cutoff and safety[23, 24]. However, all of them have a limitation due to the low gravimetric capacity under 180 mAh g^{-1}. Therefore, Li-rich cathode for high energy density, Ni-rich material

for high power density and Mn-rich cathode for safety have been developed every year[25-27].

In case of anode, carbonaceous materials are firstly introduced and commercialized at the early stage of LIB such as graphite and hard carbon. The graphite delivers about 372 mAh g^{-1}, and offers good electric conductivity, chemical stability, and Li^+ transport[28]. However, the capacity of graphite is too low, compare to materials which can alloy with Li^+ such as other IV group elements in periodic table except for carbon. For the next-generation LIB, the anode material with high energy density should be developed as well as new battery system (e.g. flexible, wearable, stretchable and deformable property).

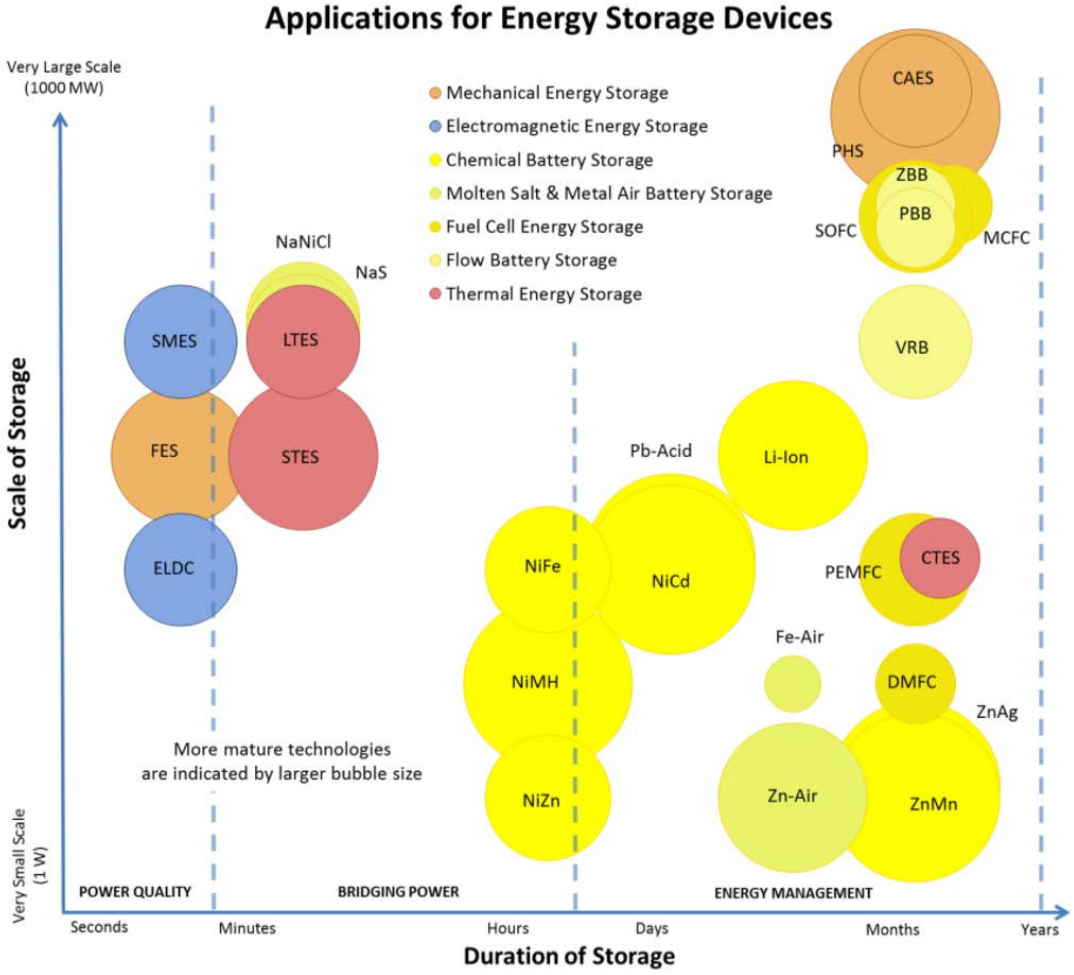

Figure 1-1. A schematic diagram of specific applications for which storage technologies[5]

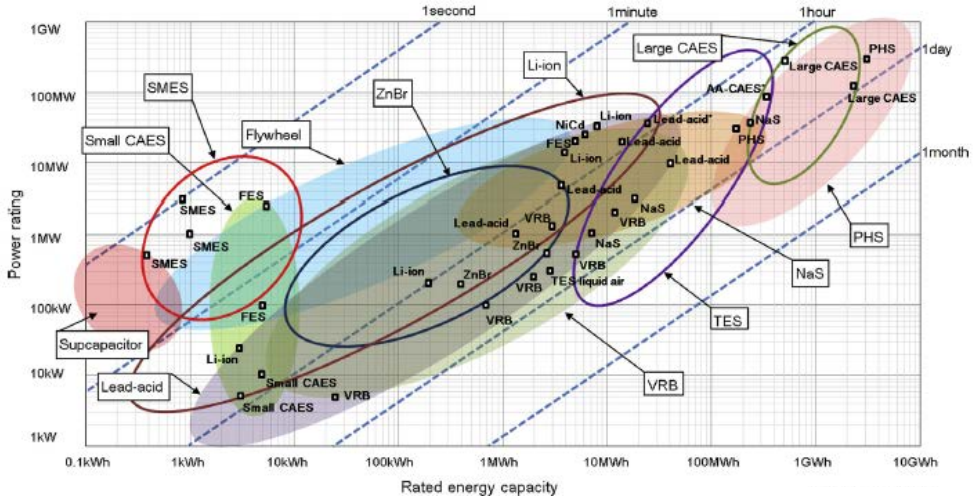

Figure 1-2. Comparison power rating and rated energy capacity with discharge time duration at power rating[1].

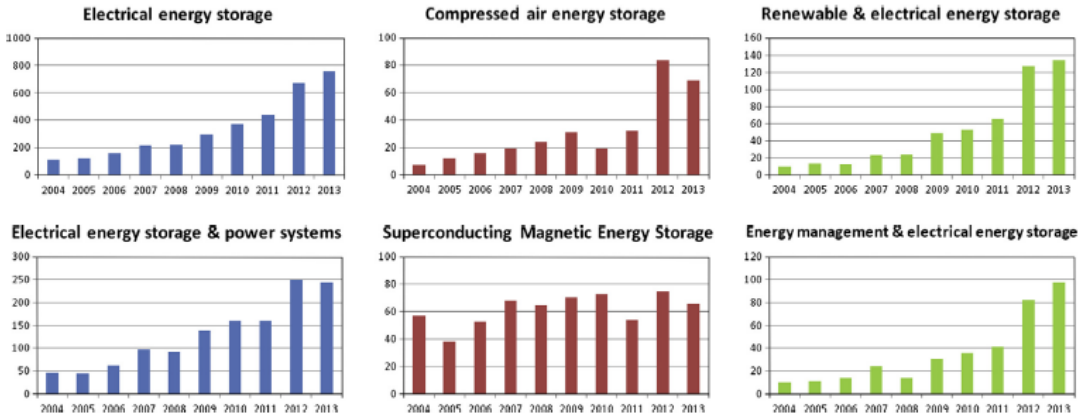

Figure 1-3. A brief statistical study to the trend in ESS related research.

1.2 Anode material for LIB

Anode materials are generally divided into three categories as a function of lithiation mechanism: (de)intercalation, (de)alloying, and conversion reaction.

(De)intercalation materials: graphite, $Li_4Ti_5O_{12}$ (LTO)

Graphite is a good example for introducing the intercalation mechanism of Li^+ into host network. It is generally known that the solvated Li^+ passes through the gap between graphene layers, and reacts with 6 carbon atoms, forming LiC_6 and delivering 372 mAh g^{-1}. [29] Although graphite is firstly commercialized based on the stability in chemical thermal and mechanical, abundant availability, low cost and reduction potential, high Li^+ diffusivity and electric conductivity, and low volume change during cycle. Graphite is not recommended for usage in polycarbonate(PC)-based electrolyte since the PC intercalated into graphite with together Li^+, causing the exfoliation of graphite and capacity fading. In order to defend the vulnerable edge plane from PC and obtain high Coulombic efficiency (CE), the amorphous carbon is coated on graphitic carbon. [30-32]

Hard carbon has graphitic regions with disordered orientation due to the low synthetic temperature under 1000 ºC. It also has nanovoid between grains, providing the additional gravimetric capacity. Its lithiation mechanism follows the Li physiosorption on the void or defect, rather than intercalation, while LiC_6 is formed in graphitic grains. [33,34]

LTO is an attractive anode material owing to the superior stability in mechanical and electrochemical, and fast Li^+ diffusivity into host network. [35] The voltage plateau is about 1.7 V (vs. Li/Li^+), exhibiting the 175 mAh g^{-1} of reversible capacity. In general, as carbonate-based electrolytes are decomposed under 1.2 V, there is no SEI layer on LTO surface. Moreover, the host network of oxides is enough for reversible transport of Li^+, leading to no volume change. Based on LTO chemistries, it can be used for fast charging devices, rather than high-energy density application. [36]

(De)alloying materials: Si, Ge, Sn, etc.

Si, Ge, Sn, Sb and Al are the representative examples for alloying lithiation mechanism.[37-39] The formation of Li_xM can deliver higher specific capacity than materials with other mechanisms, but lead to a serious volume expansion. In this matter, Si is promising materials among them due

to the high theoretical capacity (3572 mAh g^{-1} for gravimetric, 8334 mAh cc^{-1} for volumetric capacity).[38] Si also has additional advantages such as low reduction potential about <0.4 V (vs Li/Li^+), and earth abundant. However, Si is expanded to ~300% in volume, leading to crack, pulverization, and the resulting capacity fading. Moreover, electric conductivity is lower than other active materials. Although Ge shows better electrochemical behavior during cycle (higher conductivity, 1384 mAh g^{-1}, 7366 mAh cc^{-1}), it suffered from ~250% of volume expansion, and tin as well[38]. To overcome these common problems in alloying materials, many researchers have concentrated on the part through experimental and computational study. The nanostructuring of Si may be helpful to reduce the volume expansion. Also, various applications, such as composite, doping, coating, and morphology control, can be combined together.

Conversion materials: Mn_xO, NiO, Fe_2O_3, Co_3O_4, Cu_xO, SnO_2, …

In general, transition metal (TM) oxides can react with Li^+, forming the Li_2O + TM *via* conversion reaction[39-45]. It is well known for developing this approach to use oxides where Li_2O is formed during lithiation. The Li_2O itself can be active materials when the operating voltage is considerably widened, alloying with the transition metals such as MnO[40]. Although this method can reduce the loss of irreversible capacity, potential gap between anode and cathode decreased. Likewise, transition metal oxides deliver ~1000 mAh g^{-1}, but they cannot realize high energy density anode due to the high reduction potential ~1 V. [39-42] In addition, the consumption of Li^+ is high on 1st lithiation between the general voltage windows. Thus, the nanostructured design causing fast kinetics is essential in this system to obtain the more charge capacity.

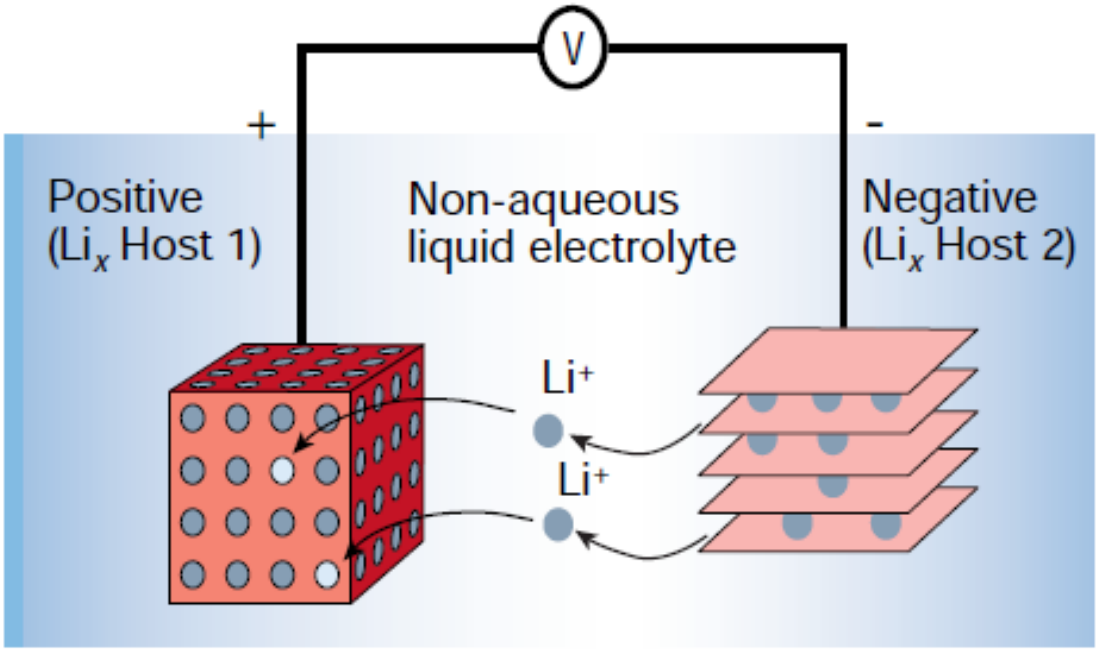

Figure 1-4. Schematic representation and operating principles of Li rechargeable batteries.[9]

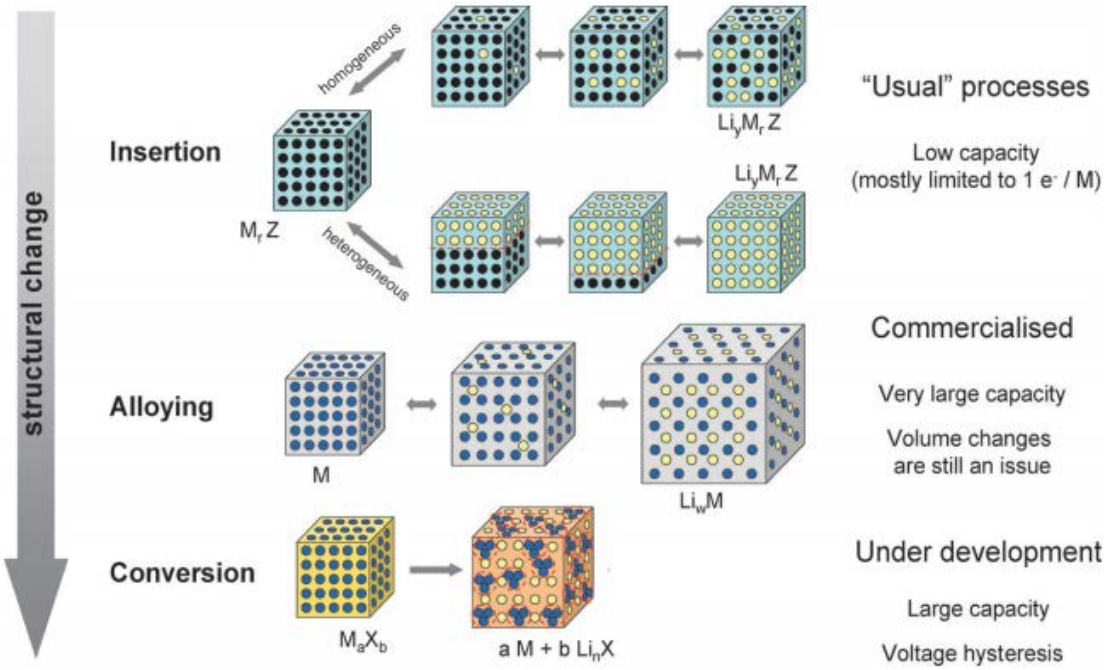

Figure 1-5. A schematic representation of the different reaction mechanism observed in electrode materials for lithium batteries[64].

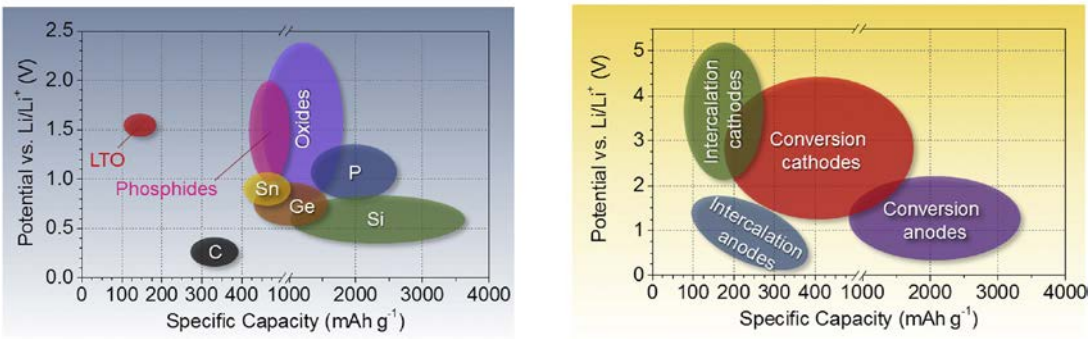

Figure 1-6. Approximate range of average discharge potentials and specific capacity of some of the most common conversion type anodes (experimental), and an overview of the average discharge potentials and specific capacities for all types of electrodes. [18]

1.3 Silicon as an anode material

As mentioned above, Si is one of the most promising candidates for next-generation anode materials due to the low reduction potential, high capacity, and earth-abundant, if volumetric deformation can be controlled. The strategies for better cycle retention of Si electrode have been developed including downsizing in dimension[46], formation of composite[47], doping and functionality[48], morphology control[49-51], and coating method[36].

First, nanostructured-Si shows the different electrochemical behavior with bulky Si[46]. Li ions cannot be diffused into core-level of bulk-Si, remaining the crystalline Si core after enough lithiation due to the low Li^+ diffusivity and electric conductivity. For the deep lithiation up to inner Si, the material size should be in nano-scale. Moreover, it is effectively worked on the stress relaxation. The crack is formed and easily propagated in bulk-Si, while Si nanoparticle (SiNP) shows no fracture on surface due to the higher surface energy which can endure the hoop stress induced lithiation on Si surface[46]. Its threshold particle size, which is unbreakable during lithiation, is under 150 nm. However, it is not a perfect solution with respect to capacity decay.

Si-composite is a popular approach to overcome Si drawbacks. There are two objectives related to kinetic and mechanical support. If Si-composite materials consist of Si and conductive material, conductive material can provide faster kinetics than Si and act as a mechanical buffer, preventing the Si fracture from a volume expansion[47]. The representative examples are graphene-encapsulated Si and graphite blending[52].

It is well known technology that the electric conductivity can be enhanced in doped Si. Its method was applied in synthetic process for anode material. Metallurgic Si consists of Si-Si single covalent bonding, while doped Si exists as the electron-rich or hole-rich state, a lower band-gap, enabling high electric conductivity. Based on enhanced conductivity, the energy barrier of surface lithiation decreased in P-doped Si[48].

The morphology control is another important keyword for the nanostructuring Si[53]. Through this method, Si can be designed for high performance active material. It is commonly classified into four categories: 0 dimensional (0D), 1D, 2D, and 3D Si[54,55]. 0D Si means SiNP mentioned above, and has inevitably a low tap density that is an important point to evaluate the electrochemical results[46]. 1D Si (Si nanowire, SiNW) introduced by Yi Cui shows the high capacity retention due to its structural feature facilitated the internal stress, while it had several limitations for mass production due to the high cost synthetic process and small batch[49]. The electrochemical performance of 2D Si is highly dependent on the thickness of sheet. For example, thin 2D Si has higher surface area-to-volume ratio, resulting in a serious side-reaction and a low

initial coulombic efficiency (ICE), while thick 2D Si has the similar properties with 0D or bulky Si[50]. Since 2D Si is also synthesized through the CVD, the cost problem is inevitable. Finally, 3D Si means the 3D network Si frame such as porous Si. 3D Si has superior cycle retention property owing to numerous pores that act as the void space to alleviate the internal stress and thin Si frame that provides the short Li^+ diffusion path for fast kinetics[51]. However, there is a trade-off between the ICE and cycle retention.

Surface modification method is widely used as coating on Si. It is well known that the thick SEI layer is formed on Si surface after the cycle due to the chemical instability. The thick SEI layer retards the Li^+ solvation, acting as a kind of resistance. To provide the stability to electrolyte and electric conductivity, carbon coating method on Si surface is used in general. Apart from carbon, ceramic and metallic compound is applied for the support from the stress relaxation such as Al_2O_3, Ti_xSi_y, Metal (Cu, Ni, Fe, Ag)[56-61]. The conductive polymer coating, such as polypyrrole and polyaniline, can be included[61, 62].

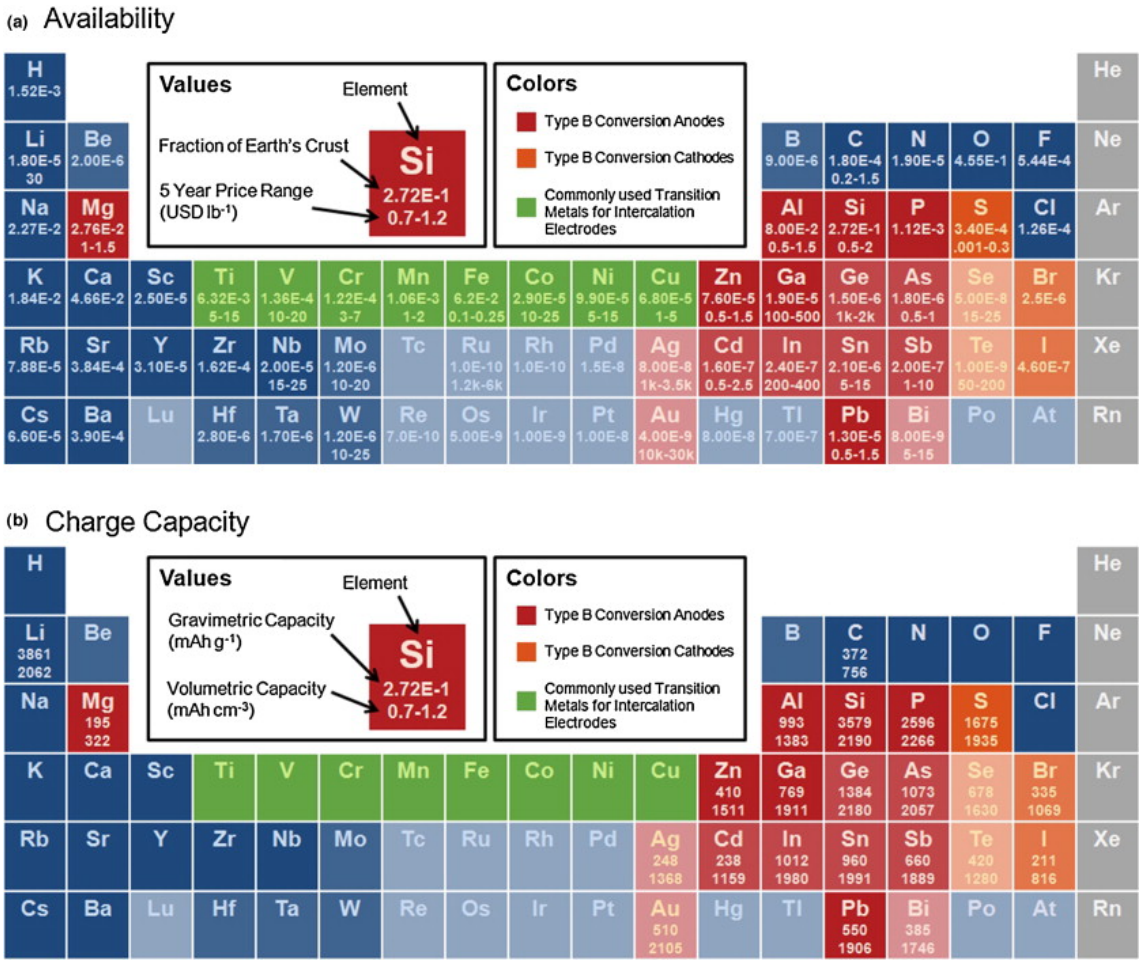

Figure 1-7. (a) Availability and (b) capacities of elements that may host Li as electrodes.[18]

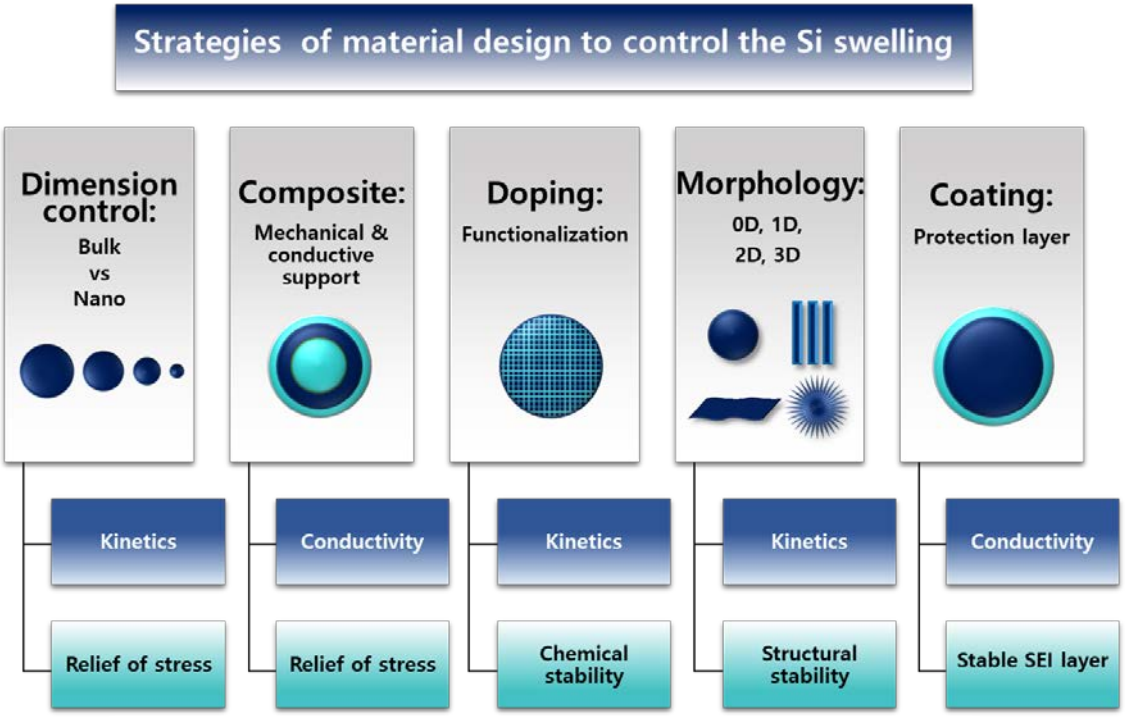

Figure 1-8. The schematic diagram of the strategies in Si material design for the high electrochemical performance.

1.4 Reference

1. Luo, X.; Wang, J. H.; Dooner, M.; Clarke, J., Overview of current development in electrical energy storage technologies and the application potential in power system operation. *Appl Energ* **2015,** *137*, 511-536.
2. Key World Energy Statistics, International Energy Agency (IEA): Paris, France. **2013**.
3. Renewables 2013: Glabal status report, REN21. **2013**.
4. Shafiee, S.; Topal, E., When will fossil fuel reserves be diminished? *Energ Policy* **2009,** *37* (1), 181-189.
5. Sabihuddin, S.; Kiprakis, A. E.; Mueller, M., A Numerical and Graphical Review of Energy Storage Technologies. *Energies* **2015,** *8* (1), 172-216.
6. Kumar, A.; Shukla, S. K., A Review on Thermal Energy Storage Unit for Solar Thermal Power Plant Application. *Energy Procedia* **2015,** *74*, 462-469.
7. Sharma, A.; Tyagi, V. V.; Chen, C. R.; Buddhi, D., Review on thermal energy storage with phase change materials and applications. *Renewable and Sustainable Energy Reviews* **2009,** *13* (2), 318-345.
8. Farid, M. M.; Khudhair, A. M.; Razack, S. A. K.; Al-Hallaj, S., A review on phase change energy storage: materials and applications. *Energy Conversion and Management* **2004,** *45* (9-10), 1597-1615.
9. J.-M. Tarascon, M. A., Issues and challenges facing rechargeable lithium batteries. *Nature* **2001,** *414*, 8.
10. Bradwell, D. J., Liquid Metal Batteries: Ambipolar Electrolysis and Alkaline Earth Electroalloying Cells, Massachusetts Institute of Technology (MIT): Cambridge, MA, USA. **2011**.
11. Cheng, X.; Shi, Z.; Glass, N.; Zhang, L.; Zhang, J.; Song, D.; Liu, Z.-S.; Wang, H.; Shen, J., A review of PEM hydrogen fuel cell contamination: Impacts, mechanisms, and mitigation. *Journal of Power Sources* **2007,** *165* (2), 739-756.
12. Christian Blanc, A. R., Understanding the Vanadium Redox Flow Batteries. In Paths to Sustainable Energy; InTech: Glasgow, UK. **2010**.
13. Bueno, C.; Carta, J. A., Wind powered pumped hydro storage systems, a means of increasing the penetration of renewable energy in the Canary Islands. *Renew Sust Energ Rev* **2006,** *10* (4), 312-340.
14. Bolund, B.; Bernhoff, H.; Leijon, M., Flywheel energy and power storage systems. *Renewable and Sustainable Energy Reviews* **2007,** *11* (2), 235-258.

15. Deane, J. P.; Gallachoir, B. P. O.; McKeogh, E. J., Techno-economic review of existing and new pumped hydro energy storage plant. *Renew Sust Energ Rev* **2010,** *14* (4), 1293-1302.
16. D. Sutanto, K. W. E. C., Superconducting Magnetic Energy Storage Systems for Power System Applications. *IEEE Trans. Appl. Supercond.* **2009,** *20*, 377-380.
17. Sharma, P.; Bhatti, T. S., A review on electrochemical double-layer capacitors. *Energy Conversion and Management* **2010,** *51* (12), 2901-2912.
18. Nitta, N.; Wu, F. X.; Lee, J. T.; Yushin, G., Li-ion battery materials: present and future. *Mater Today* **2015,** *18* (5), 252-264.
19. Xu, J.; Thomas, H. R.; Francis, R. W.; Lum, K. R.; Wang, J.; Liang, B., A review of processes and technologies for the recycling of lithium-ion secondary batteries. *Journal of Power Sources* **2008,** *177* (2), 512-527.
20. Sasaki, T.; Ukyo, Y.; Novak, P., Memory effect in a lithium-ion battery. *Nature materials* **2013,** *12* (6), 569-75.
21. Antolini, E., LiCoO2: formation, structure, lithium and oxygen nonstoichiometry, electrochemical behaviour and transport properties. *Solid State Ionics* **2004,** *170* (3-4), 159-171.
22. Junji Akimoto, Y. G., and Yoshinao Oosawa, Synthesis and Structure Refinement of LiCoO2 Single Crystals. *JOURNAL OF SOLID STATE CHEMISTRY* **1998**, 298—302.
23. Tarascon, M. A. a. J.-M., Building better batteries. *Nature* **2008,** *451*, 652-657.
24. A. MANTHIRAM , J. B. G., LITHIUM INSERTION INTO Fe2(S0& FRAMEWORKS. *Journal of Power Sources* **1989,** *26*, 403-408.
25. Rozier, P.; Tarascon, J. M., Review—Li-Rich Layered Oxide Cathodes for Next-Generation Li-Ion Batteries: Chances and Challenges. *Journal of The Electrochemical Society* **2015,** *162* (14), A2490-A2499.
26. Kim, S.; Cho, W.; Zhang, X.; Oshima, Y.; Choi, J. W., A stable lithium-rich surface structure for lithium-rich layered cathode materials. *Nature communications* **2016,** *7*, 13598.
27. Sun, Y. K.; Chen, Z.; Noh, H. J.; Lee, D. J.; Jung, H. G.; Ren, Y.; Wang, S.; Yoon, C. S.; Myung, S. T.; Amine, K., Nanostructured high-energy cathode materials for advanced lithium batteries. *Nature materials* **2012,** *11* (11), 942-7.
28. Li, H.; Zhou, H., Enhancing the performances of Li-ion batteries by carbon-coating: present and future. *Chemical communications* **2012,** *48* (9), 1201-17.
29. C. Menachem, Y. W., J. Flowers, E. Peled, S.G. Greenbaum, Characterization of lithiated natural graphite before and after mild oxidation. *Journal of Power Sources* **1998,** *76*, 180–185.
30. Xiang, H. F.; Chen, C. H.; Zhang, J.; Amine, K., Temperature effect on the graphite

exfoliation in propylene carbonate based electrolytes. *Journal of Power Sources* **2010,** *195* (2), 604-609.

31. P. Yu, J. A. R., R. E. White, B. N. Popov, Ni-Composite Microencapsulated Graphite as the Negative Electrode in Lithium-Ion Batteries. *Journal of The Electrochemical Society* **2000,** *147* (6), 2081-2085.
32. Xu, K., Nonaqueous liquid electrolytes for Li-based rechargeable batteries. *Chemical Review* **2004,** *104*, 4303-4417.
33. Hu, J.; Li, H.; Huang, X., Electrochemical behavior and microstructure variation of hard carbon nano-spherules as anode material for Li-ion batteries. *Solid State Ionics* **2007,** *178* (3-4), 265-271.
34. YINGHU LIU, J. S. X., TAO ZHENG, J. R. DAHN, MECHANISM OF LITHIUM INSERTION IN HARD CARBONS PREPARED BY PYROLYSIS OF EPOXY RESINS. *Carbon* **1996,** *34* (2), 193-200.
35. Kitta, M.; Akita, T.; Tanaka, S.; Kohyama, M., Two-phase separation in a lithiated spinel Li4Ti5O12 crystal as confirmed by electron energy-loss spectroscopy. *Journal of Power Sources* **2014,** *257*, 120-125.
36. Lee, J.-I.; Ko, Y.; Shin, M.; Song, H.-K.; Choi, N.-S.; Kim, M. G.; Park, S., High-performance silicon-based multicomponent battery anodes produced via synergistic coupling of multifunctional coating layers. *Energy Environ. Sci.* **2015,** *8* (7), 2075-2084.
37. McDowell, M. T.; Lee, S. W.; Nix, W. D.; Cui, Y., 25th anniversary article: Understanding the lithiation of silicon and other alloying anodes for lithium-ion batteries. *Advanced materials* **2013,** *25* (36), 4966-85.
38. Nitta, N.; Yushin, G., High-Capacity Anode Materials for Lithium-Ion Batteries: Choice of Elements and Structures for Active Particles. *Particle & Particle Systems Characterization* **2014,** *31* (3), 317-336.
39. Wang, X.; Tang, D. M.; Li, H.; Yi, W.; Zhai, T.; Bando, Y.; Golberg, D., Revealing the conversion mechanism of CuO nanowires during lithiation-delithiation by in situ transmission electron microscopy. *Chemical communications* **2012,** *48* (40), 4812-4.
40. Zhong, K.; Zhang, B.; Luo, S.; Wen, W.; Li, H.; Huang, X.; Chen, L., Investigation on porous MnO microsphere anode for lithium ion batteries. *Journal of Power Sources* **2011,** *196* (16), 6802-6808.
41. Qingmei Su, D. X., Jun Zhang, Gaohui Du, Bingshe Xu, In Situ Transmission Electron Microscopy Observation of the Conversion Mechanism of Fe2O3/Graphene Anode during Lithiation-Delithiation Processes. *ACS nano* **2013,** *7* (10), 9115–9121.
42. G.X. Wang, Y. C., K. Kontantinov, Matthew Lindsay, H.K. Liu, S.X. Dou, Investigation of

cobalt oxides as anode materials for Li-ion batteries. *Journal of Power Sources* **2002,** *109*, 142-147.

43. Ian A. Courtney, J. R. D., Electrochemical and In Situ X-Ray Diffraction Studies of the Reaction of Uthium with Tin Oxide Composites. *Journal of Electrochemical Society* **1997,** *144* (6), 2045-2052.
44. Zhang, L. Q.; Liu, X. H.; Perng, Y. C.; Cho, J.; Chang, J. P.; Mao, S. X.; Ye, Z. Z.; Huang, J. Y., Direct observation of Sn crystal growth during the lithiation and delithiation processes of SnO(2) nanowires. *Micron* **2012,** *43* (11), 1127-33.
45. Martin Winter, J. O. B., Electrochemical lithiation of tin and tin-based intermetallics and composites. *Electrochemica Acta* **1999,** *45*, 31-50.
46. Xiao Hua Liu, L. Z., Shan Huang, Scott X. Mao, Ting Zhu, Jian Yu Huang, Size-Dependent Fracture of Silicon Nanoparticles During Lithiation. *ACS nano* **2012,** *6* (2), 1522–1531.
47. Magasinski, A.; Dixon, P.; Hertzberg, B.; Kvit, A.; Ayala, J.; Yushin, G., High-performance lithium-ion anodes using a hierarchical bottom-up approach. *Nature materials* **2010,** *9* (4), 353-8.
48. Peng, B.; Cheng, F.; Tao, Z.; Chen, J., Lithium transport at silicon thin film: barrier for high-rate capability anode. *The Journal of chemical physics* **2010,** *133* (3), 034701.
49. Chan, C. K.; Peng, H.; Liu, G.; McIlwrath, K.; Zhang, X. F.; Huggins, R. A.; Cui, Y., High-performance lithium battery anodes using silicon nanowires. *Nature nanotechnology* **2008,** *3* (1), 31-5.
50. Ryu, J.; Hong, D.; Choi, S.; Park, S., Synthesis of Ultrathin Si Nanosheets from Natural Clays for Lithium-Ion Battery Anodes. *ACS nano* **2016,** *10* (2), 2843-51.
51. Kim, H.; Han, B.; Choo, J.; Cho, J., Three-dimensional porous silicon particles for use in high-performance lithium secondary batteries. *Angewandte Chemie* **2008,** *47* (52), 10151-4.
52. Minseong Ko, S. C., Sookyung Jeong, Pilgun Oh, Jaephil Cho, Elastic a-Silicon Nanoparticle Backboned Graphene Hybrid as a Self-Compacting Anode for High-Rate Lithium Ion Batteries. *ACS nano* **2014,** *8* (8), 8591–8599.
53. ANTONINO SALVATORE ARICÒ, P. B., BRUNO SCROSATI, JEAN-MARIE TARASCON, WALTER VAN SCHALKWIJK, Nanostructured materials for advanced energy conversion and storage devices. *Nature materials* **2005,** *5*, 12.
54. Szczech, J. R.; Jin, S., Nanostructured silicon for high capacity lithium battery anodes. *Energy Environ. Sci.* **2011,** *4* (1), 56-72.
55. Ryu, J.; Hong, D.; Lee, H.-W.; Park, S., Practical considerations of Si-based anodes for lithium-ion battery applications. *Nano Research* **2017**.
56. Hwang, G.; Park, H.; Bok, T.; Choi, S.; Lee, S.; Hwang, I.; Choi, N. S.; Seo, K.; Park, S., A

high-performance nanoporous Si/Al2O3 foam lithium-ion battery anode fabricated by selective chemical etching of the Al-Si alloy and subsequent thermal oxidation. *Chemical communications* **2015,** *51* (21), 4429-32.

57. Park, O.; Lee, J.-I.; Chun, M.-J.; Yeon, J.-T.; Yoo, S.; Choi, S.; Choi, N.-S.; Park, S., High-performance Si anodes with a highly conductive and thermally stable titanium silicide coating layer. *RSC Advances* **2013,** *3* (8), 2538.
58. Choi, S.; Lee, J. C.; Park, O.; Chun, M.-J.; Choi, N.-S.; Park, S., Synthesis of micro-assembled Si/titanium silicide nanotube anodes for high-performance lithium-ion batteries. *Journal of Materials Chemistry A* **2013,** *1* (36), 10617.
59. Park, H.; Lee, S.; Yoo, S.; Shin, M.; Kim, J.; Chun, M.; Choi, N. S.; Park, S., Control of interfacial layers for high-performance porous Si lithium-ion battery anode. *ACS applied materials & interfaces* **2014,** *6* (18), 16360-7.
60. Yoo, S.; Lee, J.-I.; Ko, S.; Park, S., Highly dispersive and electrically conductive silver-coated Si anodes synthesized via a simple chemical reduction process. *Nano Energy* **2013,** *2* (6), 1271-1278.
61. Park, H.; Choi, S.; Lee, S.; Hwang, G.; Choi, N.-S.; Park, S., Novel design of silicon-based lithium-ion battery anode for highly stable cycling at elevated temperature. *J. Mater. Chem. A* **2015,** *3* (3), 1325-1332.
62. Wu, H.; Yu, G.; Pan, L.; Liu, N.; McDowell, M. T.; Bao, Z.; Cui, Y., Stable Li-ion battery anodes by in-situ polymerization of conducting hydrogel to conformally coat silicon nanoparticles. *Nature communications* **2013,** *4*, 1943.
63. Yao, Y.; Liu, N.; McDowell, M. T.; Pasta, M.; Cui, Y., Improving the cycling stability of silicon nanowire anodes with conducting polymer coatings. *Energy & Environmental Science* **2012,** *5* (7), 7927.
64. M. Rosa Palacin, Recent advances in rechargeable battery materials: a chemist's perspective. *Chem. Soc. Rev.* **2009**, 38, 2565-2575.

Chapter II. A siloxane-incorporated copolymer as an *in-situ* cross-linkable binder for high performance silicon anodes in Li-ion batteries

Introduction

2.1 Introduction

Silicon has been intensively studied as a candidate anode material for Li-ion batteries (LIBs) over the last few decades. Such research is driven by the high energy density of silicon, which can surpass that of conventional carbon-based anode materials[1, 2]. However, the silicon anode is limited by critical problems such as large volume expansion (~300%)[3] during the lithiation process and deficient Li-ion diffusivity (1.8×10^{-14} cm^2 s^{-1} at room temperature)[4]. Numerous strategies have been developed to solve these problems, including coating the silicon surface with effective materials (e.g., carbon[5], Ag[6], $Li_4Ti_5O_{12}$[7], Al_2O_3[8, 9], etc.,) and the design of nanostructured silicon[10] (e.g., hollow particles[11], core-shell structures[12], nanowires[13], and porous structures[14]). The electrochemical performance of the silicon anode is strongly size-dependent in such a way that formation of cracks and fracture is almost negligible when the particle size of silicon is below 150 nm[10]. However, the nanostructured materials generally have a low tap density and high specific surface area, resulting in low energy density and a large irreversible capacity loss. This is linked to the emergence of active/inactive composites having a higher tap density and lower specific surface area than the nanomaterials [15]. Therefore, silicon anodes with effective coating layers have attracted significant attention for use in LIBs. Although the aforementioned silicon anodes have shown promising electrochemical performance, further development of silicon must be achieved for practical implementation. Control of the polymeric binder is one prospective avenue to resolve this problem.

In inceptive studies, poly(vinylidene fluoride) (PVdF), which is a thermoplastic material with poor elastomeric properties, was used as a conventional binder for carbonaceous materials and alloy anodes. The poor efficiency of the PVdF binder in alloy anodes has led to the introduction of several alternative binders such as poly(vinylidene fluoride-tetrafluoroethylene-propylene) (PVdF-TFE-P), styrene-butadiene rubber (SBR), and crosslinked poly(acrylic acid)/sodium carboxymethyl cellulose (PAA/CMC)[16] to accommodate the large volume change of alloying materials to achieve better cycle retention[15]. Stiff and brittle polymer binders such as PAA and CMC are more effective than PVdF or SBR for enhancing the capacity retention of LIBs[17, 18]. CMC can form strong connections with carbon black, the active materials, and the current

collector to form a network with each other[19]. Dahn et al. asserted that the lithium polyacrylate (Li-PAA) binder gave rise to much better capacity retention than the CMC binder[20]. Furthermore, Kovalenko et al. reported that an alginate binder from natural resources gave rise to better initial columbic efficiency (ICE), and cycle stability and was a less expensive and more environmentally friendly binder[21]. Accordingly, these reports indicated that the cycle performance was strongly influenced by the selection of the binder. Further investigations are therefore needed to optimize the effects of various binder systems. Recent studies have explored several approaches for modification of binders to improve the electrochemical properties of the silicon anode, including introduction of conducting functional groups in the polymer backbone to achieve a conducting binder[22-24], modification of conventional CMC[25], PAA[26], and alginate[27] binders, as well as binder design based on an interconnected three-dimensional (3D) network[16, 28-29]. All of these approaches furnished superior performance in terms of the ICE, cycle retention, and specific capacity, compared to conventional PVdF-based binders. CMC-based binders can be considered as state-of-the-art in this field[16, 22]. The advantages associated with CMC include the natural abundance of cellulose (which is the precursor for CMC), water solubility, and easy disposal after cycling. These properties make CMC useful as a commercial adhesive for the nano-Si/C anode of LIBs with long-term durability[30]. However, the demerits of CMC include the uncontrollable molecular weight, non-tunable mechanical properties, and surface oxidation of the Si[31] anodes. These limitations have led to the introduction of another polymeric binder, poly(acrylic acid) (PAA). The major advantage and selling point of PAA is the possibility for enrichment of the carboxylic acid functional groups[31]. However, electrode cracking and consequent pulverization occur after several cycles due to the glassy nature of the electrode in which PAA is used as a binder. An alginate-based binder effectively improved the electrochemical performance of the Si-based anode compared to CMC and PAA[27]. The one-dimensional structure and the secondary interactions of the binder are sensitive to the severe volume expansion of Si. In due course, a 3D network-forming binder was proposed and has been the subject of overwhelming recent interest.

In a dedicated effort to eliminate certain existing demerits associated with available binders, the present study describes the development of an *in situ* cross-linkable, 3D, interconnected, siloxane-containing novel polymeric binder, poly(*tert*-butyl acrylate-*co*-triethoxyvinylsilane). The *tert*-butyl protecting group undergoes decomposition upon thermal treatment and forms a highly interconnected 3D network via the condensation reaction. This process may minimize the electrode disintegration caused by silicon volume expansion.

An additional problem associated with the silicon anode that reduces the battery efficiency is the formation of an unstable solid-electrolyte-interface (SEI) on the silicon surface. In most cases, the SEI layers formed on the silicon surface are unstable and cannot

protect the electrode from undergoing further reaction with the electrolyte. The volume expansion of silicon particles results in the formation of cracks on the SEI layer, leading to continuous consumption of electrolyte. The SEI layers thus became thicker and reduced the battery performance[32]. In order to minimize this problem, we introduced silicon functional groups in the present molecular design. The high affinity between silicon and fluorine is well-established[33]. Thus, it was anticipated that during cycling, once the SEI is formed from a conventional lithium salt such as lithium hexafluorophosphate ($LiPF_6$), it should exist as a stable coating layer over several cycles due to the presence of fluoride ions and protect the electrode from further reaction with the electrolyte.

For practical application, the production cost and synthetic feasibility of the binder also must be considered. The present binder can be synthesized via simple 2,2′-azobis-(isobutyronitrile) (AIBN)-mediated free radical polymerization, which is cost effective and less time consuming. Herein, we synthesize a series of random copolymers consisting of *tert*-butyl acrylate and triethoxyvinylsilane and evaluate the electrochemical behavior of various binders on the Si anode. In-depth investigations show that 21% of TEVS in the random copolymer gives rise to superior performance of the copolymer as a binder for Si anodes in Li-ion batteries.

2.2 Experimental

Materials and Characterizations

tert-Butyl acrylate [stabilized with hydroquinone monomethyl ether (MEHQ), Tokyo Chemical Industries (TCI), Tokyo, Japan] was passed through an alumina column before use to remove inhibitors. Triethoxyvinylsilane was purchased from TCI and was used without further purification. Polyacrylic acid (PAA), Carboxymethylcellulose (CMC), Alginate, Polyvinylidinefluoride (PVdF) was obtained from Sigma Aldrich Korea. Dialysis membranes with molecular weight cut-offs (MWCOs) of 12−14 kDa were obtained from Spectra/Pro. The polymers were characterized using 400 MHz ^{1}H-NMR spectroscopy, FT-IR spectroscopy, and gel permeation chromatography (GPC) [poly(methyl methacrylate) standards in tetrahydrofuran eluent] (Agilent Technologies, Santa Clara, CA). Thermogravimetric analyses were performed with a TGA Q500 V20 analyzer (TG instruments, 159 Lukens Dr., New Castle, DE 19720, United States of America) under nitrogen atmosphere at a heating rate of 10 ^{o}C/min. Top- and cross-sectional images of the silicon anode before and after cycling were acquired by scanning electron microscopy (Various 460, FEI) at 10 kV without any metal coating process. X-ray photon spectroscopy measurement (K-alpha, Thermo Fisher) was used to characterize the SEI layer formation on the silicon surface.

Synthesis of poly(*tert*-butyl acrylate-*co*-triethoxyvinylsilane)

A series of random copolymers was synthesized by AIBN-mediated free radical polymerization. Similar procedures were used to synthesize the random copolymers. For batch TBA-TEVS-21 (where the number at the end indicates the amount of TEVS), AIBN (4.2 mg, 0.026 mmol), *tert*-butyl acrylate (3.3 g, 25.75 mmol), and triethoxyvinylsilane (2.95 g, 15.45 mmol) were purged with nitrogen for 15 min in an oven-dried round-bottom flask. The mixture was stirred at 100 °C for 24 h in an oil bath. The resulting reaction mixture was dissolved in methanol (MeOH) and dialyzed against MeOH using a dialysis membrane with a molecular weight cut-off of 12−14 kDa. After dialysis, methanol was evaporated to yield the pure product as a white solid (yield = ~ 90 %). GPC (M_n = 15 kDa). To synthesize polymers with varying molar ratios, the amount of AIBN and *tert*-butyl acrylate was maintained constant, and the amount of triethoxyvinylsilane was varied using the same synthetic procedure as described above (the samples are hereafter represented as TBA-TEVS-n, where ‘n’ indicates the mol-percentage of the triethoxyvinylsilane functional group). For synthesizing polymers with varying molar composition, amount of

triethoxyvinylsilane were varied using the similar synthetic procedure as described for TBA-TEVS-21. TBA-TEVS-9, TBA-TEVS-26, TBA-TEVS-34, TBA-TEVS-50, and TEVS, were synthesized with similar method by varying the amount of triethoxyvinylsilane from 0.95 g (5.15 mmol), 4.9 g (25.75 mmol), 9.8 g (51.5 mmol), to 39.2 g (103 mmol) respectively. Complete syntheses of the polymer batches were confirmed by FT-IR and ^{1}H-NMR spectroscopy.

Experiment to Confirm the cross linking.

The cross linking of TBA-TEVS-n was confirmed by FT-IR spectroscopy. The polymer film was made on the silicon wafer surface from 15 wt.% polymer solutions in N-methyl Pyrrolidine (NMP). The film kept initially kept under vacuum at room temperature in order to evaporate the solvent for 24hr, and then allowed to undergo cross linking at high temperature vacuum oven at 250 ^{0}C for 2 hr. The films were then used to measure the FT-IR spectra.

Nanoindentation Measurement

Nanoindentations were carried out at room temperature using XP module of Nanoindenter G200 instrument (Agilent Technologies, Santa Clara, CA) with a three-sided pyramidal Berkovich indenter. Twenty nanoindentations were made for each sample to obtain reproducible data. Maximum indentation depth was 1000 nm, which was shallower than 1/10 of the sample thickness. Although hardness and elastic modulus as a function of indentation depth measured by continuous stiffness measurement (CSM) do not show stable trend at very shallow indentation depths, primarily because of intrinsic issues at very early stage of contact in nanoindentation, data collected at indentation depths greater than 100 nm show stable trends that are nearly constant for both the hardness and elastic modulus.

Electrochemical Measurement

The electrochemical properties of a silicon anode employing the polymeric binder were tested using a 2016 R-type coin cell. Lithium metal was used as counter electrode in the half-cell. The working electrode consisted of 10 wt.% carbon-coated silicon nanoparticles (70%, Alfa Aesar), synthesized binder (15%), and super-P (15%). The mixed slurry was spread on a Cu current collector and dried at 250 ^{o}C for 2 hr. under vacuum. $LiPF_6$ (1.3 M) in ethylene carbonate and diethyl carbonate (Panaxetec, EC/DEC, 3:7 volume ratio) with 10 wt.% fluoroethylene carbonate (FEC) was used as the electrolyte. The loading mass of active material was about ~1.0 mg cm^{-2}, except for that used for the high mass loading test (1.6 mg cm^{-2}). The half-cells were tested in the voltage range of 0.00

5 V to 1.5 V at a rate of 0.05–0.2 C. All the cells were electrochemically tested with a WBCS-3000 battery cycler (Wonatech Co.) at ambient temperature.

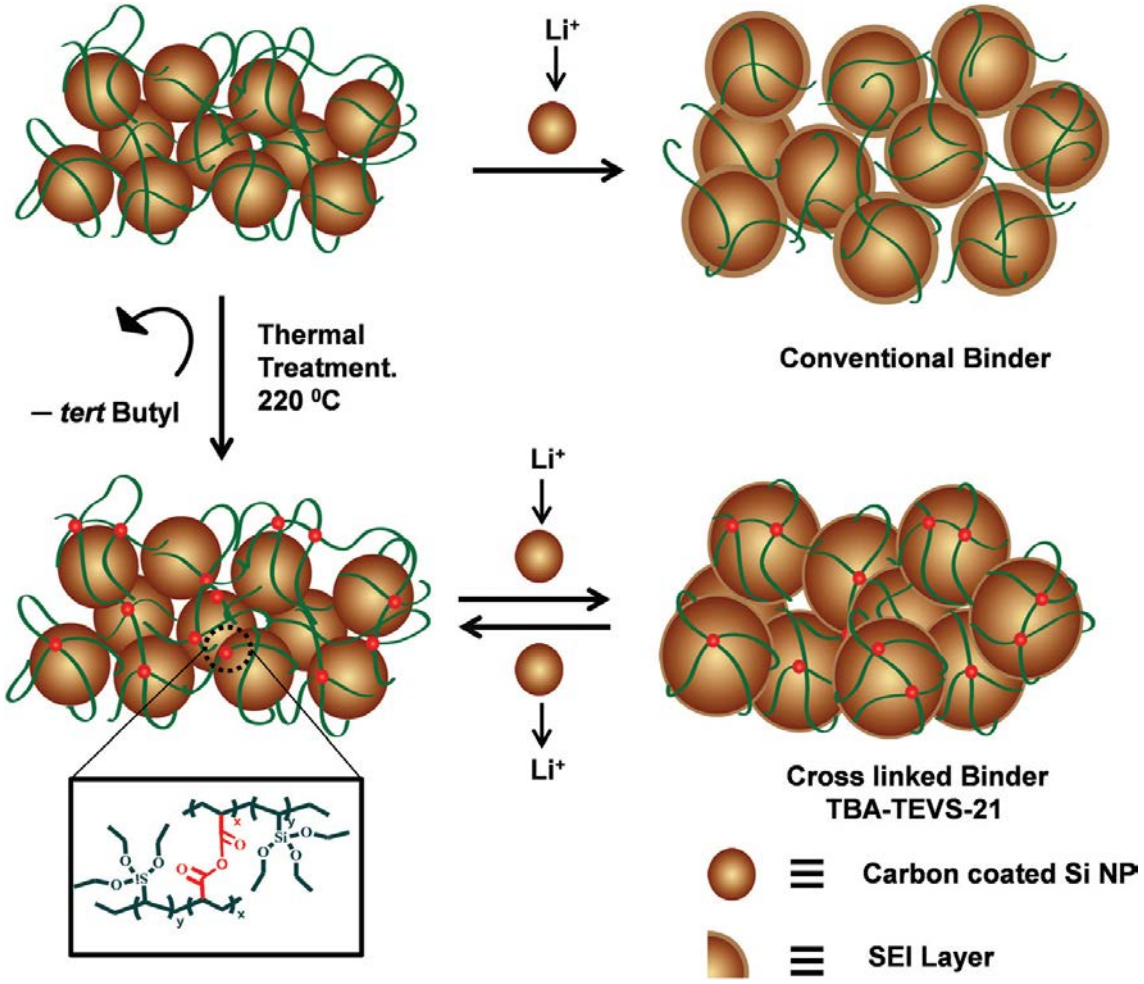

Figure 2-1. Schematic representation of a superior polymeric binder, TBA-TEVS-21, which is incorporated with siloxane and in situ cross-linkable functional moieties.

2.3 Results and discussion

We successfully synthesized and characterized a series of random copolymers, poly(*tert*-butyl acrylate─*co*─triethoxy-vinylsilane), by free radical polymerization (Figure 2-2a). The polymers were prepared with different molar ratios of the constitutive monomers (Table S1), TBA-TEVS-n, where 'n' was varied as 9, 21, 26, 34, 50, and 100 mol.% in order to find the optimum composition of the random copolymer for maximizing the efficiency as a binder for the silicon anode. The percentage composition of each monomer in the polymer was determined from ^{1}H-NMR analysis by comparing the integrals of the peaks of hydrogen attached to the tertiary carbon of the *tert*-butyl group, which appeared at 2.23 ppm ($CDCl_3$), with that of the secondary hydrogen close to the oxygen in the siloxane group, which appeared at 3.79 ppm ($CDCl_3$) (Figure 2-2b). As the amount of TEVS was increased, the intensity of the peak at 3.79 ppm also increased, whereas the intensity of the peak at 2.23 ppm decreased along with a change in the integral value, which confirmed successful synthesis of polymers with different compositions.

We conducted a series of galvanostatic measurements to investigate the effect of varying the TEVS content in the binder on the electrochemical performance of the assembly by fabricating a coin type half-cell with lithium metal as the counter electrodes. Fig. 2-3a shows the first cycles in the galvanostatic discharge and charge curves for the carbon-coated silicon nanoparticles (10%) with various polymeric binders, acquired in the range of 0.01–1.5 V. The TBA-TEVS-n polymeric binder gave rise to significantly enhanced cycle retention and better columbic efficiency than the conventional PVdF binder. However, slight variation of the TEVS content in the new polymeric binder resulted in a considerable change in the specific capacity as shown in Fig. 2-3b. TBA-TEVS-9 (with the lowest TEVS content) gave rise to a specific capacity of 3090 mAh g^{-1} and an ICE of 80.8%. In this case, even though the specific charge capacity was retained up to 50 cycles, a continuous decay was observed after 70 cycles. It can be assumed that extensive pulverization and the lack of a stable SEI contribute to this observed decay. With a further increment of the TEVS content up to 21%, TBA-TEVS-21 exhibited a high charge capacity of 3100 mAh g^{-1} and ICE of 81.8%.

TBA-TEVS-21 gave rise to surprisingly stable cycle retention up to 100 cycles compared to the other samples. Further increasing the TEVS content anomalously reduced the specific charge capacity and cycle retention. The TEVS homopolymer gave rise to dramatically poor performance with almost zero specific capacity after 50 cycles. This

result indicates that the TEVS polymer by itself is ineffective as an anode binder since it cannot withstand significant internal stress during cycling. TBA-TEVS-50 gave rise to moderate performance with an initial specific capacity of 2551 mAh g^{-1} and a retained capacity of about 1500 mAh g^{-1} after 100 cycles. This decrease in the capacity may be attributed to decreased cross-linking density. The respective specific capacities achieved with the binders having various TEVS contents were 2991.9, 2598.7, 2551, and 2362 mAh g^{-1} for 26%, 34 %, 50 %, and 100% TEVS. Twenty-one percent of TEVS with TBA was optimal for producing an efficient binder for the silicon anode in the lithium ion battery.

Peaks corresponding to only silicon were observed in the cyclic voltammogram of TBA-TEVS-21, and no peaks corresponding to any side reactions of the binder with lithium metal or the electrolyte were apparent (ESI, Fig. S1). The minimized side reaction of TBA-TEVS-21 due to the presence of siloxane building block combined with its high columbic efficiency demonstrates that stable SEI layers were formed on the electrode surface, and electrolyte decomposition on the electrode surface became slower over hundreds of cycles. The high sustainability of TBA-TEVS-21 indicates that it can maintain electronic and ionic transport pathways at the silicon-silicon interface without serious side reactions. To further confirm the good cycle retention, electrochemical impedance spectroscopy (Figure 2-4) analysis was carried out at both the initial and 100^{th} cycle The Nyquist plot in the range of 100 kHz to 0.1 Hz with an amplitude of 10 mV shows a semicircle related to the SEI layer resistance. In the case of TBA-TEVS-21, the SEI layer-related resistance was maintained from the first to 100^{th} cycle at about 40 Ω, while the resistances of TBA-TEVS-50 and TBA-TEVS-100 were about 180 Ω and over 3500 Ω, respectively. A larger semicircle represents higher resistance of the SEI layer, which is attributed to loss of the electric transfer pathway owing to severe volume expansion, resulting in decay of the charge capacity. In order to confirm the good mechanical binding energy and electronic contact of TBA-TEVS-21, a rate capability test was performed up to 10 C rate. Even at current rate of 10 C rate, a specific capacity of over 1750 mAh g^{-1} was retained with TBA-TEVS-21 after several cycles (Figure 2-3c). The high specific capacity achieved with the binder during such fast charging and discharging indicates that the binder based on TEVS provides a sufficiently stable SEI layer to prevent side reactions of the silicon particle with other components. The binder gave rise to an excellent specific capacity of 2000 and 2250 mAh g^{-1} at 8 C and 3 C rate, respectively, which confirmed the superiority of TBA-TEVS-21 as an effective binder for the silicon anode in LIBs. In addition, high-mass loading of active materials plays a key role in enhancing energy density of LIB anodes. Figure 2-2d shows cycle retention of silicon anode with a high areal capacity of 2.02 mAh cm^{-2}, which

resulted in exceptional cycling stability. We have then compared the electro chemical performance of TBA-TEVS-21 with the most commonly used as called conventional binders, such as PAA, CMC, Alginate, PAA-CMC mixture and PVdF. The PVdF is a poor binder for the Si anode because of the very weak interactions between binder and Si nanoparticles, leading to the desquamation of active materials from the current collector during cycling. Even though all other binders that we have choose as a control are known as the best polymers for Si anodes, the TBA-TEVS-21 exhibited high cycle retention with much higher specific capacity. (Figure 2-3e, d)

To confirm the fact that, TBA-TEVS-21 could provide a stable SEI to the electrode throughout the cycling, we have evaluated the SEI layer composition on the silicon nanoparticle surface after first and twenty cycles using X-ray photon spectroscopy (XPS). The comparison of C 1s spectra of TBA-TEVS-21 with C 1s spectra of PAA-CMC showed that the intensity of the peak corresponding to Li_2CO_3, which is a result of electrolyte (EC) decomposition, is significantly reduced in TBA-TEVS-21 compared to PAA-CMC. This observation directly indicates that the TBA-TEVS-21 binder is well coated to the Si nano particle surface which prevents the further decomposition of electrolyte and thereby prevents the breaking. Similarly, the 1s F spectra indicated that the peak intensity corresponding to LiF is lower for TBA-TEVS-21 after cycling where as it is observed with high intensity in the case of PAA-CMC binder. The LiF is major composition of SEI layer, which come from fluoroethylene carbonate (FEC). A higher intensity of this peak represents higher salt decomposition from the electrolyte, similarly lower intensity of this peak in TBA-TVES-21 binder directly supports our hypothesis that the binder provides a stable and thin coating, so that the further decomposition is significantly reduced in the case of TBA-TEVS-21 that in turn refers stable SEI.

We have thus far presented a series of analyses and instrumental techniques to investigate the remarkably superior performance of the as-synthesized novel polymeric TBA-TEVS binders. Multiple synergistic effects are required in order to explain the stable performance of the silicon-incorporated polymeric binder with the optimum percentage of TEVS, herein TBA-TEVS-21, rather than a single factor. The foremost reason for this stable performance is expected to arise from the highly stable, robust, and interconnected 3D polymer network that forms upon thermal treatment of the electrode containing the binder. TGA analysis of TBA showed that the *tert*-butyl group in the polymer decomposes around 250 ^{o}C (Fig. S3); thereafter, it changes to PAA. Aware of this transformation, we subjected the binder to heat treatment under vacuum to achieve de-protection of the *tert*-butyl protecting group and produce the carboxylic acid functionality with simultaneous crosslinking. The temperature for decomposition of the *tert*-butyl protecting group in TBA-TEVS-n was slightly lower than that of pure poly(*tert*-butyl acrylate), and the temperature

decreased in accordance with a decrease in the percentage of the *tert*-butyl group. For TBA-TEVS-21, decomposition of the *tert*-butyl group occurred at 215 ^{o}C (ESI, Fig. S4). Crosslinking resulted in the formation of an anhydride between two adjacent carboxylic acid groups which had undergone the condensation reaction. This leads to the formation of in an *in-situ* cross-linkable binder, which ensures sufficient stability of the 3D crosslinked network to minimize pulverization of the silicon particles. FT-IR spectral analysis of TBA-TEVS-21 after thermal treatment shows the appearance of a new peak around 1800 cm^{-1}, which confirms the formation of an ester bond (Figure 2-5). In order to make sure the peak around 1800 cm^{-1} stands for carbonyl stretching frequency of anhydride, we have conducted the similar cross-linking experiment with PAA. The FT-IR analysis of PAA also showed a distinct peak at 1808 cm^{-1} which confirms the formation of anhydride as a result of condensation reaction of two adjacent carboxylic acid functional groups. (ESI, Fig S5). The broad peak at 3000–3500 cm^{-1} in the FT-IR spectrum implies the presence of non-crosslinked carboxylic acid groups. The free carboxylic acid group further enhances the 3D network by multi-dimensional non-covalent interactions such as inter-intra molecular hydrogen bonding. Moreover, the carboxylic acid group improves the adhesion between the silicon surface and the current collector[28]. Even though the binder exhibited superior performance at a low Si loading with 15 wt.% of TBA-TEVS-21, it is necessary to demonstrate its efficiency with a high silicon mass loading in order to achieve higher energy density. Most of the binders that exhibit excellent performance at low mass loading fail to retain the superior performance during cycling at higher mass loading due to huge volume expansion, collapse of the SEI layer, and consequent loss of electrical contact with the active material. In order to investigate the effect of the TBA-TEVS binder on the electrochemical performance of the silicon anode with higher mass loading, we fabricated a thicker electrode with a loading level of 1.6 mg cm^{-2}. As aforementioned, the bi nder retained a high areal capacity of 2.02 mAh cm^{-2}, which did not fall below 1.7 mA h cm^{-2} over 50 cycles (Figure 2-3d). This observation led us to conclude that the develo ped binder can serve as an efficient candidate for practical anode application for the rea lization of a high energy electrode. For deeper evaluation of the stability of the electrodes, SEM images were acquired after 100 cycles for the electrode with the TBA-TEVS-21 binder. We have confirmed the size distribution of pristine silicon nano particle by TEM before coating with 10% carbon. The TEM analysis showed a particle size distribution of around 150 nm (Fig. 2-5a). The TEM reveals the uniform carbon coating of silicon nano particle without any aggregation (Figure 2-6b). Figure 2-6c shows the SEM images for as-fabricated silicon electrodes in which the binder was neatly stacked on the copper foil with a thickness of 13.3 μm (Figure 2-6c). After 100 cycles, the electrode thickness increased to 25.8 μm (Figure 2-6d). This increment of electrode thickness implies that the silicon electrode took place a little volume expansion of 90%

with a slight agglomeration, in which the silicon particles were still strongly connected to each other (Figure 2-6f).

In order to gain insight into the mechanical behavior of the new binder, nano indentations were conducted. The binders exhibited remarkable enhancement in hardness and elastic modulus after thermal crosslinking. Before crosslinking, the hardness and elastic modulus of TBA-TEVS-21 were respectively quantified as 0.09 (± 0.002) and 2.3 (± 0.02) GPa. The same binder exhibited somewhat enhancement after crosslinking, as indicated by the change in the hardness and modulus to 0.33 (± 0.03) and 8.1 (± 0.5) GPa, respectively. These are even higher than those of conventional PAA binders for which hardness and modulus values of 0.09 (±0.01) and 3.80 (±0.20) GPa have been respectively reported (ESI, Fig. S7). This comparison strongly supports the present proposal that TBA-TEVS-21 can act as a superior performance binder by providing sufficient mechanical support.

We have analysed the impact of mechanical property of the TBA-TEVS-n binder series on the electro chemical behaviour (ESI, Fig. S6). To investigate this, we have conducted the nano-indentation tests for TBA-TEVS-9 and TBA-TEVS-34 and compared it with cross-linked PAA binders. After cross-linking, the TBA-TEVS polymers exhibited a decreasing trend in the hardness as well as modulus value along with the increasing percentage of TEVS content. The TBA-TEVS-9 showed highest value for both hardness and modulus 0.33 (±0.01) and 8.1 (±0.2) GPa respectively after cross linking. As shown in Table 1, it is clear that there should be an optimum hardness and modulus in order for the binder to exhibit the better electro chemical performance. The better electrochemical performance of TBA-TEVS-21 can also be attributed to its high elastic modulus (7.6 (±0.2) GPa) compared with conventional PAA binder (6.5 (±0.2) GPa). However, the TBA-TEVS-34 possesses the lowest value for both hardness and modulus among this series, 0.23 (±0.01) and 6.1 (±0.2) GPa respectively, and it exhibited poor electro chemical performance among the three. The TBA-TEVS-9 showed a stable electro chemical performance until 70 cycles but after that it drastically decreased. This drastic decrease might be associated with high hardness of TBA-TEVS-9.

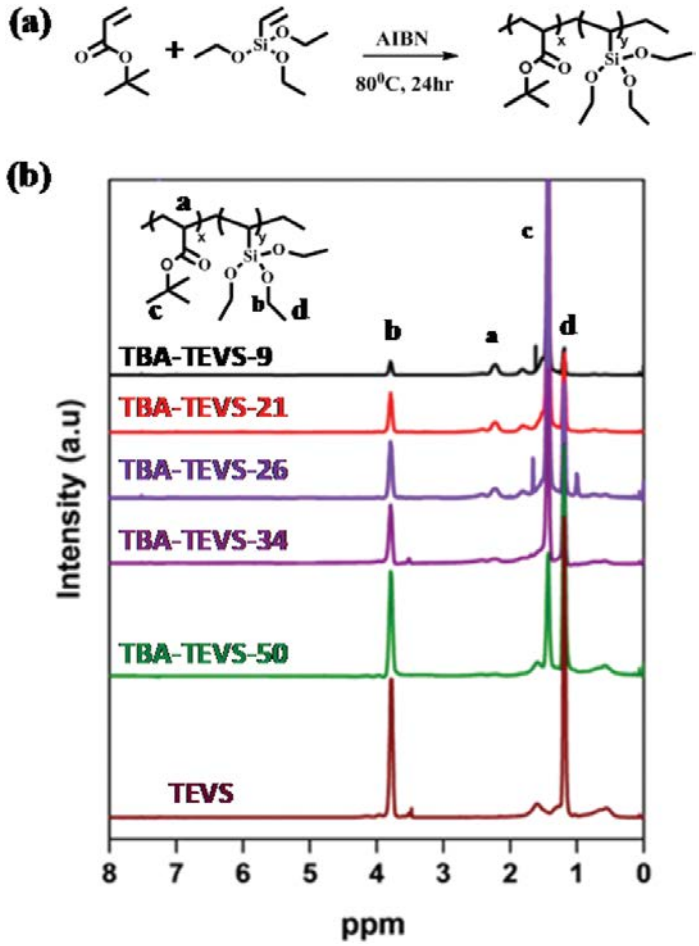

Figure 2-2. (a) Synthetic approach for the preparation of TBA-TEVS-n, (b) characterization of TBA-TEVS-n by 1H-NMR.

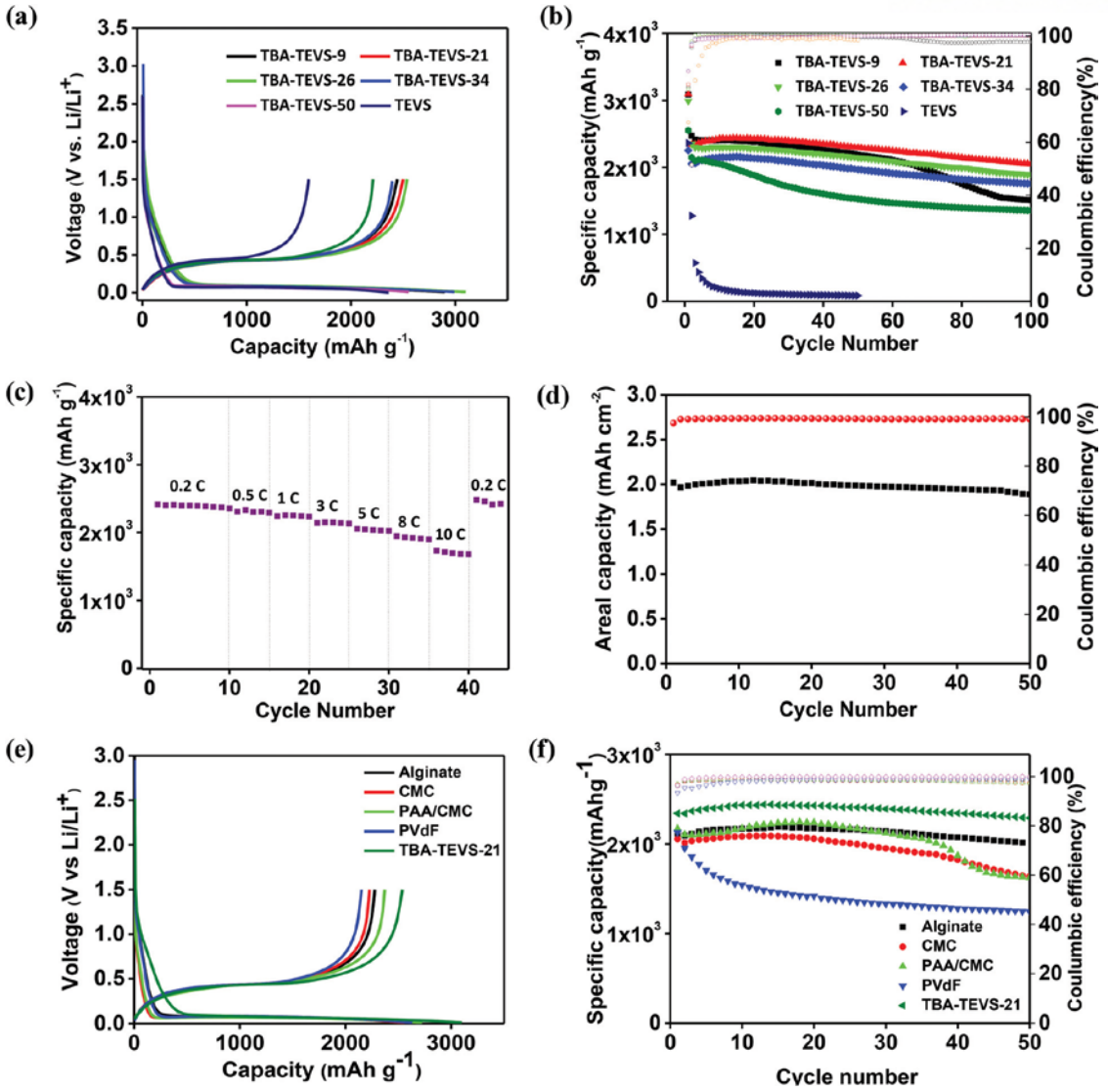

Figure 2-3. (a) Formation voltage profiles and (b) cycle retention tests of the silicon anodes which were made with various amounts of the TBA-TEVS polymeric binder. (c) Rate capability test of silicon anodes with a different current density (1C = 2.5 A g−1) each for 5 cycles at room temperature. (d) High loading level cycle evaluation shows outstanding areal capacity and great retention. (e) Formation voltage profiles and (f) cycle retention tests of the silicon anodes which were made with TBA-TEVS-21 in comparison with PAA, CMC, PAA-CMC and PVdF.

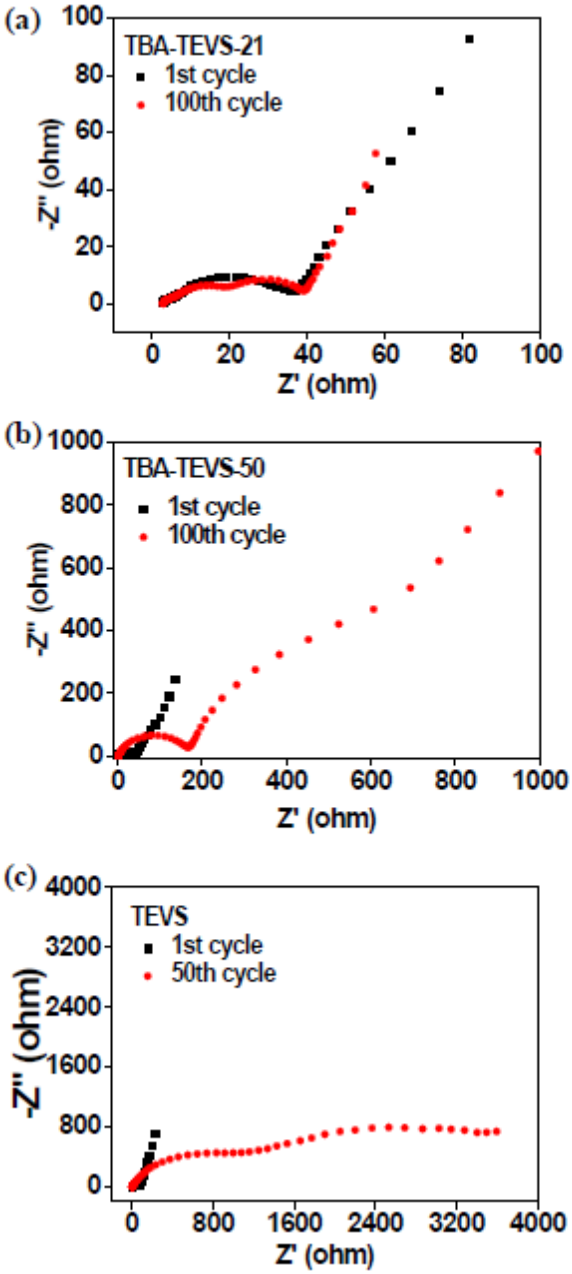

Figure 2-4. Nyquist plots of Si anode prepared with polymeric binders with various TEVS contents. (a) TBA-TEVS-21, (b) TBA-TEVS-50, and (c) TEVS. TBA-TEVS-21 sample showed the lowest SEI resistance and charge transfer resistance values, and also maintained initial resistance after 100 cycles

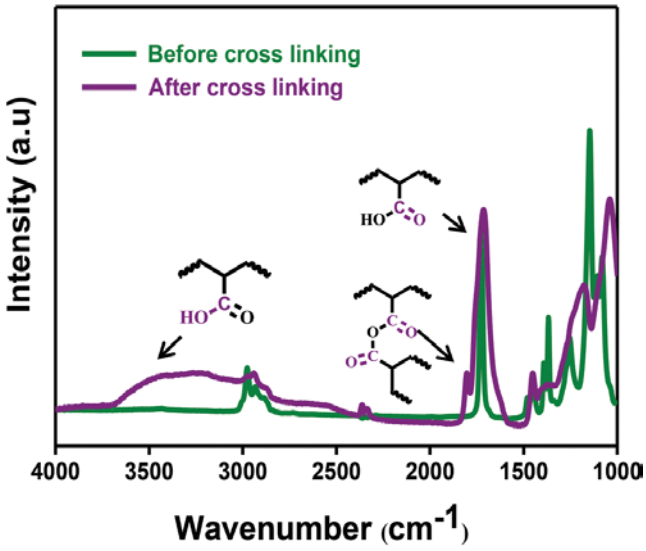

Figure 2-5. FT-IR spectra of TBA-TEVS-21 before and after crosslinking show the formation of an anhydride linkage after thermal treatment at 220 °C.

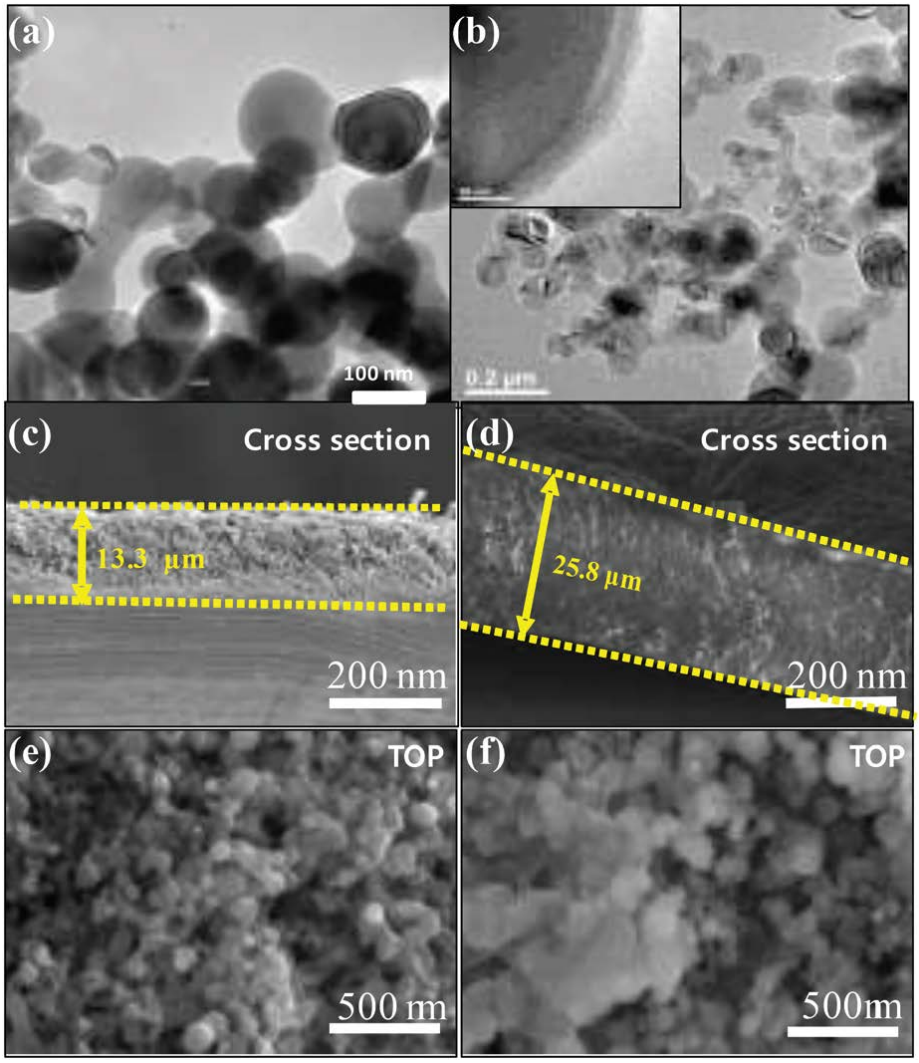

Figure 2-6. (a) TEM image of pristine silicon nanoparticles showing a particle size distribution of around 150 nm. (b) TEM images after 10% carbon coating. SEM images of (c) and (e) the as-prepared silicon electrode using the TBA-TEVS21 binder and (d) and (f) silicon electrode after 100 cycles. Silicon nanoparticles were somewhat aggregated with over 90% volume expansion during 100 cycles, but still maintained the nano-size scale.

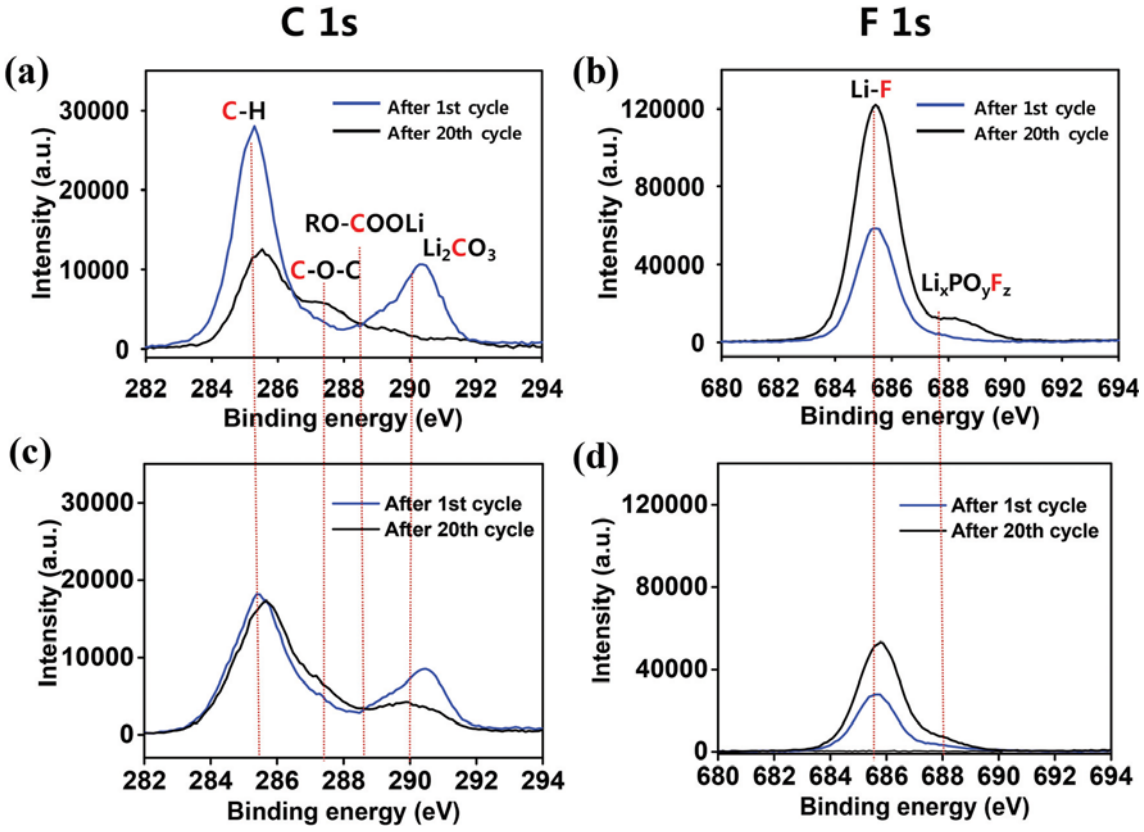

Figure 2-7. XPS spectra on the silicon anode surface with the PAA-CMC binder (a), (b), and TBA-TEVS-21 (c), (d) after the first and twentieth cycles. The C 1s spectra showed a significantly lower intensity for TBA-TEVS-21 indicating the uniform coating of TBA-TEVS-21 on the silicon nanoparticle surface. The significantly lower intensity for the LiF peak implies lower salt decomposition from the electrolyte on the silicon nanoparticle. These observations stand for the formation of a stable and thin layer of SEI for the electrode with the TBA-TEVS-21 binder.

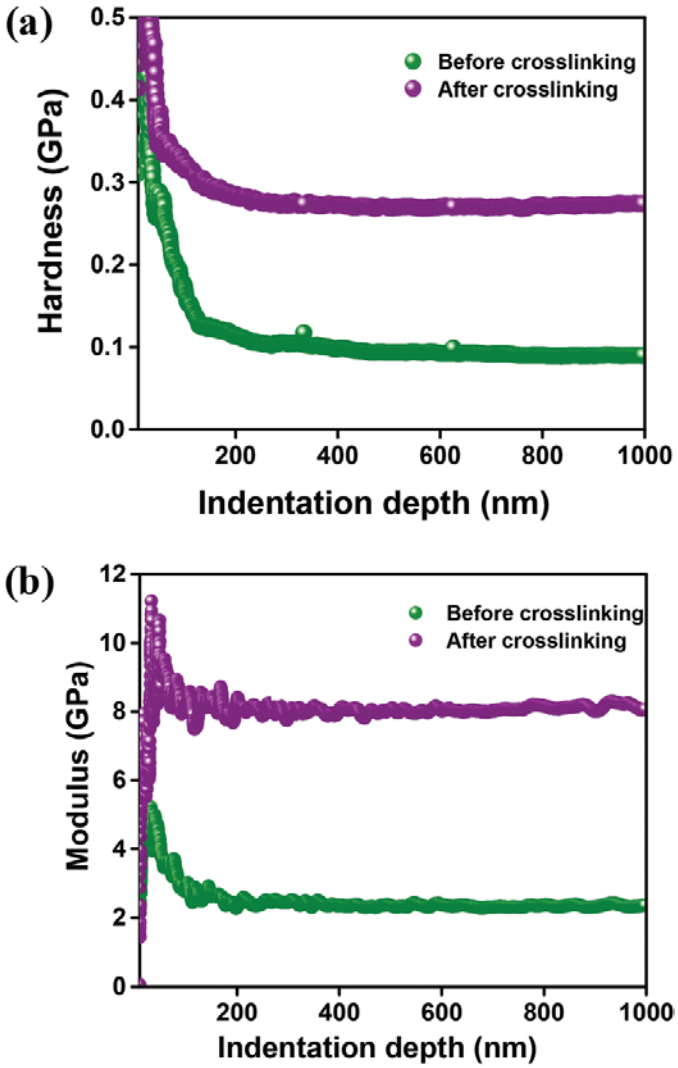

Figure 2-8. Nanoindentation measurement of TBA-TEVS-21 before and after crosslinking (a) hardness (b) elastic modulus.

	Before cross linking		After cross linking	
	Hardness (GPa)	Modulus (GPa)	Hardness (GPa)	Modulus (GPa)
TBA-TEVS-9	0.02 (±0.01)	1.1 (±0.2)	0.33 (±0.01)	8.1 (±0.2)
TBA-TEVS-21	0.09 (±0.01)	2.3 (±0.2)	0.27 (±0.01)	7.6 (±0.2)
TBA-TEVS-34	0.03 (±0.01)	1.7 (±0.2)	0.23 (±0.01)	6.1 (±0.2)
PAA	0.09 (±0.01)	3.8 (±0.2)	0.24 (±0.01)	6.5 (±0.2)

Table 2-1. Elastic modulus and hardness for TBA-TEVS-n binders in comparison with PAA

2.4 Conclusion

In summary, we have introduced poly(*tert*-butyl acrylate─*co*─triethoxyvinylsilane), TBA-TEVS-n, as a novel *in situ* cross-linkable polymeric binder for the Si anodes of LIBs. Systematic analysis with variation of each monomer in the polymer showed that 21% of triethoxyvinylsilane in the polymer, TBA-TEVS-21, produced superior performance as a binder compared with conventional polymeric binders and led to reduced pulverization. We have shown that the excellent performance of TBA-TEVS-21 is attributed to the formation of a 3D-interconnected network that is generated as a result of *in situ* crosslinking due to removal of the *tert*-butyl protecting group upon thermal treatment. The stable SEI formed during cycling, as indicated by CV, is also expected to contribute to the stable performance of TBA-TEVS-21. The SEM images indicate that the extent of silicon pulverization was reduced by up to 90% and the particles remained interconnected even after 100 cycles. Taken together, the present results demonstrate that developing 3D interconnected binder with the ability to maintain a stable SEI is an effective strategy to minimize electrode disintegration and thereby achieve stable performance of LIBs. TBA-TEVS-21 is thus proposed as a promising binder for high performance, practical LIBs.

2.5 Reference

1. Hossain, S.; Kim, Y.-K.; Saleh, Y.; Loutfy, R., Comparative studies of MCMB and C□C composite as anodes for lithium-ion battery systems. *Journal of Power Sources* **2003,** *114* (2), 264-276.
2. Obrovac, M. N.; Christensen, L., Structural Changes in Silicon Anodes during Lithium Insertion/Extraction. *Electrochemical and Solid-State Letters* **2004,** *7* (5), A93.
3. B. A. Boukamp, G. C. L., R. A. Huggins, All-Solid Lithium Electrodes with Mixed-Conductor Matrix. *Journal of Electrochemical Society: ELECTROCHEMICAL SCIENCE AND TECHNOLOGY* **1981,** *128* (4), 725-728.
4. Fuller, C. S.; Severiens, J. C., Mobility of Impurity Ions in Germanium and Silicon. *Physical Review* **1954,** *96* (1), 21-24.
5. Dimov, N.; Kugino, S.; Yoshio, M., Carbon-coated silicon as anode material for lithium ion batteries: advantages and limitations. *Electrochimica Acta* **2003,** *48* (11), 1579-1587.
6. Yoo, S.; Lee, J.-I.; Ko, S.; Park, S., Highly dispersive and electrically conductive silver-coated Si anodes synthesized via a simple chemical reduction process. *Nano Energy* **2013,** *2* (6), 1271-1278.
7. Lee, J.-I.; Ko, Y.; Shin, M.; Song, H.-K.; Choi, N.-S.; Kim, M. G.; Park, S., High-performance silicon-based multicomponent battery anodes produced via synergistic coupling of multifunctional coating layers. *Energy Environ. Sci.* **2015,** *8* (7), 2075-2084.
8. He, Y.; Yu, X.; Wang, Y.; Li, H.; Huang, X., Alumina-coated patterned amorphous silicon as the anode for a lithium-ion battery with high coulombic efficiency. *Advanced materials* **2011,** *23* (42), 4938-41.
9. Hwang, G.; Park, H.; Bok, T.; Choi, S.; Lee, S.; Hwang, I.; Choi, N. S.; Seo, K.; Park, S., A high-performance nanoporous Si/Al2O3 foam lithium-ion battery anode fabricated by selective chemical etching of the Al-Si alloy and subsequent thermal oxidation. *Chemical communications* **2015,** *51* (21), 4429-32.
10. Xiao Hua Liu, L. Z., Shan Huang, Scott X. Mao, Ting Zhu, Jian Yu Huang, Size-Dependent Fracture of Silicon Nanoparticles During Lithiation. *ACS nano* **2012,** *6* (2).
11. Yao, Y.; McDowell, M. T.; Ryu, I.; Wu, H.; Liu, N.; Hu, L.; Nix, W. D.; Cui, Y., Interconnected silicon hollow nanospheres for lithium-ion battery anodes with long cycle life. *Nano letters* **2011,** *11* (7), 2949-54.
12. Li-Feng Cui, R. R., Candace K. Chan, Hailin Peng, Yi Cui, Crystalline-Amorphous Core-Shell Silicon Nanowires for High Capacity and High Current Battery Electrodes. *Nano Letter* **2009,** *9* (1), 491-495.

13. Chan, C. K.; Peng, H.; Liu, G.; McIlwrath, K.; Zhang, X. F.; Huggins, R. A.; Cui, Y., High-performance lithium battery anodes using silicon nanowires. *Nature nanotechnology* **2008,** *3* (1), 31-5.
14. Kim, H.; Han, B.; Choo, J.; Cho, J., Three-dimensional porous silicon particles for use in high-performance lithium secondary batteries. *Angewandte Chemie* **2008,** *47* (52), 10151-4.
15. Chen, Z.; Christensen, L.; Dahn, J. R., Large-volume-change electrodes for Li-ion batteries of amorphous alloy particles held by elastomeric tethers. *Electrochemistry Communications* **2003,** *5* (11), 919-923.
16. Koo, B.; Kim, H.; Cho, Y.; Lee, K. T.; Choi, N. S.; Cho, J., A highly cross-linked polymeric binder for high-performance silicon negative electrodes in lithium ion batteries. *Angewandte Chemie* **2012,** *51* (35), 8762-7.
17. Ding, N.; Xu, J.; Yao, Y.; Wegner, G.; Lieberwirth, I.; Chen, C., Improvement of cyclability of Si as anode for Li-ion batteries. *Journal of Power Sources* **2009,** *192* (2), 644-651.
18. Li, J.; Lewis, R. B.; Dahn, J. R., Sodium Carboxymethyl Cellulose. *Electrochemical and Solid-State Letters* **2007,** *10* (2), A17.
19. Lestriez, B.; Bahri, S.; Sandu, I.; Roue, L.; Guyomard, D., On the binding mechanism of CMC in Si negative electrodes for Li-ion batteries. *Electrochemistry Communications* **2007,** *9* (12), 2801-2806.
20. Li, J.; Le, D.-B.; Ferguson, P. P.; Dahn, J. R., Lithium polyacrylate as a binder for tin–cobalt–carbon negative electrodes in lithium-ion batteries. *Electrochimica Acta* **2010,** *55* (8), 2991-2995.
21. Igor Kovalenko, B. Z., Alexandre Magasinski, Benjamin Hertzberg, Zoran Milicev, Ruslan Burtovyy, Igor Luzinov, Gleb Yushin, A Major Constituent of Brown Algae for Use in High-Capacity Li-Ion Batteries. *Science* **2011,** *334* (7), 75-79.
22. Wu, M.; Xiao, X.; Vukmirovic, N.; Xun, S.; Das, P. K.; Song, X.; Olalde-Velasco, P.; Wang, D.; Weber, A. Z.; Wang, L. W.; Battaglia, V. S.; Yang, W.; Liu, G., Toward an ideal polymer binder design for high-capacity battery anodes. *Journal of the American Chemical Society* **2013,** *135* (32), 12048-56.
23. Liu, G.; Xun, S.; Vukmirovic, N.; Song, X.; Olalde-Velasco, P.; Zheng, H.; Battaglia, V. S.; Wang, L.; Yang, W., Polymers with tailored electronic structure for high capacity lithium battery electrodes. *Advanced materials* **2011,** *23* (40), 4679-83.
24. Park, S. J.; Zhao, H.; Ai, G.; Wang, C.; Song, X.; Yuca, N.; Battaglia, V. S.; Yang, W.; Liu, G., Side-chain conducting and phase-separated polymeric binders for high-performance silicon anodes in lithium-ion batteries. *Journal of the American Chemical Society* **2015,** *137* (7), 2565-71.

25. Guo, J.; Wang, C., A polymer scaffold binder structure for high capacity silicon anode of lithium-ion battery. *Chemical communications* **2010,** *46* (9), 1428-30.
26. Song, J.; Zhou, M.; Yi, R.; Xu, T.; Gordin, M. L.; Tang, D.; Yu, Z.; Regula, M.; Wang, D., Interpenetrated Gel Polymer Binder for High-Performance Silicon Anodes in Lithium-ion Batteries. *Advanced Functional Materials* **2014,** *24* (37), 5904-5910.
27. Liu, J.; Zhang, Q.; Wu, Z. Y.; Wu, J. H.; Li, J. T.; Huang, L.; Sun, S. G., A high-performance alginate hydrogel binder for the Si/C anode of a Li-ion battery. *Chemical communications* **2014,** *50* (48), 6386-9.
28. Jeena, M. T.; Lee, J. I.; Kim, S. H.; Kim, C.; Kim, J. Y.; Park, S.; Ryu, J. H., Multifunctional molecular design as an efficient polymeric binder for silicon anodes in lithium-ion batteries. *ACS applied materials & interfaces* **2014,** *6* (20), 18001-7.
29. Jeong, Y. K.; Kwon, T. W.; Lee, I.; Kim, T. S.; Coskun, A.; Choi, J. W., Hyperbranched beta-cyclodextrin polymer as an effective multidimensional binder for silicon anodes in lithium rechargeable batteries. *Nano letters* **2014,** *14* (2), 864-70.
30. Magasinski, A.; Zdyrko, B.; Kovalenko, I.; Hertzberg, B.; Burtovyy, R.; Huebner, C. F.; Fuller, T. F.; Luzinov, I.; Yushin, G., Toward efficient binders for Li-ion battery Si-based anodes: polyacrylic acid. *ACS applied materials & interfaces* **2010,** *2* (11), 3004-10.
31. Xu, C.; Lindgren, F.; Philippe, B.; Gorgoi, M.; Björefors, F.; Edström, K.; Gustafsson, T., Improved Performance of the Silicon Anode for Li-Ion Batteries: Understanding the Surface Modification Mechanism of Fluoroethylene Carbonate as an Effective Electrolyte Additive. *Chemistry of Materials* **2015,** *27* (7), 2591-2599.
32. Peter L. Timms, R. A. K., Thomas C. Ehlert, John L. Margrave, Silicon-Fluorine Chemistry. I. Silicon Difluoride and the Perfluorosilanes. *Journal of the American Chemical Society* **1965,** *87*, *13*, 2824-2828.

Chapter III. An effective coupling of nanostructured Si and gel polymer electrolytes for high-performance lithium-ion battery anodes

3.1 Introduction

Lithium ion batteries (LIBs), owing to their high energy density and also well-tailored electrochemical properties, have garnered a great deal of attention as a compelling power source for a wide variety of mobile electronic devices[1]. Stimulated by the successful application to portable electronics including cellular phones and notebook computers, LIBs are now eager to pursue new application fields represented by electric vehicles (EVs) and grid-scale energy storage systems (ESSs)[2-4]. Unfortunately, their current technology level is not sufficient to fulfill the stringent requirements of the newly emerging application fields[5,6]. Among numerous material-based approaches to address this challenging issue, silicon has been the center of attention due to its exceptionally high theoretical capacity (3579 mAh g^{-1}, based on $Li_{15}Si_4$ at room temperature)[7] which is about one order of magnitude higher than that of commercially widespread graphite[8]. In addition, silicon is also characterized with other advantageous properties, including low cost, natural abundance, and relatively low lithiation voltage (~ 0.3 V)[9]. However, practical use of silicon as an anode material has been staggering due to its tremendously large volume expansion (~300%) during electrochemical lithiation-delithiation, eventually resulting in unwanted pulverization and disruption of electric/ionic conduction pathways[10-12].

Nanostructured silicon has drawn considerable attention as a promising way to resolve the aforementioned challenges of silicon anode materials. Benefiting from nano-scaled particle size (< 150 nm), the nano-silicon can accommodate the volume expansion-induced internal stress/strain[13], thus enabling substantial improvement in electrochemical performance. A rich variety of silicon morphologies have been developed, including nanoparticle[14], core-shell[15], thin film[16], nanowire[17], nanotube[18], nanosheet[19] and three-dimensional (3D) mesoporous/macroporous structure[20,21]. Core-shell structure consists of silicon core and inactive shell which can protect silicon surface from side reaction and/or increase electrical conductivity. Chan et al. reported that silicon nanowire can accommodate large strain without pulverization, providing good electronic contact and conduction channels, and displaying short lithium insertion distance[17]. Li et al. demonstrated that mesoporous sponge silicon, owing to its unique porous structure, can

significantly reduce the apparent volume expansion and thus prevent lithiation-induced pulverization[20]. Despite such remarkable advances mentioned above, commercial application of the nanostructured silicon materials reported to date still remains a formidable issue mainly due to synthesis complexity and processing cost.

In addition, major performance concerns of silicon materials are believed to arise from interface issues with electrochemically-vigorous liquid electrolytes (generally composed of linear/cyclic alkyl carbonate mixtures and lithium salts). The liquid electrolytes have many advantageous attributes suitable for commercial lithium-ion batteries, however, they still have critical safety concerns related to volatility and flammability[21-26] and also often give rise to interfacial side reactions with electrode materials[27]. Unfortunately, little attention has been paid to searching for alternative electrolytes that outperform the liquid electrolytes in the development of high-capacity silicon anodes.

Herein, we synthesize a variety of silicon anode materials featuring well-designed/precisely-controlled nanostructure (including mesoporous, micro-sized macroporous, two-dimensional (2D) sheet and urchin-like structure) and then combine them with chemically-crosslinked gel polymer electrolytes (GPEs) with an aim to pursue unprecedented synergistic coupling and its versatile applicability for high performance LIB anodes. Meanwhile, the GPE presented herein is *in-situ* synthesized through thermal crosslinking reaction in the presence of silicon materials inside a cell. A predetermined amount of ethoxylated trimethylopropane triacrylate (ETPTA) monomer which was chosen by considering the results of previous studies[28,29] is added into liquid electrolyte. The ETPTA monomer/liquid electrolyte mixture is then injected into the cell and subsequently the ETPTA monomer undergoes thermal crosslinking reaction to produce ETPTA polymer networks in the liquid electrolyte, leading to the GPE in close contact with the silicon materials. All of the silicon/GPE systems show significant improvement in cycling performance over control systems containing the silicon/liquid electrolyte. Notably, the silicon/GPE system exhibits a specific capacity of over 2000 mAh g^{-1} after 100 cycles, and also a half of volume change relative to the control system.

3.2 Experimental

Synthesis of nanostructured silicon materials.

Mesoporous silicon: 3D mesoporous silicon was synthesized *via* a metallothermic reduction reaction[21]. Firstly, silica foam was prepared according to the previous report[30]. 4 g of poly(ethylene oxide)-*b*-poly(propylene oxide)-*b*-poly(ethylene oxide) (PEO-*b*-PPO-*b*-PEO, Pluronic P-123, Sigma-Aldrich) triblock copolymer was dissolved in 150 mL of 1.6 M hydrochloric acid (HCl) solution at 35°C. Then, 1,3,5-trimethylbenzene (Mesitylene, Sigma-Aldrich) as a swelling agent was incorporated into the pre-prepared polymer solution, followed by the addition of 8.5 g of tetraethyl orthosilicate (TEOS, Sigma-Aldrich) as a silica precursor. The resulting solution was vigorously stirred for 24 hours, and maintained at 80°C for additional 24 hours. Final solid products were filtered and dried at 60°C in a convection oven. In order to remove residual polymers in the final products, calcination process was conducted at 600°C for 5 hours in oxygen environment. Subsequently, the resulting silica foam reacted with Mg (Sigma-Aldrich) at 700°C for 3 hours in argon-filled chamber. After the magnesiothermic reaction, MgO byproducts were completely removed by 1 M HCl solution at 35°C for 4 hours to obtain pure 3D mesoporous silicon.

Micro-sized macroporous silicon: 1 g of silica with macroporous structure (Diatomite, EP Minerals) was uniformly mixed with 0.8 g of Mg powder together in a stainless steel vessel under argon environment. The furnace was heated up to 700 °C at a rate of 5 °C min^{-1} and kept at this temperature for 3 hours. Then, the final product was immersed in a 1 M HCl solution at 35 °C for 4 hours to remove MgO byproducts.

Silicon sheet: Silicon sheet was prepared by magnesiothermic reaction of a phyllosilicate which is one of the clay minerals. 2 g of illite (alumino-silicate, Samwoo Chemical) was mixed with 1.6 g of Mg powder in argon-substituted vessel. The container was heated in the alumina tube furnace at 700 °C for 3 hours. In order to selectively remove the by-products, the final products were leached in 1 M HCl solution at 35 °C for 4 hours.

Fabrication of gel polymer electrolytes.

ETPTA (Mw = 428, Sigma-Aldrich) was mixed with liquid electrolyte (1M $LiPF_6$ in ethylene carbonate (EC)/diethyl carbonate (DEC), PANAX Starlyte) containing 10 wt.% of fluoroethylene carbonate (FEC) as an additive. The weight-based composition ratios of the ETPTA/liquid electrolyte were varied as 2/98, 3/97, 4/96 (w/w), wherein benzoyl

peroxide (BPO, 1.0 wt.% relative to the ETPTA content) was added as a radical initiator to allow thermal crosslinking reaction. The unit cells (2032-type coin) assembled with the silicon anodes and ETPTA monomer-containing liquid electrolytes were thermally cured at 60 ^{o}C for 30 min.

Physicochemical/electrochemical characterization.

Surface morphologies of as-prepared silica and silicon were characterized using a scanning electron microscopy (Cold FE-SEM S-4800, Hitachi). For transmission electron microscopy (TEM) measurement (JEM-1400), the silicon particles were dispersed in ethanol and transferred on a Cu grid. The crystalline structure of silicone materials was analyzed by X-ray diffraction (XRD) measurement using Cu Kα radiation from 10 to 90 two theta degrees. The thermal-crosslinking reaction of the GPE was investigated using a FT-IR spectrometer (FT-3000, Excalibur) with a spectral resolution of 4 cm^{-1}. The gel content of the GPE was estimated by measuring the weight loss of the samples after being solvent-extracted in dimethyl carbonate at 70^{o}C for 8 hours and subsequently in acetone at room temperature for 24 hours. The ionic conductivity (σ) of the GPE was obtained using an impedance analyzer (VSP classic, Bio-Logic) over a frequency range of 1 to 10^3 Hz under a temperature range 30 to 70^{o}C. The cyclic voltammetry of cells was examined using a potentiostat at a scan rate of 0.1 mV s^{-1}. The silicone anodes were fabricated by traditional slurry coating technique, wherein the composition ratio of the anodes was silicon active material (70 wt.%), Super-P as an electroconductive agent (15 wt.%) and poly(acrylic acid) (PAA)/sodium carboxymethyl cellulose (CMC) (= 1/1, 15 wt.%) as an anode binder. The electrochemical tests of half cells (= silicon anode/GPE/Li metal) were galvanostatically conducted from 0.01 and 1.2 V (versus Li/Li^+) at 0.05 and 0.2 C-rates using WBCS 3000 battery system (Wonatech).

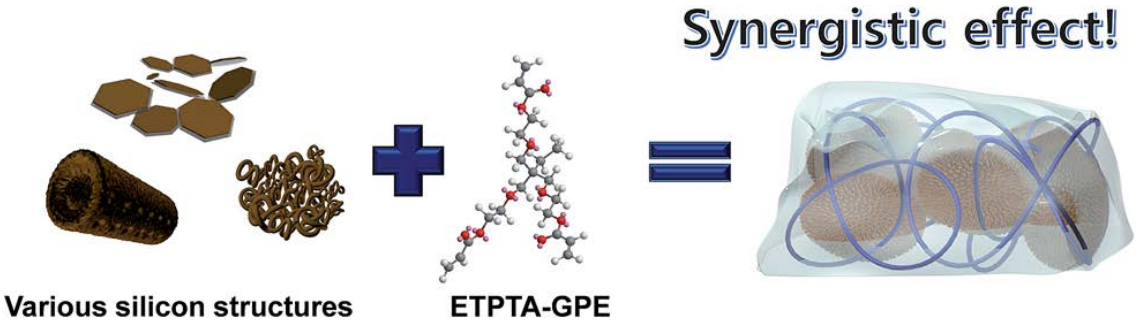

Scheme 3-1. Schematic illustration showing the synergistic coupling of various silicon anode materials (mesoporous, micro-sized macroporous, 2D sheet) and crosslinked ETPTA polymer-mediated GPEs.

3.3 Results and discussion

Micrometer-sized silicon anode materials are known to suffer from pulverization due to large volume expansion compared to nanostructured silicon ones[13]. In order to better understand advantageous effect of the silicon/GPE coupling and its versatile applicability, we prepared three different kinds of nanostructured silicon materials including mesoporous, micro-sized macroporous, 2D sheet (Scheme 1).

Mesoporous silicon

The mesoporous silica was synthesized by introducing silica precursors into self-assembled triblock copolymer template. Notably, the swelling agent (here, mesitylene) plays an important role in controlling pore size[31,32]. The use of swelling agent is known to be an effective way to generate numerous nanopores, providing high surface area (686.17 $m^2\ g^{-1}$) (ESI, fig. S1). The dimension of as-prepared silica foam consisted of nanometer-sized primary particles and micron-sized secondary particles (Fig. 1a and 1b). To make pure silica foam (starting material for magnesiothermic reaction), the triblock copolymer/silica mixtures were heated at 600 ^oC for 5 hours in O_2 environment. Subsequently, the 3D mesoporous silicon was synthesized *via* magnesiothermic reduction reaction, $SiO_2\,(s) + Mg\,(g) \rightarrow Si\,(s) + MgO\,(s)$ [33]. This chemical reduction is one of the simplest methods to make pure silicon. The MgO by-products were completely removed in HCl solution. The morphological characterization (Fig. 3-1c and 1d) of the resultant mesoporous silicon shows that primary silicon particles are aggregated due to the exothermal heat generated during the chemical reduction, compared to pristine silica foam. However, the overall size of secondary particles appears to be similar with that of the as-prepared silica ones. Moreover, the nano-sized silicon particles are interconnected together, maintaining interstitial voids formed between the particles (Fig. 3-1d). The interstitial voids may contribute to accommodating volume change of silicon anode during the repeated lithiation and delithiation process[34]. The XRD pattern (Fig. 3-1e) of an intermediate sample obtained after the magnesiothermic reduction shows the characteristic peaks corresponding to the silicon and MgO byproducts. This result indicates that the subsequent leaching with HCl solution leads to the successful formation of pure silicon.

Prior to combining the mesoporous silicon with the GPE, the physicochemical properties of the GPE were characterized. Increasing the ETPTA content in the GPEs exerted advantageous influence on the pulverization suppression and interfacial stability

with silicon anode materials, however, simultaneously caused the ionic conductivity loss. Taking into such a trade-off behavior of polymer content in the GPEs, the optimum content of polymer matrix was determined. Specifically, the GPE (containing 3 wt.% ETPTA) showed the best electrochemical performance, although its ionic conductivity was slightly lower than that of the GPE (with 2 wt.% ETPTA). First, the thermal-crosslinking reaction of the GPE was examined by observing the change in the FT-IR peaks assigned to acrylic C=C= bonds (1610-1625 cm^{-1}) of the ETPTA monomer before/after thermal-curing[35,36]. Figure 3-2b shows that the characteristic FT-IR peaks of the acrylic C=C bonds in the GPE disappeared after the thermal curing. This result verifies the successful thermal-polymerization of ETPTA monomer, which was further confirmed by measuring the gel content of the GPEs. The gel content (i.e. insoluble polymer fraction after solvent (dimethyl carbonate and acetone extraction) of the GPE was observed to be more than 99 %, which demonstrates that the thermal-crosslinking reaction of the ETPTA monomer in the GPEs is almost completed. The mechanical flexibility of the GPE was shown in fig. 3-2a and movie (ESI, movie S1). The GPEs featuring these unique physical properties are expected to act as a mechanical cushion which can alleviate the large volume change of silicon anode during the battery operation.

The temperature-dependent ionic conductivity of the GPE is compared with that of the liquid electrolyte containing no ETPTA polymer. Both the GPE and the liquid electrolyte show excellent ionic conductivities over a wide range of temperature (fig. 3-2c). Notably, the ionic conductivity of the GPE (incorporating 2 wt.% ETPTA) appears to be similar to that of the liquid electrolyte, indicating that the presence of the ETPTA polymer does not exert harmful influence on ion transport in the GPE. Such good ionic conductivity of the GPE can be explained by the unique role of the ETPTA polymer network. Specifically, the ETPTA polymer may have strong interaction with lithium ions due to the presence of nine oxygen atoms of ETPTA molecule, possibly facilitating the dissociation of lithium salts[36,37]. In addition, the electrochemical stability window of the GPE was examined by analyzing the cyclic voltammetry (Fig. 3-2d). No significant decomposition of any components in the GPE takes place in the range of 0.01-1.2 V (vs. Li/Li^+), ensuring that the GPE could be electrochemically combined with the silicon anode.

The potential application of the GPE to the mesoporous silicon anode was explored in terms of cell performance. The first galvanostatic voltage profile was shown at discharge/charge current density of 0.05 C/0.05 C (Fig. 3-2e). It is of note that the GPE with 2 wt.% ETPTA presents the larger initial capacity than the liquid electrolyte. However, the GPE (2 wt.% ETPTA) showed a sharp decay in the capacity retention after 66^{th} cycle.

In contrast, the GPEs containing the higher amount (3 and 4 wt.%) of ETPTA presented better cycling stability. In particular, the improvement in the cycling performance was remarkable at the GPE (3 wt.% ETPTA)(capacity retention for GPE is 92%, while the cell using liquid electrolyte showed 80 % of retention after 100 cycles). The relatively inferior capacity retention of the GPE (4 wt.% ETPTA) may be ascribed to its lower ionic conductivity (Fig. 3-2c). This result exhibits that the GPEs, which are characterized with the superior elasticity over the liquid electrolyte (Fig. 3-2a), can act as an exceptional mechanical cushion to accommodate the volume change of silicon inevitably generated during the lithiation-delithiation reaction, demonstrating the unusual synergistic coupling of mesoporous silicon and GPE (3 wt.% ETPTA).

Micro-sized, macroporous Si

The micrometer-sized 3D macroporous silicon was synthesized *via* magnesiothermic reaction. Macroporous silica (Diatomite) is composed of 90% of silica, 5% of alumina, 1% of iron oxide and trace amounts of different kinds of oxides. According to the Ellingham diagram[38], all of the oxides mentioned above can be converted to reduced species by magnesium vapor. When the molar ratio of silica to magnesium during the magnesiothermic reaction is higher than 1.25, excess Mg reacts with Si product or unreacted silica to generate additional Mg_2Si or Mg_2SiO_4, respectively. The Mg_2Si can be easily removed by HCl treatment[39], however, the HCl is not a suitable etchant for Mg_2SiO_4. If the Mg_2SiO_4 byproducts, which are electrochemically inert with lithium ions, may not completely removed, the loss of specific capacity of the resultant micro-sized macroporous silicon is difficult to avoid.

Diatomite has a unique shape which is a hollow cylinder (over 15 μm in height) with thick frame (<3 μm), and numerous narrow channels (several hundred nanometer in diameter), as shown in Fig. 3-3a. After the magnesiothermic reaction and subsequent HCl treatment, the micro-sized macroporous silicon and MgO byproducts were produced without any shape-deformation. The XRD pattern displays that the crystalline phases are exclusively assigned to pure silicon without any other impurities (ESI, fig. S2). The micro-sized macroporous silicon particles have large numbers of pores which may alleviate the volume change of silicon (inset of fig. 3-3b). The voltage profiles at 1st cycle (discharge/charge current density = 0.05 C/0.05 C, an inset of fig. 3-3c) show no significant difference in the capacity between the GPE (3 wt.% ETPTA) and liquid electrolyte. However, as the cycle number was increased, the cell containing the GPE provided the substantial improvement in the cycling performance (capacity after 100 cycles = 1191 mAh g^{-1}, fig. 3-3c), while the cell with the liquid electrolyte showed the

sharp capacity decay (~ 800 mAh g^{-1}). This result demonstrates the advantageous effect of the GPE on the long-term electrochemical performance of the micro-sized macroporous silicon anode. Moreover, the cell assembled with the GPE showed the excellent discharge rate capability (e.g., capacity retention at 5.0 C (vs. at 0.2 C) ~ 80%, fig. 3-3d).

Silicon sheet

The 2D silicon sheet was synthesized through magnesiothermic reaction of illite, one of the layered clay minerals. The chemical formula of illite is $(K, H_3O)(Al, Mg, Fe)_2(Si, Al)_4O_{10}[(OH)_2, (H_2O)]$. And, the composition ratio of illite is 47% of silica, 23.3% of alumina, 10% of iron oxide, 6.7% of potassium oxide and so on[40]. It consists of thin single unit layers which are piled up to 20 μm in height (fig. 3-4a). During the magnesiothermic reaction, the layers of illite are partially exfoliated and subsequently converted to 2D silicon sheet structure with thickness of 10 μm (fig. 3-4b). The XRD patterns (fig. 3-4c) of the resulting 2D silicon sheets show the successful formation of pure silicon (that was synthesized from illite). The coupling effect of the silicon sheet and GPE on the electrochemical performance was investigated.

The silicon sheet combined with the GPE (3 wt.% ETPTA) showed the higher initial capacity (= 1469 mAh g^{-1}) than that with the liquid electrolyte (= 1137 mAh g^{-1}) (inset of fig. 3-4d). This beneficial effect of the GPE over the liquid electrolyte could be attributed to physical tightening of the silicon sheets by the crosslinked elastic GPE, thereby allowing larger amount of silicon active materials to participate in the discharge/charge reaction. The 2D silicon sheet combined with the GPE also showed the stable cycling performance (capacity retention ~ 65 % after 150 cycles at 0.2 C/0.2 C, fig. 3-4d). Interestingly, when carbon-coated Si sheets anode (with carbon contents of 10 wt.%) was combined with GPE electrolytes, outstanding cycling retention (nearly capacity retention of 100% after 200 cycles at 0.5 C rate) was shown compared to electrode combined with liquid electrolyte (fig. 3-4e).

Volume change of silicon anodes before/after cycling

To better understand the unique role of the GPE as a mechanical cushion that can alleviate the volume change-induced internal stress of silicon materials during the repeated cycling, the cross-sectional morphologies of silicon anodes before/after cycling test (100 cycles) were analyzed (fig. 5).

It is of note that the GPE, as compared to the liquid electrolyte, remarkably su ppressed the volume expansion of the silicon anodes. Specifically, the volume exp ansion (after 100 cycles) was found to be 131 % vs. 65 % (liquid electrolyte vs. GPE) for the mesoporous silicon anodes, 187 % vs. 134 % for the micro-sized

macroporous silicon, and 195 % vs. 101 % for the silicon sheet. This result demonstrates that the GPE effectively acts as a mechanical cushion to accommodate the volume change (leading to pulverization) of silicon and also preserve the electronic/ionic conduction pathways, eventually providing significant improvement in the long-term cycling performance of the nanostructured silicon materials.

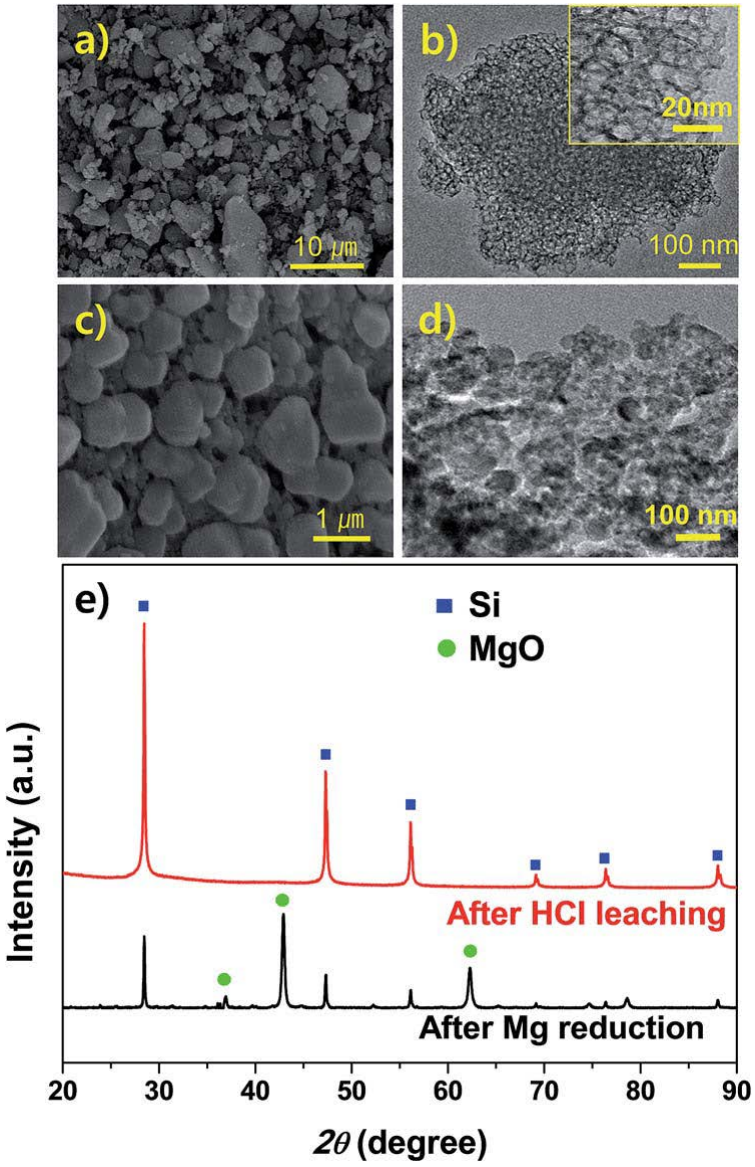

Figure 3-2. (a) SEM and (b) TEM images of silica form obtained by heat treatment at 600 C under air. An inset in the (b) shows the foam-like structure. (c) SEM and (d) TEM images of mesoporous silicon particles synthesized by magnesiothermic reaction of silica form. (e) XRD patterns of mesoporous silicon and MgO by-product after Mg reduction and HCl leaching process, respectively.

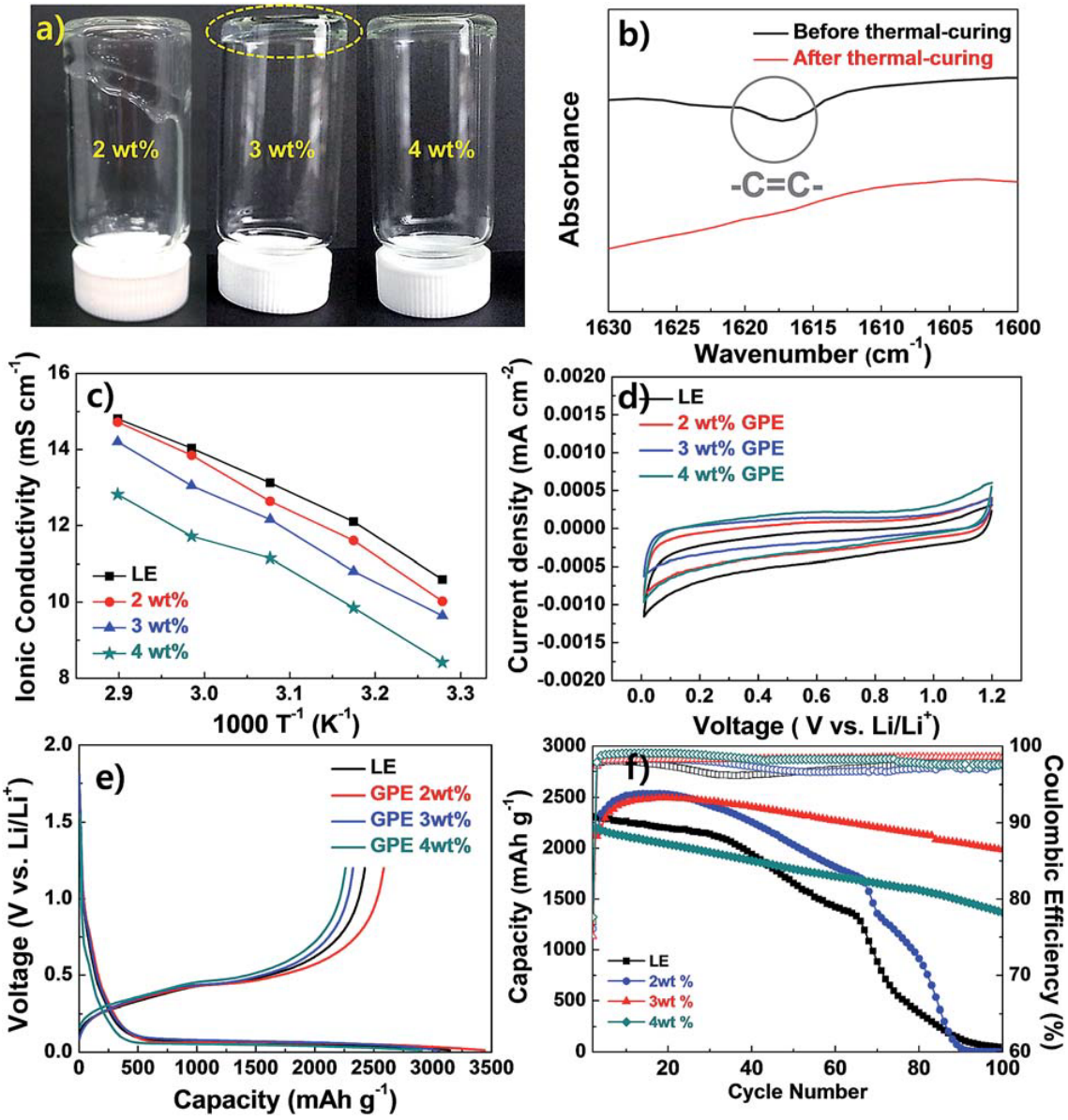

Figure 3-3. (a) Physical appearance of GPE as a function of the incorporated ETPTA content. (b) FT-IR spectra of acrylic C]C double bonds of ETPTA monomer before/after thermal-curing. (c) Temperature-dependent ionic conductivity of GPEs and liquid electrolyte. (d) Cyclic voltammograms of GPEs and liquid electrolyte. (e) Discharge/charge profiles of half cells assembled with mesoporous silicon anode and GPEs at 1st cycle and (f) cycling performance of half cells at discharge/charge current density of 0.2C/0.2C under voltage range of 0.01–1.2 V.

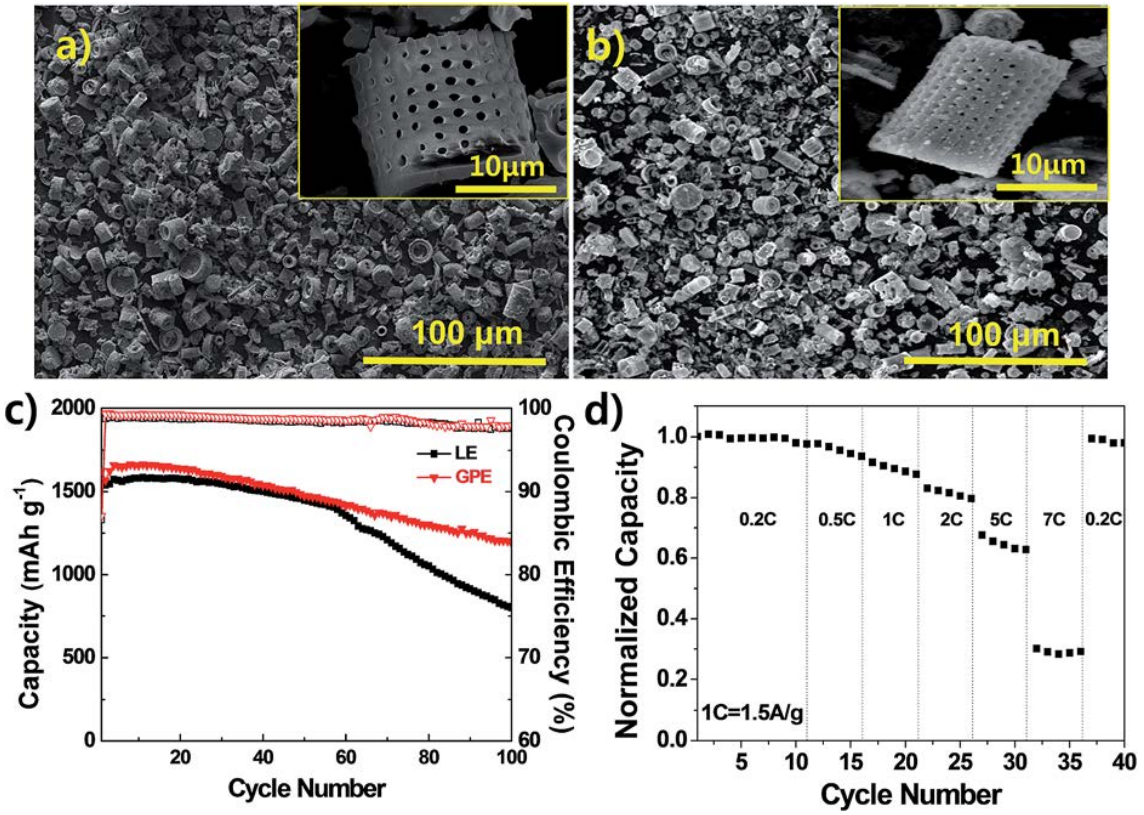

Figure 3-4. (a) SEM image of micro-sized macroporous diatomite. An inset shows the macrospores and smooth silica surface. (b) SEM image of micro-sized macroporous silicon synthesized via magnesiothermic reaction of diatomite. An inset is the XRD pattern indicating the formation of pure silicon particles. (c) Cycling performance of micro-sized macroporous silicon anodes combined with GPE (3 wt.% ETPTA) or liquid electrolyte. An inset shows the first cycle voltage profiles. (d) Charge rate capability of micro-sized macroporous silicon anode combined with GPE (3 wt.% ETPTA).

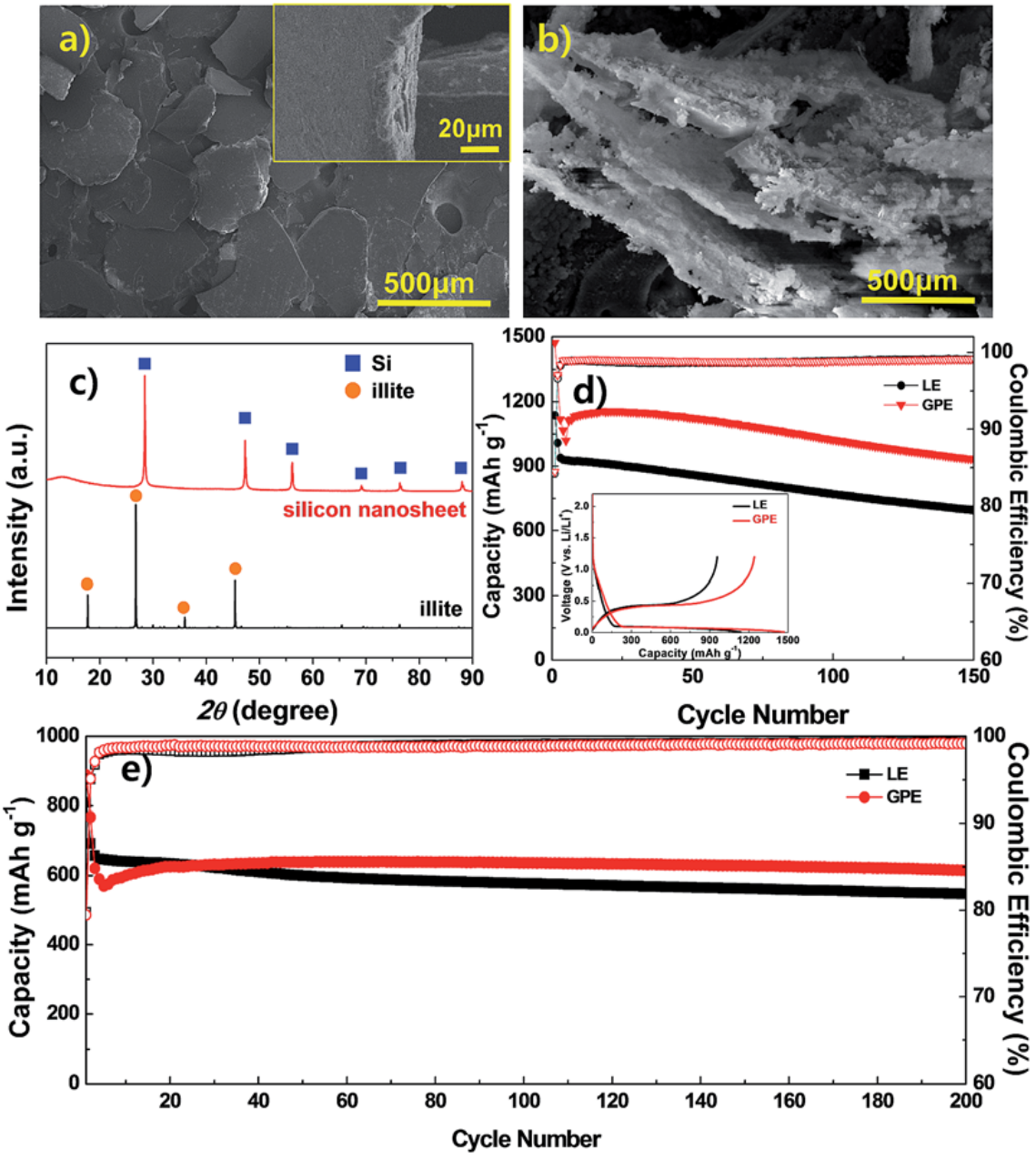

Figure 3-5. (a) SEM images of pristine illite showing sheet-like structure. (b) SEM image of 2D silicon sheets synthesized through magnesiothermic reduction of illite. (c) XRD patterns of illite and 2D silicon sheet. (d) Cycling performance of 2D silicon sheet combined with GPE or liquid electrolyte. An inset shows the discharge/charge voltage profiles at 1st cycle. (e) Cycling performance of carbon-coated 2D silicon sheets combined with two different electrolytes.

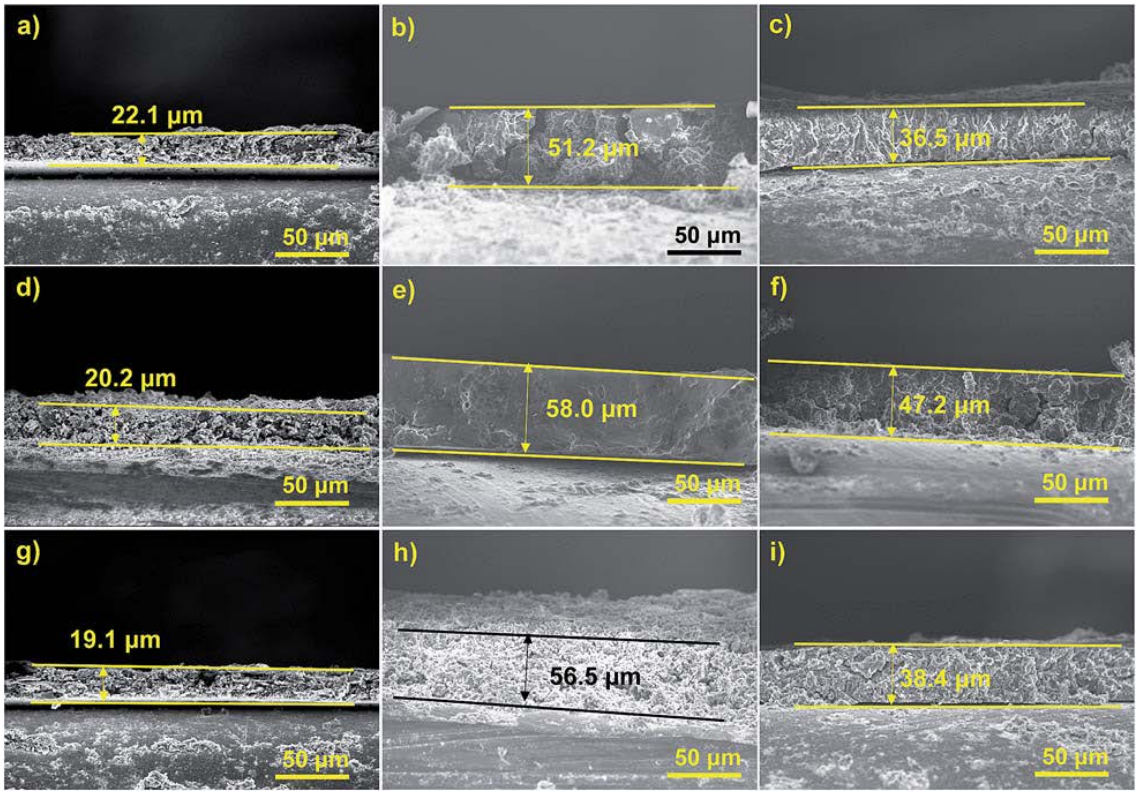

Figure 3-6. Cross-sectional SEM images showing the volume expansion of various silicon anodes (1st column: as-prepared anodes, 2nd column: anodes containing liquid electrolyte after 100 cycles, 3rd column: anodes containing GPE after 100 cycles). SEM images of (a–c) mesoporous silicon, (d–f) micro-sized macroporous silicon, and (g–i) silicon sheet.

3.4 Conclusion

We demonstrated the coupling effect of nanostructured silicon materials and GPEs for high-performance lithium-ion battery anodes. For all of the silicon anode systems, the GPE showed the significant improvement in the cycling retention, up to 60% higher in case of mesoporous silicon, than the liquid electrolyte. The chemically-crosslinked ETPTA-mediated elastic GPE acted as a mechanical cushion which can alleviate the volume change of silicon anodes during the repeated cycling and stabilized the interface of silicon materials. More notably, the GPE enabled the remarkable suppression (1.5 or 2 times less) in volume expansion of the silicon anodes during the cycling. For more detail, electrochemical results of above cells was compiled in the table S1. We anticipate that this coupling strategy based on the nanostructured silicon and the chemically-crosslinked elastic GPE is effective and also versatile, which thereupon can be easily applicable to a vast variety of silicon anode materials suffering from electrochemical pulverization concerns.

3.5 Reference

1. Tarascon, M. A. a. J.-M., Building better batteries. *Nature* **2008,** *451*, 652-657.
2. Poizot, P.; Laruelle, S.; Grugeon, S.; Dupont, L.; Tarascon, J., Nano-sized transition-metal oxides as negative-electrode materials for lithium-ion batteries. *Nature* **2000,** *407* (6803), 496-499.
3. Dyer, C. K., Fuel cells for portable applications. *Fuel Cells Bulletin* **2002,** *2002* (3), 8-9.
4. Endo, M.; Kim, C.; Nishimura, K.; Fujino, T.; Miyashita, K., Recent development of carbon materials for Li ion batteries. *Carbon* **2000,** *38* (2), 183-197.
5. Liu, C.; Li, F.; Ma, L. P.; Cheng, H. M., Advanced materials for energy storage. *Advanced materials* **2010,** *22* (8).
6. Thackeray, M. M.; Wolverton, C.; Isaacs, E. D., Electrical energy storage for transportation—approaching the limits of, and going beyond, lithium-ion batteries. *Energy & Environmental Science* **2012,** *5* (7), 7854-7863.
7. Obrovac, M. N.; Christensen, L., Structural Changes in Silicon Anodes during Lithium Insertion/Extraction. *Electrochemical and Solid-State Letters* **2004,** *7* (5), A93.
8. Hossain, S.; Kim, Y.-K.; Saleh, Y.; Loutfy, R., Comparative studies of MCMB and C□ C composite as anodes for lithium-ion battery systems. *Journal of power sources* **2003,** *114* (2), 264-276.
9. Liu, X. H.; Zheng, H.; Zhong, L.; Huang, S.; Karki, K.; Zhang, L. Q.; Liu, Y.; Kushima, A.; Liang, W. T.; Wang, J. W.; Cho, J. H.; Epstein, E.; Dayeh, S. A.; Picraux, S. T.; Zhu, T.; Li, J.; Sullivan, J. P.; Cumings, J.; Wang, C.; Mao, S. X.; Ye, Z. Z.; Zhang, S.; Huang, J. Y., Anisotropic swelling and fracture of silicon nanowires during lithiation. *Nano letters* **2011,** *11* (8), 3312-8.
10. Beaulieu, L.; Hatchard, T.; Bonakdarpour, A.; Fleischauer, M.; Dahn, J., Reaction of Li with alloy thin films studied by in situ AFM. *Journal of The Electrochemical Society* **2003,** *150* (11), A1457-A1464.
11. Beaulieu, L.; Eberman, K.; Turner, R.; Krause, L.; Dahn, J., Colossal reversible volume changes in lithium alloys. *Electrochemical and Solid-State Letters* **2001,** *4* (9), A137-A140.
12. Ge, M.; Rong, J.; Fang, X.; Zhou, C., Porous doped silicon nanowires for lithium ion battery anode with long cycle life. *Nano letters* **2012,** *12* (5), 2318-2323.
13. Xiao Hua Liu, L. Z., Shan Huang, Scott X. Mao, Ting Zhu, Jian Yu Huang, Size-Dependent Fracture of Silicon Nanoparticles During Lithiation. *ACS nano* **2012,** *6* (2), 1522–1531.
14. Wang, C.; Wu, G.; Zhang, X.; Qi, Z.; Li, W., Lithium insertion in carbon-silicon composite materials produced by mechanical milling. *Journal of the Electrochemical Society* **1998,** *145*

(8), 2751-2758.

15. Gao, P.; Fu, J.; Yang, J.; Lv, R.; Wang, J.; Nuli, Y.; Tang, X., Microporous carbon coated silicon core/shell nanocomposite via in situ polymerization for advanced Li-ion battery anode material. *Physical Chemistry Chemical Physics* **2009,** *11* (47), 11101-11105.
16. Ohara, S.; Suzuki, J.; Sekine, K.; Takamura, T., A thin film silicon anode for Li-ion batteries having a very large specific capacity and long cycle life. *Journal of Power Sources* **2004,** *136* (2), 303-306.
17. Chan, C. K.; Peng, H.; Liu, G.; McIlwrath, K.; Zhang, X. F.; Huggins, R. A.; Cui, Y., High-performance lithium battery anodes using silicon nanowires. *Nature nanotechnology* **2008,** *3* (1), 31-5.
18. Park, M.-H.; Kim, M. G.; Joo, J.; Kim, K.; Kim, J.; Ahn, S.; Cui, Y.; Cho, J., Silicon nanotube battery anodes. *Nano letters* **2009,** *9* (11), 3844-3847.
19. Fu, K.; Yildiz, O.; Bhanushali, H.; Wang, Y.; Stano, K.; Xue, L.; Zhang, X.; Bradford, P. D., Aligned carbon nanotube-silicon sheets: A novel nano-architecture for flexible lithium ion battery electrodes. *Advanced materials* **2013,** *25* (36), 5109-5114.
20. Li, X.; Gu, M.; Hu, S.; Kennard, R.; Yan, P.; Chen, X.; Wang, C.; Sailor, M. J.; Zhang, J.-G.; Liu, J., Mesoporous silicon sponge as an anti-pulverization structure for high-performance lithium-ion battery anodes. *Nature communications* **2014,** *5*.
21. Choi, S.; Bok, T.; Ryu, J.; Lee, J.-I.; Cho, J.; Park, S., Revisit of metallothermic reduction for macroporous Si: compromise between capacity and volume expansion for practical Li-ion battery. *Nano Energy* **2015,** *12*, 161-168.
22. Xu, K., Nonaqueous liquid electrolytes for lithium-based rechargeable batteries. *Chemical reviews* **2004,** *104* (10), 4303-4418.
23. Tarascon, J.-M.; Gozdz, A.; Schmutz, C.; Shokoohi, F.; Warren, P., Performance of Bellcore's plastic rechargeable Li-ion batteries. *Solid State Ionics* **1996,** *86*, 49-54.
24. Sato, T.; Maruo, T.; Marukane, S.; Takagi, K., Ionic liquids containing carbonate solvent as electrolytes for lithium ion cells. *Journal of Power Sources* **2004,** *138* (1), 253-261.
25. Mandal, B. K.; Padhi, A. K.; Shi, Z.; Chakraborty, S.; Filler, R., Thermal runaway inhibitors for lithium battery electrolytes. *Journal of Power Sources* **2006,** *161* (2), 1341-1345.
26. Murata, K.; Izuchi, S.; Yoshihisa, Y., An overview of the research and development of solid polymer electrolyte batteries. *Electrochimica acta* **2000,** *45* (8), 1501-1508.
27. Kim, J.-M.; Park, J.-H.; Lee, C. K.; Lee, S.-Y., Multifunctional semi-interpenetrating polymer network-nanoencapsulated cathode materials for high-performance lithium-ion batteries. *Scientific reports* **2014,** *4*.
28. Kil, E. H.; Ha, H. J.; Lee, S. Y., A Facile Approach to Fabricate Self-Standing Gel-Polymer

Electrolytes for Flexible Lithium-Ion Batteries by Exploitation of UV-Cured Trivalent/Monovalent Acrylate Polymer Matrices. *Macromolecular Chemistry and Physics* **2011,** *212* (20), 2217-2223.

29. Ha, H.-J.; Kwon, Y. H.; Kim, J. Y.; Lee, S.-Y., A self-standing, UV-cured polymer networks-reinforced plastic crystal composite electrolyte for a lithium-ion battery. *Electrochimica Acta* **2011,** *57*, 40-45.
30. Kim, H.; Jung, J. C.; Kim, P.; Yeom, S. H.; Lee, K.-Y.; Song, I. K., Preparation of H 3 PMo 12 O 40 catalyst immobilized on surface modified mesostructured cellular foam (SM-MCF) silica and its application to the ethanol conversion reaction. *Journal of Molecular Catalysis A: Chemical* **2006,** *259* (1), 150-155.
31. Bok, T.; Choi, S.; Lee, J.; Park, S., Effective strategies for improving the electrochemical properties of highly porous Si foam anodes in lithium-ion batteries. *J. Mater. Chem. A* **2014,** *2* (34), 14195-14200.
32. Zhao, D.; Feng, J.; Huo, Q.; Melosh, N.; Fredrickson, G. H.; Chmelka, B. F.; Stucky, G. D., Triblock copolymer syntheses of mesoporous silica with periodic 50 to 300 angstrom pores. *science* **1998,** *279* (5350), 548-552.
33. Bao, Z.; Weatherspoon, M. R.; Shian, S.; Cai, Y.; Graham, P. D.; Allan, S. M.; Ahmad, G.; Dickerson, M. B.; Church, B. C.; Kang, Z., Chemical reduction of three-dimensional silica micro-assemblies into microporous silicon replicas. *Nature* **2007,** *446* (7132), 172-175.
34. Liu, N.; Lu, Z.; Zhao, J.; McDowell, M. T.; Lee, H.-W.; Zhao, W.; Cui, Y., A pomegranate-inspired nanoscale design for large-volume-change lithium battery anodes. *Nature nanotechnology* **2014,** *9* (3), 187-192.
35. Ha, H.-J.; Kil, E.-H.; Kwon, Y. H.; Kim, J. Y.; Lee, C. K.; Lee, S.-Y., UV-curable semi-interpenetrating polymer network-integrated, highly bendable plastic crystal composite electrolytes for shape-conformable all-solid-state lithium ion batteries. *Energy & Environmental Science* **2012,** *5* (4), 6491-6499.
36. Kim, S.-H.; Choi, K.-H.; Cho, S.-J.; Kil, E.-H.; Lee, S.-Y., Mechanically compliant and lithium dendrite growth-suppressing composite polymer electrolytes for flexible lithium-ion batteries. *Journal of Materials Chemistry A* **2013,** *1* (16), 4949-4955.
37. Choi, K. H.; Cho, S. J.; Kim, S. H.; Kwon, Y. H.; Kim, J. Y.; Lee, S. Y., Thin, Deformable, and Safety-Reinforced Plastic Crystal Polymer Electrolytes for High-Performance Flexible Lithium-Ion Batteries. *Advanced Functional Materials* **2014,** *24* (1), 44-52.
38. Ellingham, H. J. T., Reducibility of oxides and sulfides in metallurgical processes. *J Soc Chem Ind* **1944,** *63*, 125-133.
39. Chen, W.; Fan, Z.; Dhanabalan, A.; Chen, C.; Wang, C., Mesoporous silicon anodes prepared

by magnesiothermic reduction for lithium ion batteries. *Journal of The Electrochemical Society* **2011,** *158* (9), A1055-A1059.

40. Bell, T., Microstructure in mixed-layer illite/smectite and its relationship to the reaction of smectite to illite. *CLAYS CLAY MINER. Clays Clay Miner.* **1986,** *34* (2), 146.

Chapter IV. Effective strategies for improving the electrochemical properties of highly porous Si foam anodes in lithium-ion batteries

4.1 Introduction

Currently, rechargeable lithium-ion batteries (LIBs) are the dominant power sources for medical and portable electronic devices, such as laptop computers, mobile phones, camcorders, and radio frequency identification.[1-3] Furthermore, the development of next-generation LIBs with high energy density and long cycle life is of great technological importance to be used in hybrid vehicles, plug-in hybrid vehicles, electric vehicles, and renewable energy storage system[4-6]. To meet the requirements of next-generation LIBs, the electrode materials must have high specific gravimetric/volumetric capacities, a high power density, and a long cycling life.[4-6]

The increasing demand for high-performance LIBs has driven intense interest in developing significantly improved electrode materials. At present, various carbonaceous anode materials have been used in commercial LIBs, however, the low theoretical capacity (372 mAh g^{-1}) cannot satisfy the demand of next-generation LIBs.[7, 8] Among the available candidate materials exhibiting a high storage capacity, silicon (Si) is the most promising anode material owing to its high theoretical capacity (4200 mAh g^{-1}, an order magnitude higher than that of graphite), relatively low working potential (<0.5 V vs. Li/Li^+), natural abundance, and environmentally friendliness.[9] Even though Si anode materials have many advantages mentioned above, it has a fatal weakness for the practical application in LIBs. The major drawback of Si anode is a large volume change (>300%) that occurs during lithiation and delithiation process. The repeated cycling can generate an enormous mechanical stress within the Si material, leading to severe cracking and pulverization of the electrode. Consequently, the Si electrode results in a significant capacity fading due to the electrical disconnection of the electrode from the current collector.[10] Other disadvantages of the Si anode are low intrinsic electrical conductivity and low lithium diffusion rate.[11, 12]

In order to solve the problems related to Si anodes, great efforts have been devoted to mitigating the pulverization of Si and enhancing electrical conductivity of Si by developing several strategies, including nanostructuring (e.g., nanoparticles, nanowires, nanotubes, hollow spheres), porous structures, nanocomposites, coating of Si active materials with conductive materials (e.g., carbon, graphene, carbon nanotubes, metals, conducting polymers), application of electrolyte additive, and synthesis of new binders.[13-20]

Nanostructured Si have been used to reduce mechanical stress that occurs during cycling, resulting in accommodation of a large volume change of Si, which in turn significantly improved a long-term cyclability. It also provides other benefits, including short Li-ion diffusion length within the electrode and improved rate capability due to the large surface area, compared to micron-sized Si.[21,22] However, nanostructured Si faces some challenges to be solved. Nano-sized Si with high surface area shows undesired side-reaction on the Si surface, thermal runaway, and low volumetric energy density, which are obstacles for practical LIB applications.[21, 22]

To solve these critical issues, one of the best solutions is to combine micro- and nano-scale materials to capitalize on advantages and restrain drawbacks of the two components. Several examples have been reported including nanostructuring of micrometer-sized Si particles, dispersion of nano-sized Si in carbon matrix, self-assembly of nanoscale Si and carbon, template-based chemical synthesis of porous Si, three-dimensionally (3D) interconnection of one-dimensional Si structures.[23-27] Among these approaches, porous Si structure has been proven to be highly efficient as follows: (i) void space of the pores accommodates a volume expansion to reduce the mechanical stress during cycling, resulting in attainment of a stable cycling and (ii) porous regions increase the accessibility of electrolyte and lithium ions to shorten lithium ion diffusion distance within the electrodes, leading to a high rate capability.[28-31]

For example, Kim et al. synthesized a 3D macroporous Si using silica (SiO_2) particle template which exhibited a reversible specific capacity of 2800 mAh g^{-1} at 1 C rate with excellent cycling performance (capacity retention of 90% at 1 C rate after 100 cycles). However, the high-cost and low yield (~5%) synthetic process may hinder its large scale production.[26] Recently, Jia et al. prepared a 3D mesoporous Si material with a lotus-like morphology using a magnesiothermic reduction method. Subsequent carbon-coated mesoporous Si composite showed a stable capacity of ~1500 mAh g^{-1} for 100 cycles at 1 C rate and a high rate capability up to 15 C rate. However, the existence of numerous mesopores may induce a serious side-reaction and may not effectively accommodate a large volume expansion during cycling.[31]

Herein, we demonstrate facile, inexpensive, and effective strategies to enhance the electrochemical performances of highly porous Si foam anode in lithium-ion batteries. Firstly, we synthesize a hierarchical Si foam structure via a magnesiothermic reduction of micrometer-sized SiO_2 foam particles obtained by controlling calcination process. Secondly, we introduce a heat scavenging molten salt during the chemical reduction reaction to minimize exothermic heat, leading to a successful synthesis of shape-preserving Si foam particles. Thirdly, electrically conductive metal nanoparticles are introduced within Si foam particles, and subsequent chemical reduction process leads to a formation of metal-doped Si foam particles. The Si foam anodes

obtained by these strategies exhibit a high reversible capacity (>1500 mAh g^{-1}) and a highly stable cycling retention (> 90% after 100 cycles at 0.2 C rate).

4.2 Experimental

Preparation of highly porous Silica foam

Silica foam was prepared according to the previously reported method.[32] Typically, 4 g of poly(ethylene oxide)-b-poly(propylene oxide)-b-poly(ethylene oxide) (PEO-b-PPO-b-PEO) triblock copolymer (Pluronic P123, Sigma-Aldrich), a polymer template, was dissolved in 150 ml of 1.6 M HCl solution at 35 ºC. 4 g of 1,3,5-trimethylbenzene (Mesitylene, Sigma-Aldrich), a swelling agent, was added into the solution containing the copolymer template. The mixed solution was then slowly added into 8.5 g of tetraethylorthosilicate (TEOS, Sigma-Aldrich), a silica precursor. The resulting solution was vigorously stirred for 24 h, and then it was maintained at 80 ºC for 24 h. Finally, the solid product was filtered and dried at room temperature. As-prepared silica/polymer product was divided into three alumina boat to be calcined to make hierarchical silica particles. To control the amount of residual carbon after calcination, we used three different calcination processes (first portion: no calcination, second portion: 600 ºC for 2 h in ambient, and third portion: 600 ºC for 5 h in oxygen environment). Subsequently, three different silica samples were reacted with Mg vapor via magnesiothermic reduction at 700 ºC for 3 h in an argon-filled alumina vessel to make porous Si particles.

Characterization of silica and Si foam particles

Microstructure of as-synthesized silica foam and converted Si foam particles were investigated by a normal X-ray diffractometer (Bruker D8 Advance). The internal morphologies of the silica and the Si foam were analyzed by transmission electron microscopy (TEM, JEM-1400) at an acceleration voltage of 120 kV. For the TEM measurement, the silica and Si particles were dispersed in ethanol, then transferred on to a Formvar-coated copper grid. The surface morphologies of the silica and Si foam were characterized by a scanning electron microscopy (Cold FE-SEM S-4800, Hitachi) operating at 10 kV without any metal coating process. The nitrogen adsorption and desorption isotherms were measured with a VELSORP-mini II (BEL Japan, Inc.) at 77 K in the relative pressure range of P/P0 from 0.05 to 0.3. It was fitted to the Brunauer-Emmett-Teller (BET) equation to determine the BET surface areas.

Electrochemical properties of Si foam anodes

The electrochemical properties of Si foam anode were tested by galvanostatic discharging (lithiation) and charging (delithiation) in coin-type half cells (2016 R-type). The cells that are made up of Si foam/poly(acrylic acid) (PAA, Aldrich) and sodium carboxymethyl cellulose (CMC, Aldrich)/acetylene black composites as working electrode, and lithium metal as the

counter electrode, were prepared in a glove box filed argon gas. The electrodes were composed of Si active material (70 wt.%), Super-P (10 wt.%), and a PAA/CMC (50/50, wt./wt.) binder (20 wt.%). The resulting slurry was spread on a copper current collector and dried in a vacuum oven at 150 ^{o}C for 2 h. The electrolyte was composed of 1.3 M $LiPF_6$ in a mixture of ethylene carbonate/diethyl carbonate (Panaxetec, EC/DEC, 30/70 vol.%) with an additive of 10 wt.% fluoroethylene carbonate (FEC). The loading mass of active materials is in the range of 1.2-1.5 mg cm^{-2}. All cells were cycled at a rate of 0.05-0.5 C in the range of 0.005-1.2 V. All the electrochemical measurements were carried out with a WBCS-3000 battery cycler (Wonatech Co.) at room temperature.

4.3 Results and discussion

Conversion of hierarchical SiO_2 foam to Si foam

Porous SiO_2 particles have been synthesized from self-assembled block copolymer template and silica precursors.[33-35] They have attracted much attention in numerous applications, like adsorption, separation, bio-sensing, catalysis, and Si source materials, owing to their unique porous structures.[36-39] In particular, the porous structures with a high surface area make them well suitable for making porous Si particles via a metallothermic reduction process.

In this study, we prepared sponge-like SiO_2 particles with tens-of-nanometer pores and tens-of-micrometer size using triblock copolymer as a structure-directing agent and trimethylbenzene as pore expander. When as-prepared SiO_2 particles were reacted with Mg vapor at 700 ^oC (well above the melting temperature of Mg) for 3h, shape-preserving Si particles were obtained.

Figure 5-1a shows scanning electron microscopy (SEM) image of as-prepared SiO_2 particles. Hundreds-of-nanometer-sized primary SiO_2 particles were aggregated to make micrometer-sized secondary SiO_2 particles (the inset of figure 5-1a). Internal morphology of primary SiO_2 particles was characterized by transmission electron microscopy (TEM). The primary SiO_2 particles showed sponge-like structures consisting of a very thin SiO_2 frame and macro-pores (Figure 5-1d). The nitrogen adsorption isotherm of sponge-like SiO_2 powder is shown in Figure 5-1c. Brunauer-Emmett-Teller (BET) surface area of the SiO_2 particles was 686.17 $m^2 g^{-1}$, indicating a high specific surface area.

During the magnesiothermic reduction reaction, porous Si is formed via the solid-state redox reaction between SiO_2 and Mg, $SiO_2(s) + 2Mg(g) \rightarrow Si(s) + 2MgO(s)$.[39] It is well-known that MgO by-products can be removed easily with a concentrated HCl solution. After the chemical reduction of the SiO_2 particles, SEM image of as-synthesized Si particles shows that primary Si particles are aggregated to make tens-of-micrometer-sized secondary particles (Figure 5-1b). The primary Si particles become bigger compared to original primary SiO_2 particles (Inset of Figure 5-1b). It may be attributed to the aggregation of Si by an exothermic heat that occurs during the magnesiothermic reaction. However, the dimension of secondary Si particles is similar with that of the original SiO_2 particles. TEM image of primary Si particles shows that crystalline Si particles with 10-20 nm feature size are connected each other with a void space and look like Si foam structures (Figure 5-1e). After the magnesiothermic reaction, a void space was significantly decreased. However, void regions uniformly distributed within the primary Si particles would be helpful to accommodate a large volume change of Si anode during lithiation and delithiation process. X-ray diffraction (XRD) patterns of as-synthesized Si

particles indicate that a highly crystalline Si was successfully obtained from chemical reduction of SiO_2 particle (Figure 5-1f).

Prior to electrochemical tests of Si foam particles, we synthesized three different Si particles by changing calcination process of copolymer-containing porous SiO_2 particles. Three samples are no calcination, calcination in ambient air, and calcination in oxygen, respectively. All three samples are sponge-like structures regardless of calcination condition, as shown in TEM images (ESI, Figure S1a-S1c). However, BET surface areas of three SiO_2 particles are totally different due to the residual polymer after calcination (ESI, Figure S1d-S1e). These three SiO_2 particles were converted to Si particles via a magnesiothermic reaction at the same condition. Subsequently, as-synthesized Si particles were carbon-coated with carbon contents of 8 wt.% using thermal decomposition of acetylene gas at 900 ^oC for 10 min, since pristine Si particles exhibit intrinsically low electrical conductivity. Raman spectrum of the carbon-coated Si particles shows two peaks at ~1360 and ~1580 cm^{-1} corresponding to the disordered band (D band) and the graphene band (G band), respectively. The ratio of the D band to the G band was estimated to be 2.21, indicating an amorphous carbon structure.[23] Intense Raman scattering peaks of pristine Si without carbon layers appear at ~520 cm^{-1} indicating crystalline Si structure, as manifested by above XRD patterns (ESI, Figure S2). Furthermore, we characterized surface area and pore volume of three carbon-coated Si foam particles (no calcination-Si (ncSi), air-calcined-Si (acSi), and oxygen-calcined-Si (ocSi)) (ESI, Figure S3 and S4).

Figure 5-2a shows the first cycle galvanostatic discharge (lithiation)-charge (delithiation) curves for three carbon-coated Si foam samples at 0.05 C rate in the range of 0.005-1.2 V. The ncSi shows an initial discharge capacity of 1510 mAh g^{-1} and charge capacity of 740 mAh g^{-1}, corresponding to a very low initial coulombic efficiency of 49%. It may be attributed to the formation of SiC layer that can be produced by additional heat generation during the magnesiothermic reduction.[40,41] Crystalline SiC was formed via chemical reduction of SiO_2 as Si source and copolymer surfactant as carbon source as the following reaction: $SiO_2(s) + C(s) + 2Mg(g) \rightarrow SiC(s) + 2MgO(s)$.[40,41] We confirmed the formation of SiC layers in case of ncSi particles by XRD (ESI, Figure S5). Insulating SiC layers formed at the Si surface act as side reaction in the electrochemical cells as Lipson et al. reported previously.[42] In contrast, acSi and ocSi without SiC layers showed an initial discharge (charge) capacities of 2560 (1820) and 2915 (2290) mAh g^{-1}, respectively, with a significant increase of initial coulombic efficiency. In case of acSi sample, even though there is no detection of carbon in the energy-dispersive X-ray spectroscopy (EDS) characterization after calcination, initial coulombic efficiency of the acSi anode was slightly decreased, compared to the ocSi anode.

However, the cycling performances of three porous Si anodes show the opposite tendency (Figure 5-2b). The ocSi, acSi, and ncSi anodes showed charge capacities of 50, 1500, and 850 mAh g^{-1} after 100 cycles at 0.2 C rate (discharge-charge), respectively, corresponding to the capacity retention of 2%, 96%, and 100%. In particular, excellent cycling performances of the acSi electrodes may be explained as follows: (i) a negligible amount of carbon layers in the porous Si formed during the chemical reduction acts as a buffer layer to a large volume change during the cell operation, (ii) carbon-coated Si foam structure also decrease mechanical stress that occurs during the lithiation and delithiation process.

We further investigated volume expansion of ncSi, acSi, and ocSi electrodes after 1^{st} and 100^{th} cycle lithiation. After cycling, the electrodes were carefully disassembled in a glove box. Subsequently, before and after cycling, the thicknesses of three electrodes were measured by cross-sectional SEM (Figure 5-3). The ncSi, acSi, and ocSi electrodes showed a low volume expansion of 10%, 31%, and 33%, respectively, after 1^{th} cycle lithiation. However, after 100^{th} cycle lithiation, the ncSi, acSi, and ocSi electrodes showed volume expansion of 120%, 175%, and 212%, respectively. From these results, we suggest that residual carbon layers during calcination process of porous SiO_2 particles may affect the cycling retention and the volume expansion of final Si foam electrodes.

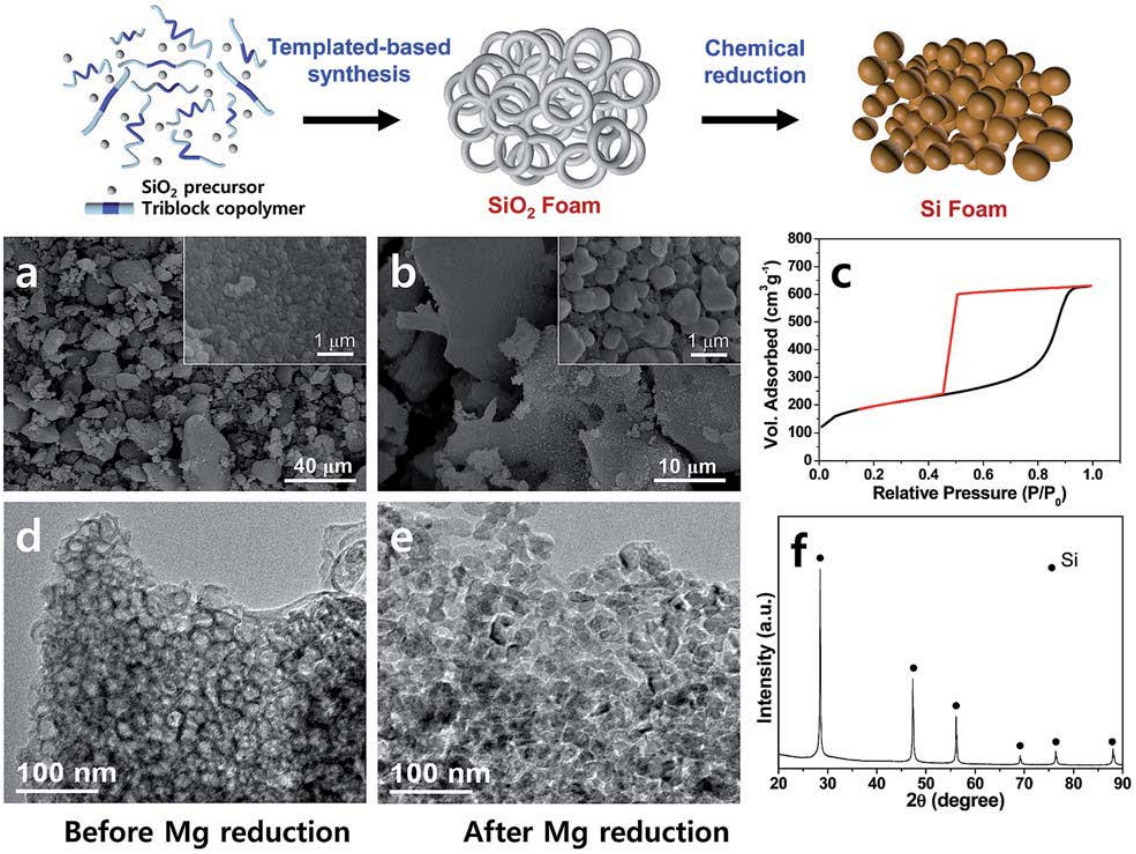

Figure 4-1. Top: schematic illustration showing the synthetic process of SiO2 foam and shape-preserving Si. Bottom: (a) low-magnified SEM image (inset: high-magnified SEM) and (d) TEM image of SiO2 foam prepared by a block copolymer template. (b) Low-magnified SEM image (inset: high-magnified SEM) and (e) TEM image of Si foam prepared by the magnesiothermic reaction of SiO2. (c) BET plot of the SiO2 foam shows a typical mesoporous structure. (f) XRD pattern of as-synthesized Si foam clearly shows the crystalline structure.

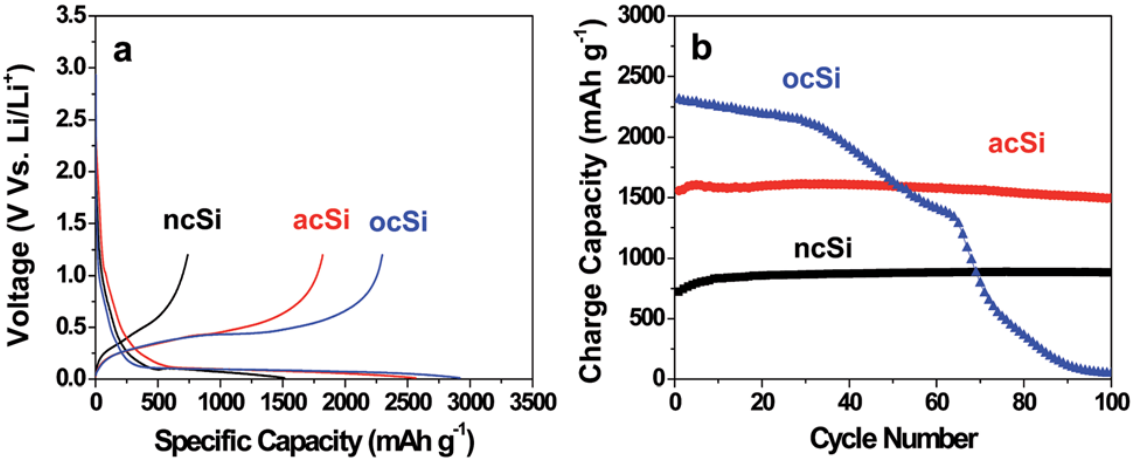

Figure 4-2. Electrochemical tests of carbon-coated Si foam particles (ncSi, acSi, and ocSi) prepared by three different calcination processes. (a) First cycle voltage profiles of three samples obtained at 0.05 C rate between 0.005 and 1.2 V. (b) Cycle performances of three Si foam electrodes at 0.2 C (discharge–charge) rate were tested to 100 cycles.

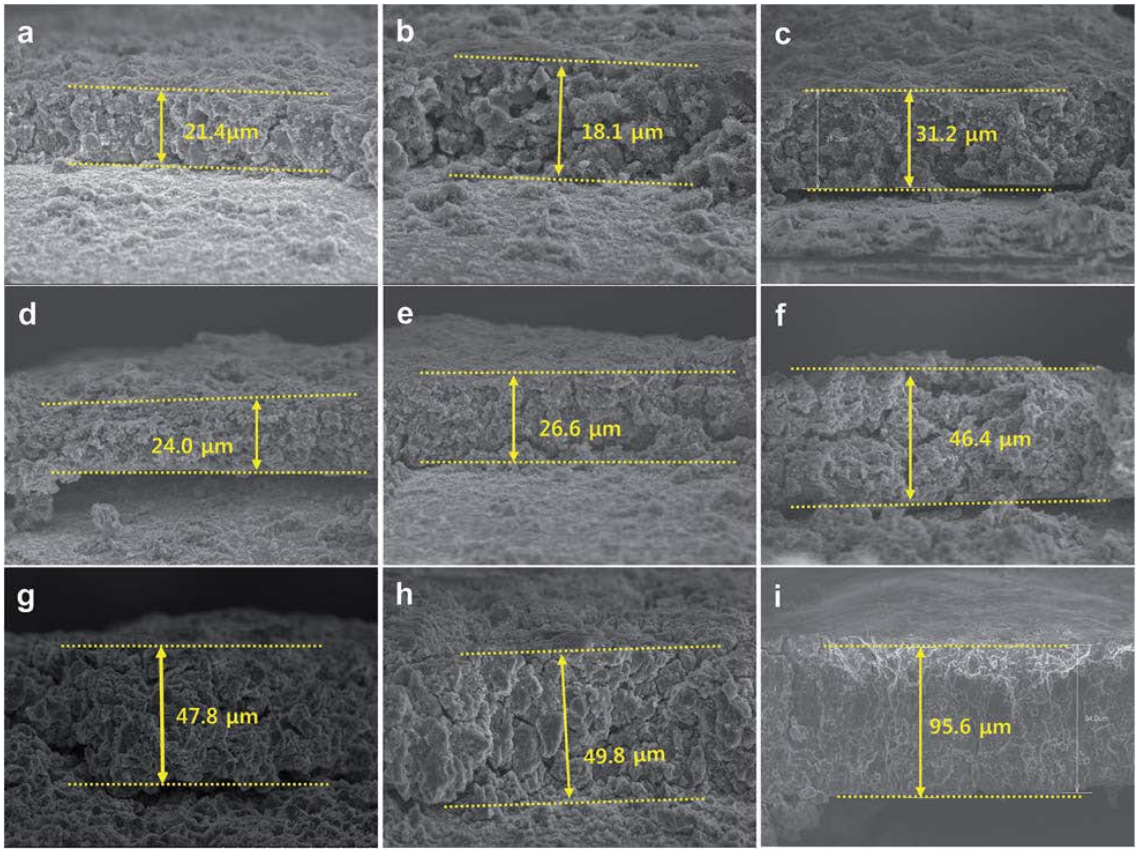

Figure 4-3. Cross-sectional SEM images showing the volume expansion of three Si electrodes (a–c: as-prepared, d–f: after 1st cycle lithiation, and g–i: after 100th cycle lithiation). Electrode thicknesses of ncSi (a: before, d: 1st cycle, and g: 100th cycle), acSi (b: before, e: 1st cycle, and f: 100th cycle), and ocSi (c: before, f: 1st cycle, and i: 100th cycle). The ncSi, acSi, and ocSi electrodes showed a volume expansion of 120%, 175%, and 212%, respectively, after 100 cycles.

Effect of heat scavenger on the morphology of Si particles

In general, magnesiothermic reduction reaction between Mg and SiO_2 generates massive heat, resulting in collapses the architecture of SiO_2 particles and agglomeration of as-synthesized Si particles. Won et al. reported that the exothermic temperature measured in the magnesiothermic reduction could reach a very high temperature, 1720 ^oC.[43] When the magnesiothermic reaction was carried out in solid phase diluted with alkali metal halides (e.g., NaCl, $MgCl_2$, $CaCl_2$, etc.), molten salts can consume the generated heat.[44, 45]

We employed NaCl as a heat scavenger to retain the original SiO_2 foam structure after the chemical reduction. The oxygen-calcined SiO_2/NaCl mixture and Mg powder (SiO_2:Mg:NaCl = 1:0.8:1 in mass) were homogeneously mixed together in an argon-filled glovebox. Subsequently, the mixture was heated in a tube furnace at 700 ^oC for 3 h under argon environment. After the reaction, NaCl salt was washed several times by water and MgO by-products salts were completely removed from 1M HCl. Figure 4a and 4b show TEM images of Si particles synthesized without and with NaCl salts, respectively. As expected, Si particles with void spaces were obtained in the presence of NaCl, while Si obtained in the absence of NaCl was seriously agglomerated. After both Si particles were coated with carbon contents of 8 wt.%, they were cycled at 0.2 C rate (discharge-charge) between 0.005 and 1.2 V. Porous Si electrodes (with NaCl) exhibited a high reversible capacity of 2350 mAh g^{-1} after 100 cycles, corresponding to the capacity retention of 87.4% compared to initial capacity. In contrast, Si electrodes (without NaCl) showed a significant capacity decaying (capacity retention of 2.5% after 100 cycles). Similarly, volume expansion of porous Si electrodes (with NaCl) was significantly decreased after 100 cycles, compared to the Si electrodes (without NaCl) (ESI, Figure S6). These results suggested that magnesiothermic reduction in the presence of molten salts reduces exothermic heat, resulting in preservation of original SiO_2 structure and a significant improvement of electrochemical properties of Si electrodes.

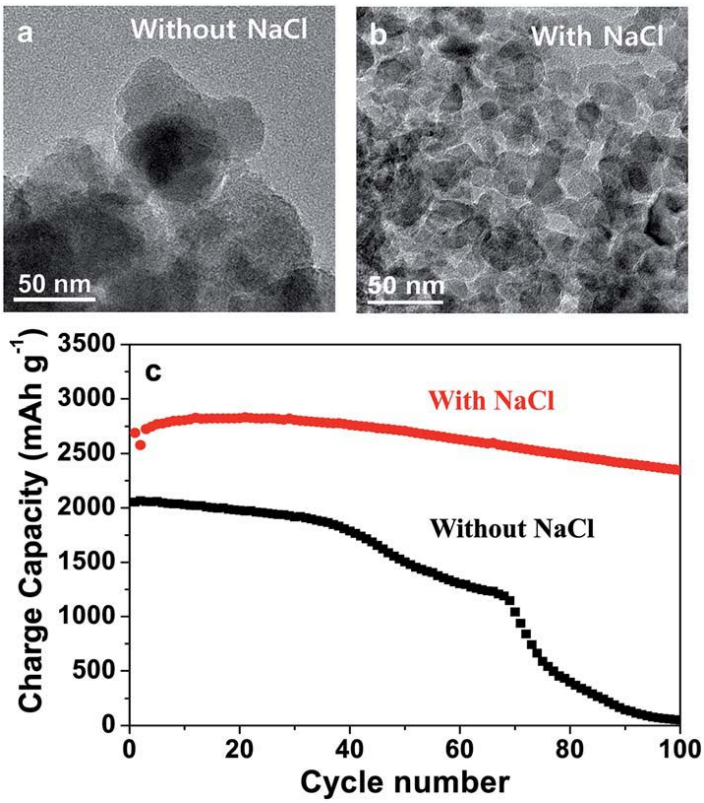

Figure 4-4. TEM images of Si foam obtained by the magnesiothermic reaction (a) without NaCl and (b) with NaCl. (c) Cycle performances of Si foam electrodes with NaCl (red, solid dot) and without NaCl (black, solid square) were tested at 0.2 C (discharge–charge) until 100 cycles.

Synthesis of metal-loaded Si foam

Another effective strategy to improve electrochemical properties of Si foam anode is to introduce metal nanoparticles within Si foam, since one of the critical problems related to Si-based particles is their low intrinsic electrical conductivity. We employed well-known silver (Ag) mirror reaction to coat Ag nanoparticles on the surface of oxygen-calcined SiO_2 foam particles.[46] A one-pot chemical reduction of Ag precursor in the presence of n-butylamine led to a formation of Ag-loaded SiO_2 foam particles at room temperature. Typically, 0.25 g of oxygen-calcined SiO_2 foam particles was dispersed into 20 mL of ethanol at 35 ^oC in a propylene vessel, and subsequently, 50 mM of AgNO3 and 50 mM of n-butylamine were simultaneously added to the solution and kept stirring for 10 min.

Figure 5-5a clearly shows that Ag nanoparticles with diameters of 5-10 nm were uniformly distributed into SiO_2 foam particles without a serious aggregation. Subsequent magnesiothermic reduction of Ag-loaded SiO_2 and Mg vapor led to a successful formation of Ag-doped Si particles. During the chemical reduction process, a significant aggregation of Ag nanoparticles within Si foam was seen due to the exothermic heat. However, the bigger Ag particles were still dispersed well into the Si foam particles (Figure 5-5b). XRD patterns of the Ag-loaded Si particles indicate that crystalline Ag and Si particles are clearly detected (Figure 5-5c). Moreover, Ag contents of 2 wt.% were confirmed through the EDS analysis. The Ag-doped Si foam electrodes were tested by galvanostatic discharging and charging at a rate of 0.05-0.2 C in the range of 0.005-1.2 V. The first discharge and charge capacities are 2580 and 2085 mAh g^{-1}, respectively, corresponding to the initial coulombic efficiency of 80.8% (Figure 5-5d). The increasing coulombic efficiency is attributed to the enhancement of electrical conductivity owing to the Ag doping. Subsequent cycling performances were tested at 0.2 C (discharge-charge) rate. After 50 cycles, a high reversible capacity of 1220 mAh g^{-1} was exhibited with a high coulombic efficiency per cycle (>99.5% after 5 cycles). To further investigate the superior electrochemical property of the Ag-doped Si electrodes, electrochemical impedance spectroscopy (EIS) was conducted. The Nyquist impedance plots are obtained after 50th cycle for Ag-doped ncSi and ncSi sample (ESI, Figure S7). The charge-transfer resistance (R_{ct} = 5.71 ohm) of the Ag-doped ncSi electrode is smaller than those of ncSi electrode (R_{ct} = 57.92 ohm) at a rate of 0.2 C. This result indicates that the Ag-doped ncSi electrode is more suitable for the Li^+ diffusion.

Moreover, we extended this idea to Cu-doped Si foam particles. Cu-doped Si foam particles were successfully synthesized and their electrochemical performances including a high reversible capacity (2000 mAh g^{-1} at 0.05 C rate) and a good capacity retention (84.2% after 50 cycles at 0.2 C rate) were exhibited (ESI, Figure S8).

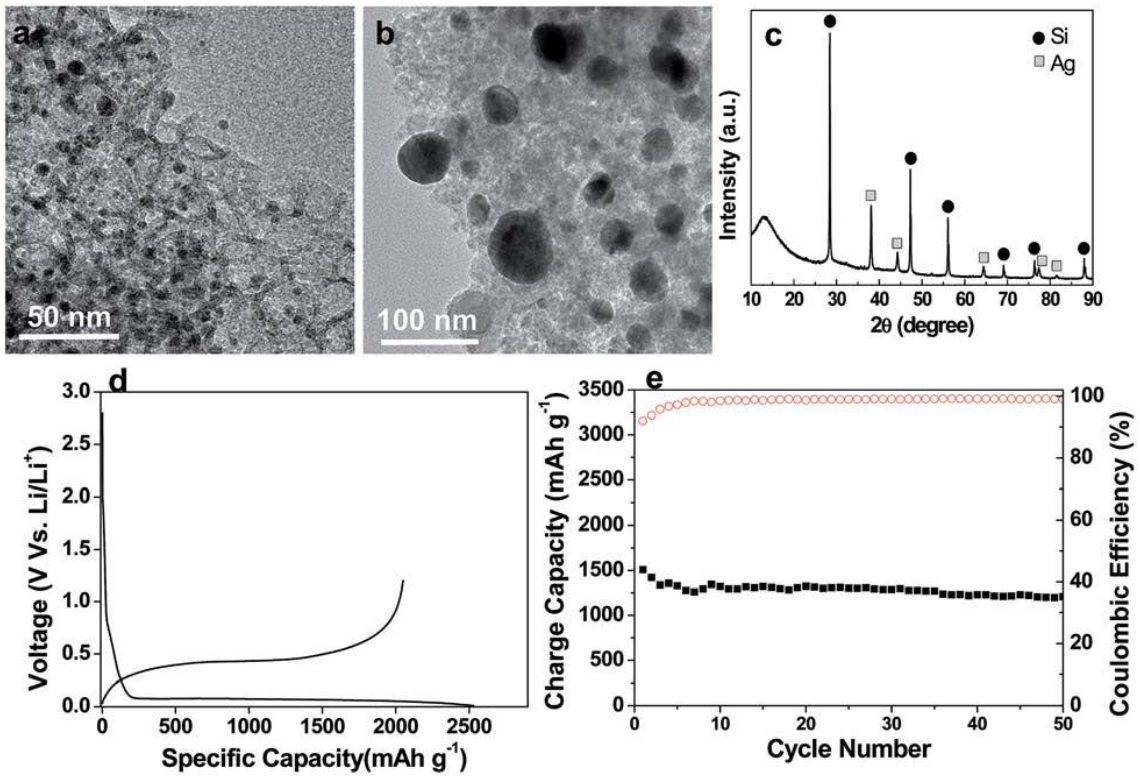

Figure 4-5. TEM images of (a) Ag-loaded SiO2 foam and (b) Ag-doped Si particles. (c) XRD patterns of the Ag-doped Si particles show that Ag and Si are crystalline structures. (d) First cycle voltage profile of the Ag-doped Si anode was obtained at 0.05 C rate between 0.005 and 1.2 V. (e) Cycling retention of the Ag-doped Si was obtained at 0.2 C rate (discharge–charge) until 50 cycles.

4.4 Conclusion

We demonstrated three effective strategies for enhancing the electrochemical performances of highly porous Si anode prepared by a magnesiothermic reduction reaction. The first strategy was a conversion of hierarchical SiO_2 to Si with preserving the original SiO_2 porous structure. By controlling calcination process, amount of residual carbon sources in as-prepared porous SiO_2 was controlled by tuning the calcination process. Subsequent Si particles obtained by magnesiothermic reaction showed different electrochemical performances. The second way was to introduce heat scavenging molten salt during magnesiothermic reduction to minimize exothermic heat. It led to a successful synthesis of shape-preserving Si foam particles after the chemical reduction, resulting in a significant improvement of cycling retention. The third strategy is to introduce metal nanoparticles within Si foam particles during the chemical reduction reaction. Electrically conductive Ag and Cu nanoparticles were uniformly dispersed in Si foam, leading to the significant improvements of initial coulombic efficiency and cycle retention of metal-doped Si anodes. These strategies can be extended not only Si particles but also other particles for improving electrochemical performances for practical rechargeable battery applications.

4.5 Reference

1. Nazri, G.-A.; Pistoia, G., *Lithium batteries: science and technology*. Springer Science & Business Media: 2008.
2. Whittingham, M. S., Materials challenges facing electrical energy storage. *Mrs Bulletin* **2008,** *33* (4), 411-419.
3. Armand, M.; Tarascon, J.-M., Building better batteries. *Nature* **2008,** *451* (7179), 652-657.
4. Liu, C.; Li, F.; Ma, L. P.; Cheng, H. M., Advanced materials for energy storage. *Advanced materials* **2010,** *22* (8).
5. Song, M.-K.; Park, S.; Alamgir, F. M.; Cho, J.; Liu, M., Nanostructured electrodes for lithium-ion and lithium-air batteries: the latest developments, challenges, and perspectives. *Materials Science and Engineering: R: Reports* **2011,** *72* (11), 203-252.
6. Szczech, J. R.; Jin, S., Nanostructured silicon for high capacity lithium battery anodes. *Energy Environ. Sci.* **2011,** *4* (1), 56-72.
7. Obrovac, M. N.; Christensen, L., Structural Changes in Silicon Anodes during Lithium Insertion/Extraction. *Electrochemical and Solid-State Letters* **2004,** *7* (5), A93.
8. Hossain, S.; Kim, Y.-K.; Saleh, Y.; Loutfy, R., Comparative studies of MCMB and C□ C composite as anodes for lithium-ion battery systems. *Journal of power sources* **2003,** *114* (2), 264-276.
9. B. A. Boukamp, G. C. L., R. A. Huggins, All-Solid Lithium Electrodes with Mixed-Conductor Matrix. *Journal of Electrochemical Society: ELECTROCHEMICAL SCIENCE AND TECHNOLOGY* **1981,** *128* (4), 725-728.
10. Kasavajjula, U.; Wang, C.; Appleby, A. J., Nano-and bulk-silicon-based insertion anodes for lithium-ion secondary cells. *Journal of Power Sources* **2007,** *163* (2), 1003-1039.
11. Kulova, T.; Pleskov, Y. V.; Skundin, A.; Terukov, E.; Kon'Kov, O., Lithium intercalation into amorphous-silicon thin films: An electrochemical-impedance study. *Russian Journal of Electrochemistry* **2006,** *42* (7), 708-714.
12. Chen, S.; Gordin, M. L.; Yi, R.; Howlett, G.; Sohn, H.; Wang, D., Silicon core–hollow carbon shell nanocomposites with tunable buffer voids for high capacity anodes of lithium-ion batteries. *Physical Chemistry Chemical Physics* **2012,** *14* (37), 12741-12745.
13. Cho, J., Porous Si anode materials for lithium rechargeable batteries. *Journal of Materials Chemistry* **2010,** *20* (20), 4009-4014.
14. Gohier, A.; Laïk, B.; Kim, K. H.; Maurice, J. L.; Pereira-Ramos, J. P.; Cojocaru, C. S.; Van, P. T., High-Rate Capability Silicon Decorated Vertically Aligned Carbon Nanotubes for Li-Ion Batteries. *Advanced materials* **2012,** *24* (19), 2592-2597.

15. Zhou, X.; Yin, Y.-X.; Wan, L.-J.; Guo, Y.-G., Facile synthesis of silicon nanoparticles inserted into graphene sheets as improved anode materials for lithium-ion batteries. *Chemical communications* **2012,** *48* (16), 2198-2200.
16. Jia, H.; Gao, P.; Yang, J.; Wang, J.; Nuli, Y.; Yang, Z., Novel Three-Dimensional Mesoporous Silicon for High Power Lithium-Ion Battery Anode Material. *Advanced Energy Materials* **2011,** *1* (6), 1036-1039.
17. Du, F.-H.; Wang, K.-X.; Fu, W.; Gao, P.-F.; Wang, J.-F.; Yang, J.; Chen, J.-S., A graphene-wrapped silver–porous silicon composite with enhanced electrochemical performance for lithium-ion batteries. *Journal of Materials Chemistry A* **2013,** *1* (43), 13648-13654.
18. Chan, C. K.; Peng, H.; Liu, G.; Mcilwrath, K.; Zhang, X. F.; Huggins, R. A.; Cui, Y., High-performance lithium battery anodes using silicon nanowires. *Nature nanotechnology* **2008,** *3* (1), 31.
19. Mukherjee, R.; Krishnan, R.; Lu, T.-M.; Koratkar, N., Nanostructured electrodes for high-power lithium ion batteries. *Nano Energy* **2012,** *1* (4), 518-533.
20. Yi, R.; Dai, F.; Gordin, M. L.; Chen, S.; Wang, D., Micro-sized Si-C Composite with Interconnected Nanoscale Building Blocks as High-Performance Anodes for Practical Application in Lithium-Ion Batteries. *Advanced Energy Materials* **2013,** *3* (3), 295-300.
21. Bruce, P. G.; Scrosati, B.; Tarascon, J. M., Nanomaterials for rechargeable lithium batteries. *Angewandte Chemie International Edition* **2008,** *47* (16), 2930-2946.
22. Manthiram, A.; Murugan, A. V.; Sarkar, A.; Muraliganth, T., Nanostructured electrode materials for electrochemical energy storage and conversion. *Energy & Environmental Science* **2008,** *1* (6), 621-638.
23. Bang, B. M.; Kim, H.; Song, H.-K.; Cho, J.; Park, S., Scalable approach to multi-dimensional bulk Si anodes via metal-assisted chemical etching. *Energy & Environmental Science* **2011,** *4* (12), 5013-5019.
24. Magasinski, A.; Dixon, P.; Hertzberg, B.; Kvit, A.; Ayala, J.; Yushin, G., High-performance lithium-ion anodes using a hierarchical bottom-up approach. *Nature materials* **2010,** *9* (4), 353-8.
25. Bang, B. M.; Lee, J. I.; Kim, H.; Cho, J.; Park, S., High-Performance Macroporous Bulk Silicon Anodes Synthesized by Template-Free Chemical Etching. *Advanced Energy Materials* **2012,** *2* (7), 878-883.
26. Kim, H.; Han, B.; Choo, J.; Cho, J., Three-dimensional porous silicon particles for use in high-performance lithium secondary batteries. *Angewandte Chemie* **2008,** *120* (52), 10305-10308.
27. Yoo, S.; Lee, J. I.; Shin, M.; Park, S., Large-Scale Synthesis of Interconnected Si/SiOx Nanowire Anodes for Rechargeable Lithium-Ion Batteries. *ChemSusChem* **2013,** *6* (7), 1153-

1157.

28. Yu, Y.; Gu, L.; Zhu, C.; Tsukimoto, S.; van Aken, P. A.; Maier, J., Reversible Storage of Lithium in Silver-Coated Three-Dimensional Macroporous Silicon. *Advanced materials* **2010,** *22* (20), 2247-2250.
29. Lee, J. I.; Lee, K. T.; Cho, J.; Kim, J.; Choi, N. S.; Park, S., Chemical-assisted thermal disproportionation of porous silicon monoxide into silicon-based multicomponent systems. *Angewandte Chemie International Edition* **2012,** *51* (11), 2767-2771.
30. Chen, D.; Mei, X.; Ji, G.; Lu, M.; Xie, J.; Lu, J.; Lee, J. Y., Reversible Lithium-Ion Storage in Silver-Treated Nanoscale Hollow Porous Silicon Particles. *Angewandte Chemie International Edition* **2012,** *51* (10), 2409-2413.
31. Kim, H.; Jung, J. C.; Kim, P.; Yeom, S. H.; Lee, K.-Y.; Song, I. K., Preparation of H 3 PMo 12 O 40 catalyst immobilized on surface modified mesostructured cellular foam (SM-MCF) silica and its application to the ethanol conversion reaction. *Journal of Molecular Catalysis A: Chemical* **2006,** *259* (1), 150-155.
32. Zhao, D.; Feng, J.; Huo, Q.; Melosh, N.; Fredrickson, G. H.; Chmelka, B. F.; Stucky, G. D., Triblock copolymer syntheses of mesoporous silica with periodic 50 to 300 angstrom pores. *science* **1998,** *279* (5350), 548-552.
33. Minakuchi, H.; Nakanishi, K.; Soga, N.; Ishizuka, N.; Tanaka, N., Octadecylsilylated porous silica rods as separation media for reversed-phase liquid chromatography. *Analytical chemistry* **1996,** *68* (19), 3498-3501.
34. Lee, J.; Kim, J.; Kim, J.; Jia, H.; Kim, M. I.; Kwak, J. H.; Jin, S.; Dohnalkova, A.; Park, H. G.; Chang, H. N., Simple synthesis of hierarchically ordered mesocellular mesoporous silica materials hosting crosslinked enzyme aggregates. *Small* **2005,** *1* (7), 744-753.
35. Davis, M. E., Ordered porous materials for emerging applications. *Nature* **2002,** *417* (6891), 813-821.
36. Hoffmann, F.; Cornelius, M.; Morell, J.; Fröba, M., Silica-based mesoporous organic–inorganic hybrid materials. *Angewandte Chemie International Edition* **2006,** *45* (20), 3216-3251.
37. Slowing, I. I.; Trewyn, B. G.; Giri, S.; Lin, V. Y., Mesoporous silica nanoparticles for drug delivery and biosensing applications. *Advanced Functional Materials* **2007,** *17* (8), 1225-1236.
38. Bao, Z.; Weatherspoon, M. R.; Shian, S.; Cai, Y.; Graham, P. D.; Allan, S. M.; Ahmad, G.; Dickerson, M. B.; Church, B. C.; Kang, Z., Chemical reduction of three-dimensional silica micro-assemblies into microporous silicon replicas. *Nature* **2007,** *446* (7132), 172-175.
39. Shi, Y.; Zhang, F.; Hu, Y.-S.; Sun, X.; Zhang, Y.; Lee, H. I.; Chen, L.; Stucky, G. D., Low-temperature pseudomorphic transformation of ordered hierarchical macro-mesoporous

SiO2/C nanocomposite to SiC via magnesiothermic reduction. *Journal of the American Chemical Society* **2010,** *132* (16), 5552-5553.

40. Choi, S.; Lee, J. C.; Park, O.; Chun, M.-J.; Choi, N.-S.; Park, S., Synthesis of micro-assembled Si/titanium silicide nanotube anodes for high-performance lithium-ion batteries. *Journal of Materials Chemistry A* **2013,** *1* (36), 10617.
41. Lipson, A. L.; Chattopadhyay, S.; Karmel, H. J.; Fister, T. T.; Emery, J. D.; Dravid, V. P.; Thackeray, M. M.; Fenter, P. A.; Bedzyk, M. J.; Hersam, M. C., Enhanced lithiation of doped 6H silicon carbide (0001) via high temperature vacuum growth of epitaxial graphene. *The Journal of Physical Chemistry C* **2012,** *116* (39), 20949-20957.
42. Won, C.; Nersisyan, H.; Won, H., Solar-grade silicon powder prepared by combining combustion synthesis with hydrometallurgy. *Solar Energy Materials and Solar Cells* **2011,** *95* (2), 745-750.
43. Won, C.; Nersisyan, H.; Won, H.; Lee, J., Refractory metal nanopowders: synthesis and characterization. *Current Opinion in Solid State and Materials Science* **2010,** *14* (3), 53-68.
44. Luo, W.; Wang, X.; Meyers, C.; Wannenmacher, N.; Sirisaksoontorn, W.; Lerner, M. M.; Ji, X., Efficient fabrication of nanoporous Si and Si/Ge enabled by a heat scavenger in magnesiothermic reactions. *Scientific reports* **2013,** *3*.
45. Yoo, S.; Lee, J.-I.; Ko, S.; Park, S., Highly dispersive and electrically conductive silver-coated Si anodes synthesized via a simple chemical reduction process. *Nano Energy* **2013,** *2* (6), 1271-1278.

Chapter V. Mesoporous Silicon Hollow Nanocubes Derived from Metal−Organic Framework Template for Advanced Lithium-Ion Battery Anode

5.1 Introduction

To satisfy the ever-growing demand for technological applications including electric vehicles and renewable power stations, intensive academic and industrial efforts have been devoted to developing clean, renewable, and sustainable energy solutions.[1,2] Among various approaches to develop energy solutions, rechargeable lithium-ion batteries (LIBs) are one of the most important energy storage devices because of their impressive energy density, long cycling stability, discharge–charge rate capability, and low cost.[3-5] In particular, Si-based anodes have been considered promising candidates because of their abundant natural resources and electrochemical properties, such as their low Li-uptake voltage (~0.5 V vs. Li/Li^+) and exceptionally higher theoretical capacity (3579 $mAhg^{-1}$ in the form of $Li_{15}Si_4$) than commercial graphite (372 $mAhg^{-1}$ in the form of LiC_6).[6,7] However, the full utilization of Si-based anodes is limited by the low diffusivity for Li ions, low intrinsic electronic conductivity, and poor structural stability caused by their dramatic volume change (>300%) during lithiation–delithiation.[8] As a result, micrometer-size Si anodes exhibit serious capacity fading.[1,9-11] Hence, nanostructuring strategies for Si have attracted considerable attention to improve the structural stability and electrochemical performance of Si-based anode materials. Recently, there have been important findings related to nanostructured Si materials such as Si nanowires,[4,11] nanotubes,[9,12] nanosheets,[13,14] and hollow[15-17] and porous structures.[18-20]

The metal-organic frameworks (MOFs), constructed by bridging metal ions with organic linkers to form three-dimensional (3D) crystalline networks, are a key to synthesizing 3D hollow morphologies with complex configurations.[21,22] Recently, the application of MOFs in LIBs has been reported to improve the performances of anode materials by relaxing the volume expansion of active Si.[23-25] Nevertheless, the control of morphology and porosity for MOF template-based materials is still underdeveloped. As a simple process, the use of removable or sacrificial templates is an effective route to form hollow-type morphologies.[26,27] Such a design offers attractive features to synthesize the resulting materials. First, the MOFs with metal ion and organic linkers are coordinately saturated, which is caused by uniform distribution as individual templates

with controllable size and morphology.[21] Second, the MOF templated core-shell composites generate a hollow nanostructure after the etching of MOFs. More importantly, the designated crystallographic planes of MOFs can control the deposition of ionic or molecular species without altering the initial shape.[28] Among the classic examples of MOFs, the zeolitic imidazolate framework with coordination bonding of metal-nitrogen (*i.e.*, ZIF-8) is employed as an ideal template because of its exceptional chemical and thermal stability.[29] In addition, the exterior surface of ZIF-8 is hydrophilic due to N−H functional groups, which uniformly adhere to the precursor on the ZIF-8 surface and generate hydrolyzed oligomers as solution-based chemical reaction.[30]

Herein, we demonstrate the synthesis of m-Si HCs *via* magnesiothermic reduction reaction (MRR) of silica-coated ZIF-8. The MRR is a facile route for preparing porous Si structures along with MgO by-products.[31] In this system, silica-coated ZIF-8 is converted into mesoporous silicon-coated ZnO/MgO during the MRR. Subsequently, the by-products are removed by acid treatment. The MOF is used as a sacrificial template to create inner void spaces in the final product. The resulting m-Si HCs have several advantages: i) the architecture with the mesoporous external shell and internal void (~60 nm) can effectively accommodate a large volume expansion,[15,32] ii) the thin Si shell (thickness of ~15 nm) can significantly reduce the electronic and ionic diffusion pathways between electrolytes and Li ions,[15] iii) the high porosity of Si shell can facilitate the electrolyte penetration during electrochemical test,[33] iv) the cube-shaped architecture enhances the m-Si HC/electrolyte contact area because of the accessible exposed active plane,[34] which enhances the diffusion efficiency.

5.2 Experimental

Materials

Zinc nitrate hexahydrate (≥99%), 2-Methylimidazole (HMIM, 99%) and silicon dioxide nanopowder (10-20 nm, 99.5%) were purchased from Sigma-Aldrich. (1-Hexadecyl)trimethylammonium bromide (CTAB, 98%) and Tetraethyl orthosilicate (98%) were purchased from Alfa Aesar. All the chemicals were of analytical grade and used without further purification.

Synthesis of ZIF-8 NC

0.72 g of $Zn(NO_3)_2 \cdot 6H_2O$ was dispersed in 72.0 mL of deionized water, followed by adding 1.20 mL of 0.10 M CTAB aqueous solution. After stirring for 10 min at room temperature, 120.0 mL of 1.096 M HMIM solution was added and stirred for another 10 min. Then, the mixture was transferred to 300 mL Teflon-line autoclave and heated in an electric oven at 120 °C for 6 h. Finally, the precipitate was centrifuged at 8000 rpm for 10 min and washed with methanol three times, and dried at 80 °C overnight.

Synthesis of ZIF-8@SiO_2

ZIF-8 NC can be used as template for SiO_2 shell coating. 1.0 g of the as-prepared ZIF-8 NC was dispersed in a solution containing 400 mL of ethanol, 660 mL of deionized water and 5 g of HMIM. The solution was then sonicated for 30 min, followed by adding 3.04 g of CTAB and stirred for another 30 min. Then, 8 mL of TEOS was added into this solution dropwise within 3 min. The solution was vigorously stirred for 2 h. Finally, the precipitate was centrifuged at 8000 rpm for 10 min and washed with methanol three times, and dried at 80 °C overnight. The 5 nm ZIF-8@SiO_2 was synthesized by adding 4 mL of TEOS and then stirring for 1 h. The 50 nm ZIF-8@SiO_2 was synthesized by adding 16 mL of TEOS and then stirring for 4 h.

Synthesis of ZnO@SiO_2 HC

ZIF-8@SiO_2 sample was heated at 600 °C for 6 h with a ramping rate of 5 °C/min by flowing the air atmosphere.

Synthesis of Si HC, m-Si HC and reference Si

Different weight ratios between sample and magnesium are used for Mg reduction; Si HC, m-Si HC and reference Si (Si nanoparticles, 10–20 nm in diameter) were heated at 650 °C for 3 h under argon atmosphere with different weight of Mg (weight ratios of Mg to sample = 0.4:1, 0.8:1

and 0.8:1, respectively). Then, these samples were leached with 1.0 M HCl for 1h to remove the MgO, followed by washing with ethanol and DI water, and drying at 80 °C overnight. The reference Si showed mesoporous structure after MRR. Finally, carbon coating was carried out with high purity acetylene (C_2H_2) gas at a flow rate of 500 mL/min for 5 min at 900 °C.

Characterization

The surface morphologies were analyzed by field-emission scanning electron microscopy (FE-SEM, Nova 230, FEI). The morphological investigations were carried out with high resolution transmission electron microscopy (HRTEM) and scanning transmission electron microscopy (STEM) with an acceleration voltage of 200 kV, and EDX scan was used to characterize the elements of samples (JEM-2100F, JEOL). The crystallographic information was determined through high-power X-ray diffractometer (MAX 2500V, Rigaku, Cu Kα radiation λ = 1.54059 Å) with scanning angle 2θ ranging from 10° to 80°. Surface analysis of samples were investigated by X-ray photoelectron spectroscopy (K-alpha, ThermoFisher) with a beam of monochromated aluminum X-ray source. Surface areas of samples were determined using N_2 adsorption-desorption isotherms at 77 K (ASAP 2020, Micromeritics Instrument) with Brunauer-Emmett-Teller (BET) method. Prior to the BET measurements, the samples were degassed at 100 °C for overnight in vacuum. Raman spectroscopy was carried out on a Confocal Raman (alpha 300R, WITec) with a laser wavelength of 532 nm. The chemical compositions were determined by ICP-MS (Perkin Elmer, ELAN DRC-II) and EA (Flash 2000, ThermoFisher)

Electrochemical test

The galvanostatic measurement of all samples were tested using a 2032-coin cell. Lithium metal was used as counter and reference electrode, while working electrode was composed of 70 wt.% of active materials, 15 wt.% of Poly(acrylic acid)/sodium carboxymethyl cellulose (CMC) (1/1 in weight) and 15 wt.% of super-P, representing 1.0 mg cm^{-2} of loading density. The electrochemical performances for electrodes at various loading levels are shown in Figure S23. For the full cell test, anode was prepared with natural graphite/m-Si HC (90:10 in weight fraction) and consisted of active material, styrene butadiene rubber/CMC, super-P at the weight ratio of 95.8:1.7:1.5:1, while cathode (areal density = 2.9 mA h cm^{-2}) was prepared with commercialized $LiCoO_2$ (92wt.%), polyvinylidene fluoride binder (3 wt.%) and super-P (5 wt.%). N/P ratio of ~1.1 was designed. The mixed slurry was coated on copper current collector for anode and aluminum current collector for cathode, dried at 80 °C for 20 min, and further dried in vacuum at 150 °C for 2 h. 1.3 M $LiPF_6$ in ethylene carbonate and diethyl carbonate (EC/DEC, 3/7, in volume) with 10 wt.% of fluoroethylene carbonate (FEC) was used as liquid electrolyte. 20-μm-thick polyethylene separator was employed. Every coin cell was tested using a WBCS-3000 battery

cycler at room temperature. The operation voltage is between 0.005 to 1.5 V for the first cycle at a 0.05 C-rate and between 0.01 to 1.2 V for the rest in half cell, while full cell analysis was carried out in the voltage windows from 2.5 to 4.2 V. Electrochemical impedance spectroscopy (EIS) was carried out in the range of 100 kHz to 0.1 Hz with an amplitude of 10 mV using an Iviumstat (Ivium Technologies).

5.3 Results and discussion

The major synthetic routes to prepare the m-Si HC material are presented in Figures 6-1a and S1. First, ZIF-8 nanocubes (denoted as ZIF-8 NC, with an average diameter of ~60 nm) have 6 (100) facets through the coordinate bonding between metal ions and imidazole molecules (N–M–N, where M is Zn^{2+}, Co^{2+}, *etc.* and N is a nitrogen atom), as shown in Figure 6-1b.[35] The SiO_2 shell is directly coated on the surface of ZIF-8 NC (denoted as ZIF-8@SiO_2 with the thickness of the SiO_2 shell being ~15 nm) by hydrolyzing tetraethyl orthosilicate (TEOS) as a Si precursor under an alkaline solution containing water, ethanol, and imidazole molecules (Figure 6-1c). The pH values of 10.2 should be attained to maintain the ZIF-8 NC structure and form the silica shell.[36] Subsequently, ZIF-8@SiO_2 is treated by pyrolysis to remove the remaining surfactants and organic species of TEOS, during which ZnO is formed inside the silica shell under air condition. Note that the architecture of armored ZnO can be efficiently protected during thermal and chemical treatments (Figure 6-1d, denoted as ZnO@SiO_2 HC). The SiO_2 shell in the ZnO@SiO_2 HC is converted to metallic Si *via* the MRR at 650°C in an inert atmosphere.[37] However, different weight ratios between the sample and magnesium are considered for MRR:ZnO@SiO_2 HC and Mg with weight ratios of 1:0.4 and 1:0.8. As a result, the Si hollow nanocubes (Figure 6-1e, denoted as Si HCs) after MRR with a weight ratio of 1:0.4 are well preserved because of the limited reaction with less heat generation, which results in the formation of unreacted silica and magnesium silicate (Mg_xSiO_y).[38] In addition, the mesoporous Si hollow nanocubes (Figure 6-1f, denoted as m-Si HCs) after Mg reduction with a weight ratio of 1:0.8 generate mesoporous Si because of the relatively complete conversion. The compositional line profiles of all the samples were obtained using transmission electron microscopy (TEM) coupled with energy-dispersive X-ray spectroscopy (Figure S2). The additional information for Si HC and m-Si HC morphologies towards high-resolution transmission electron microscopy (HRTEM), scanning transmission electron microscopy (STEM), energy-dispersive X-ray spectroscopy (EDX), and fast Fourier transform (FFT) are shown in Figure S3-S7 with more detailed information.

To further characterize the crystallographic information of the ZIF-8 NC, ZIF-8@SiO_2, ZnO@SiO_2 HC, Si HC, and m-Si HC samples, X-ray diffraction (XRD) patterns were obtained (Figure 6-2a). The XRD patterns for ZIF-8 NC are in good agreement with previous reports.[35,36] The ZIF-8@SiO_2 patterns show no obvious change because of the amorphous characteristic of SiO_2. After annealing the ZIF-8@SiO_2, all the peaks of ZIF-8 NC disappeared, whereas broad peaks attributed to amorphous SiO_2 and ZnO were formed (labeled ♠, JCPDS #36-1451). It can be concluded that the carbon species of ZIF-8 NC after heat treatment under air condition were

degraded and the Zn ions were transformed to ZnO inside the SiO_2 shell. The main diffraction peaks of the Si HC and m-Si HC samples at 28.4°, 47.3°, 56.1°, 69.1°, and 76.3° are attributed to the (111), (220), (311), (400), and (331) lattice planes of crystalline Si, respectively (labeled ♦, JCPDS #05-0565). However, the extra peaks for the Si HC sample are indicative of the formation of Mg_xSiO_y, resulting from the incomplete reduction (labeled ♣, JCPDS #34-0189). To clarify the differences in the binding characteristics of Si HC and m-Si HC, X-ray photoelectron spectroscopy (XPS) was employed. The peaks of Zn 2p and C 1s in Figures S3 and S4 almost disappeared after thermal and chemical treatments. The binding energies at Si 2p were deconvoluted into individual peaks at 95.5, 100.5, 101.2, 102.2, and 103.5 eV, corresponding to crystalline Si^0, Si^+, Si^{2+}, Si^{3+}, and Si^{4+}, respectively (Figure 6-2b).[39] Si^{4+} is attributed to the formation of SiO_2, whereas the residual peaks of Si^+, Si^{2+}, and Si^{3+} may indicate by-products such as Mg_xSiO_y and SiO_x, which may result in inferior battery performance.[40,41] In addition, the binding energy in the O 1s region appeared at 532.3 eV, which is mainly attributed to SiO_2 (Figure 6-2c). However, an additional peak for Si HC at approximately 530 eV indicates the presence of Mg_xSiO_y and SiO_x.[42] For comparison, these materials were also analyzed using Raman spectroscopy (Figure 6-2d). Peaks are observed in the Raman spectra of ZIF-8 and ZIF-8@SiO_2 at 678, 1142, 1161, 1455, and 1488 cm^{-1}, which correspond to the vibrational modes of the 2-methylimidazole organic ligand.[43] The ZnO@SiO_2 showed no obvious peaks because amorphous peaks are overscattered under the same condition. The m-Si HC showed a main sharp peak centered at 520 cm^{-1} and two minor peaks centered at 295 and 950 cm^{-1} which was assigned to crystalline Si.[44] However, the Si HC showed a main broad peak centered at approximately 500 cm^{-1} corresponding to the amorphous Si feature.[45] Furthermore, Brunauer–Emmett–Teller (BET) analysis was performed to measure the surface area and pore size distribution of anode materials. The adsorption is denoted by filled square symbol, while desorption by hollow square symbol (Figure 6-2e). The BET surface areas of ZIF-8 NC, ZIF-8@SiO_2, ZnO@SiO_2 HC, m-Si HC, Si HC, and reference Si are 1701.78, 889.21, 619.02, 93.68, 39.22 and 43.01 $m^2\ g^{-1}$, respectively. The obvious sharp peaks for m-Si HC and reference Si at high relative pressure ($P/P_0 > 0.9$) indicate the existence of mesopores. The pore size distribution plot for m-Si HC shows that sharp peak of around 3 nm and broad peaks ranging from 5 nm to 60 nm are observed (Figure 6-2f). The XPS, pore size distribution and chemical composition for the resulting anode materials are discussed in more details (Supporting Information, Figures S8–S12 and Table S1).

The electrochemical properties of the m-Si HC, Si HC, and reference Si anodes were evaluated using discharge–charge galvanostatic measurements in the voltage range of 0.005–1.5 V (Figure 6-3). The Si HC, m-Si HC, and reference Si were coated with amorphous carbon by thermal decomposition of acetylene gas, and their characterizations are presented in Figures S13–S15. In

addition, we investigated the effect of SiO_2 shell thickness on the electrochemical properties of the resulting m-Si HC. Among 5, 15, and 50 nm-thick SiO_2 shells, the 15 nm-thick sample showed an optimum condition for the electrochemical performance. Morphological and electrochemical characterization of each sample was shown in Figure S16. As observed in Figure 6-3a, the optimized m-Si HC exhibited first discharge and charge capacities as high as 1728 and 2159 $mAhg^{-1}$, respectively, for a current rate of 0.05 C (1 C = 2.0 A g^{-1}). The initial Coulombic efficiency (ICE) was 80.1%, which is attributed to the irreversible reaction and formation of a solid-electrolyte interphase (SEI) along the surfaces. The Si HC and reference Si exhibited first discharge capacities of 948 $mAhg^{-1}$ (81.6% of ICE) and 1885 $mAhg^{-1}$ (80.9% of ICE), respectively. Although the reference Si exhibited a higher initial capacity than the m-Si HC anode, the capacity of the reference Si decayed with increasing cycles, resulting from aggregation of Si particles and/or pulverization of the electrode (Figure 6-3b). In contrast, the m-Si HC and Si HC anodes achieved capacities of 1208 $mAhg^{-1}$ (capacity retention of 73.1%) and 908 $mAhg^{-1}$ (capacity retention of 85.7%) over 300 cycles, respectively. These samples containing the residual silica and Mg_xSiO_y exhibited better cycling stability, which was attributed to the physical support acting as a mechanical buffer of internal stress induced by volumetric expansion of lithiated Si[46,47] and the passivation layer produced by the side reaction during the discharge–charge steps, although these features may cause the specific capacity. In particular, the suitable presence of residual silica and Mg_xSiO_y for m-Si HC was considered to be an optimum condition for long-term cycle life. Moreover, the m-Si HC exhibited excellent rate capabilities even at high current densities (Figure 6-3c). The discharge capacities of the m-Si HC anode were 1471, 1433, 1369, and 1050 $mAhg^{-1}$ at 1, 5, 10, and 15 C-rates, respectively. When the C-rate returned from 15 to 0.2, the discharge capacity was 1541 $mAhg^{-1}$, recovering completely from the initial capacity of 1501 $mAhg^{-1}$ (capacity retention of nearly 100%). This finding demonstrates that the high kinetic property is attributed to the morphology of m-Si HC because Li ions migrate through the short pathway in the mesoporous thin Si shell.[48] Cycle voltammetry and tap density data for anode materials are shown in Figure S17, S18, and Table S2.

To further confirm the other electrochemical properties, electrochemical impedance spectroscopy (EIS) was used to analyze the first and 300-cycled electrodes (Figure 6-3d). The resistivity of the reference Si increased from approximately 10 Ω in the first cycle to over 400 Ω in the final cycle, whereas that of m-Si HC remained at approximately 180 Ω even for 300 cycles. The increase of resistivity can explain the capacity decay because the semi-circles in this frequency region are correlated to SEI-layer-related resistivity.[49] The continuously cracked Si causes substantial decomposition of the electrolyte, which leads to thick and unstable SEI layers and capacity fading.[50] Thus, the m-Si HC exhibited better cycle retention and rate capability than

the reference Si. Furthermore, the m-Si HC anode exhibited outstanding cycle stability of 850 $mAhg^{-1}$ even at a 1C/1C-rate (charge/discharge) over 800 cycles with a high Coulombic efficiency per cycle of 99.8% (Figure 6-3e). The outstanding performance is attributed to the fine Si structure containing mesoporous hollow Si with large inner void space, which shortens the Li-ion diffusion length and simultaneously alleviates the internal stress generated from lithiated Si.

Additionally, the m-Si HC was evaluated with a full cell, where the m-Si HC/natural graphite anode (10 wt.%/90 wt.%, designed capacity of 550 $mAhg^{-1}$) was coupled with a commercial $LiCoO_2$ (LCO) cathode (Figure 6-4a). The cell had an initial areal density of 2.58 $mAhcm^{-2}$ with an ICE of 88.7% at a 0.05 C-rate. The reversible capacities steadily decreased up to approximately 73% of the initial reversible capacity after 100 cycles. The initial voltage profiles of the LCO cathode and graphite/m-Si HC are presented in Figure S19. The Coulombic efficiency during the repeated cycle is an important feature to estimate the full-cell performance.[51.,52] This parameter reached 99.5% within 14 cycles in this test and never decreased below 99.5% (Figure 6-4b).

To better understand the electrochemical properties, SEM cross-sectional examination was performed before and after 300 cycles (Figure 5). After 300 cycles, the electrode thickness variation of m-Si HC (volume expansion of ~47%, Figures 6-5a and b) was less than half the value of the reference Si (volume expansion of ~107%, Figures 6-5c and d). Top-view SEM analysis also revealed a clear difference between the m-Si HC and reference Si (Figure S20). After 300 cycles, the m-Si HC exhibited low volume expansion, and the shape of each nanoparticle was maintained with the help of the void spaces. In contrast, the entire surface of the reference Si electrode was agglomerated and covered with a thick SEI layer. These results emphasize the two main features of m-Si HC: the mesoporous structure and mechanical buffer layer. First, the porosity of the surface can accommodate expansion of Si during the lithiation process. Second, the inactive layer combined with active particles acts as a physical support to protect Si that is vulnerable to fracture.[53] The Nyquist plots and TEM images of reference Si, Si HC, and m-Si HC at the full lithiation state are shown in Figure S21 and S22.

From the core-level XPS spectra of C 1s, the lithium carbonate peaks for 290.0 eV are electrochemically undesirable for the anode; however, the intensities of the peaks for m-Si HC (Figure 6-6a) and reference Si (Figure 6-6c) are very low. More importantly, the LiF peak intensity at 684.7 eV for the m-Si HC (Figure 6-6b) is approximately three times larger than that for the reference Si (Figure 6-6d), which can stabilize the SEI layer of the Si surface.[54] These results indicate that the m-Si HC exhibits outstanding electrochemical properties, including long-term cycling stability and excellent rate capabilities.

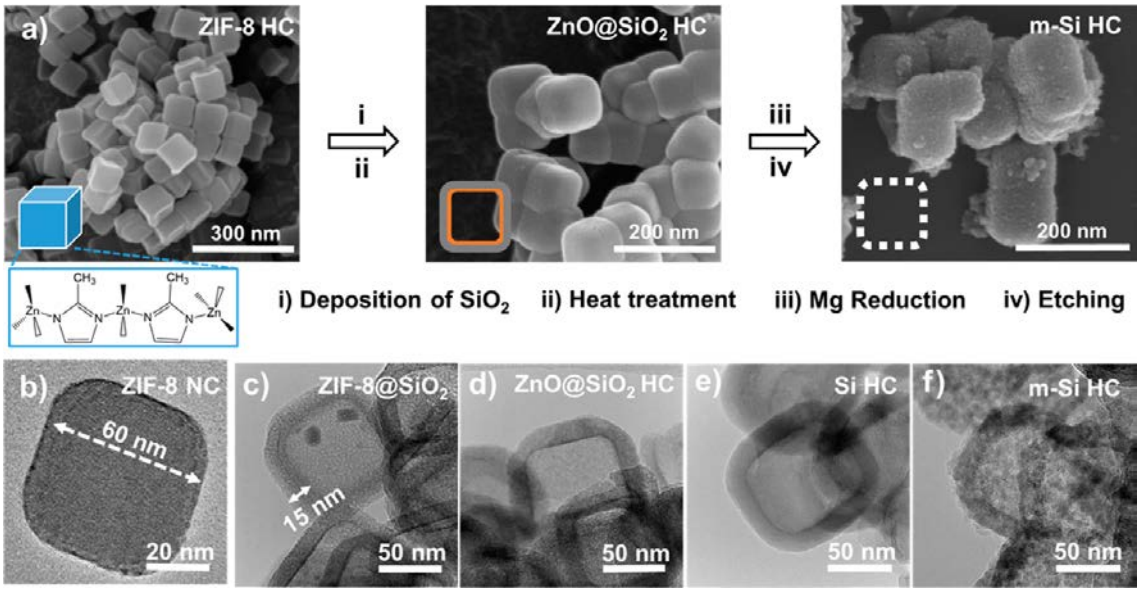

Figure 5-1. (a) SEM images illustrating synthetic routes of m-Si HC: (i) Deposition of SiO2 shell coating on ZIF-8 NC, (ii) heat treatment for calcination, (iii) magnesiothermic reduction, and (iv) etching with 1 M HCl. The illustrations in the inset of (a) depict the cubic morphology of ZIF-8 NC, SiO2 HC with inner ZnO, and mesoporous Si-HC. HRTEM images of (b) ZIF-8 nanocube (ZIF-8 NC), (c) ZIF-8@SiO2, (d) ZnO@SiO2 hollow nanocube (ZnO@SiO2 HC), (e) Si hollow nanocube (Si HC) after Mg reduction (weight ratio of sample to Mg = 1:0.4), and (f) mesoporous Si hollow nanocube (m-Si HC) after Mg reduction (weight ratio of sample to Mg = 1:0.8).

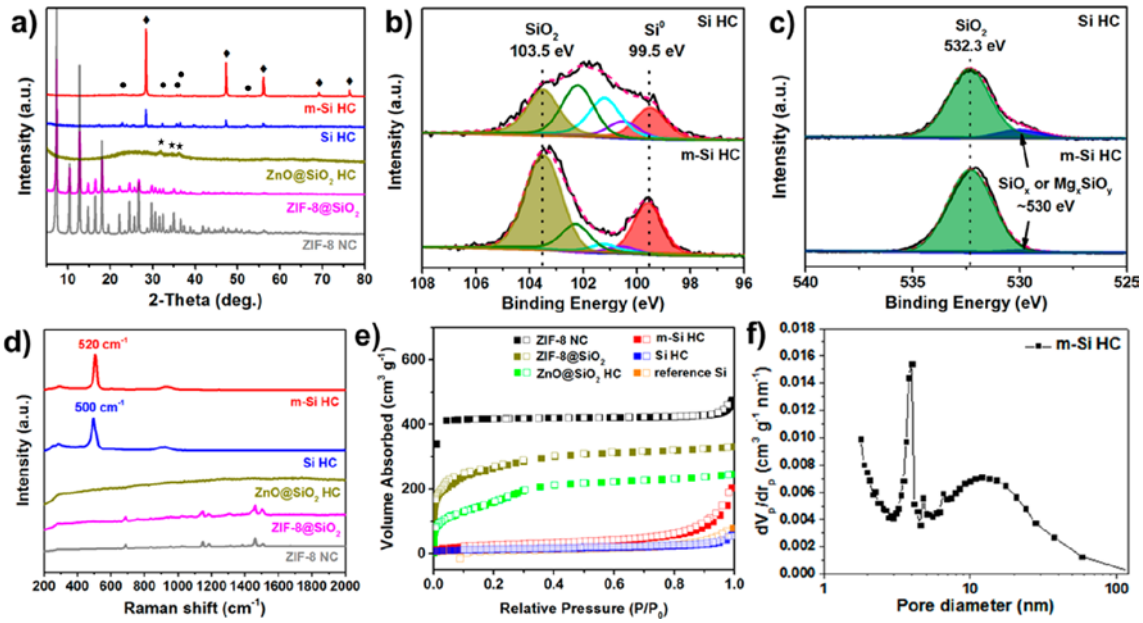

Figure 5-2. (a) XRD patterns of ZIF-8 NC, ZIF-8@SiO2, ZnO@SiO2 HC, Si HC, and m-Si HC. Core-level XPS spectra of (b) Si 2p and (c) O 1s for Si HC and m-Si HC. (d) Raman spectra. (e) The BET surface area calculated from nitrogen (77K) adsorption−desorption isotherms, denoted by solid/hollow square symbols, and (f) their corresponding pore size distribution of m-Si HC.

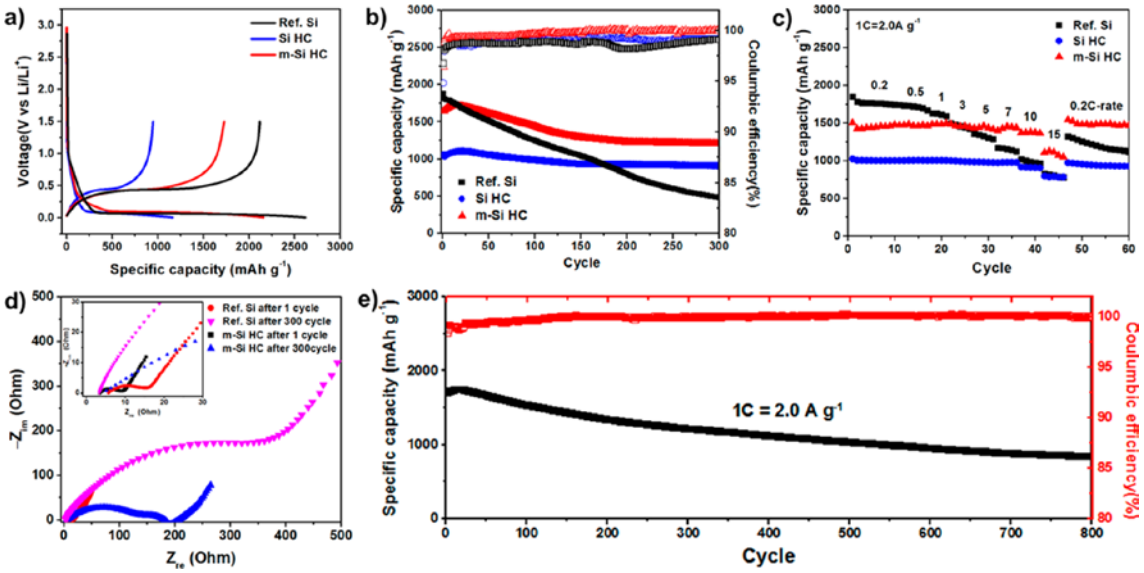

Figure 5-3. Electrochemical properties of m-Si HC, Si HC, and reference Si anodes. (a) First discharge−charge profiles at 0.05 C-rate. (b) Cycle retention test at 0.2 C-rate. (c) Rate capability at different delithiation rates (fixed lithiation rate: 0.2 C). (d) Nyquist plot of reference Si and m-Si HC after 1 and 300 cycles. (e) Long-term cycle retention of m-Si HC at 1C/1C-rate.

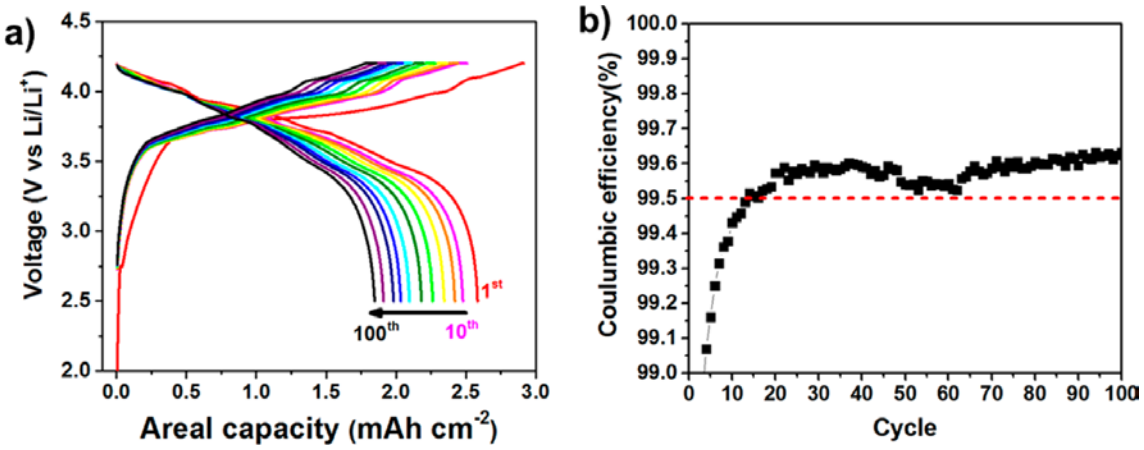

Figure 5-4. (a) Voltage profiles of full cell with LCO cathode and graphite/m-Si HC blending anode. (b) Coulombic efficiency of full cell determined from (a).

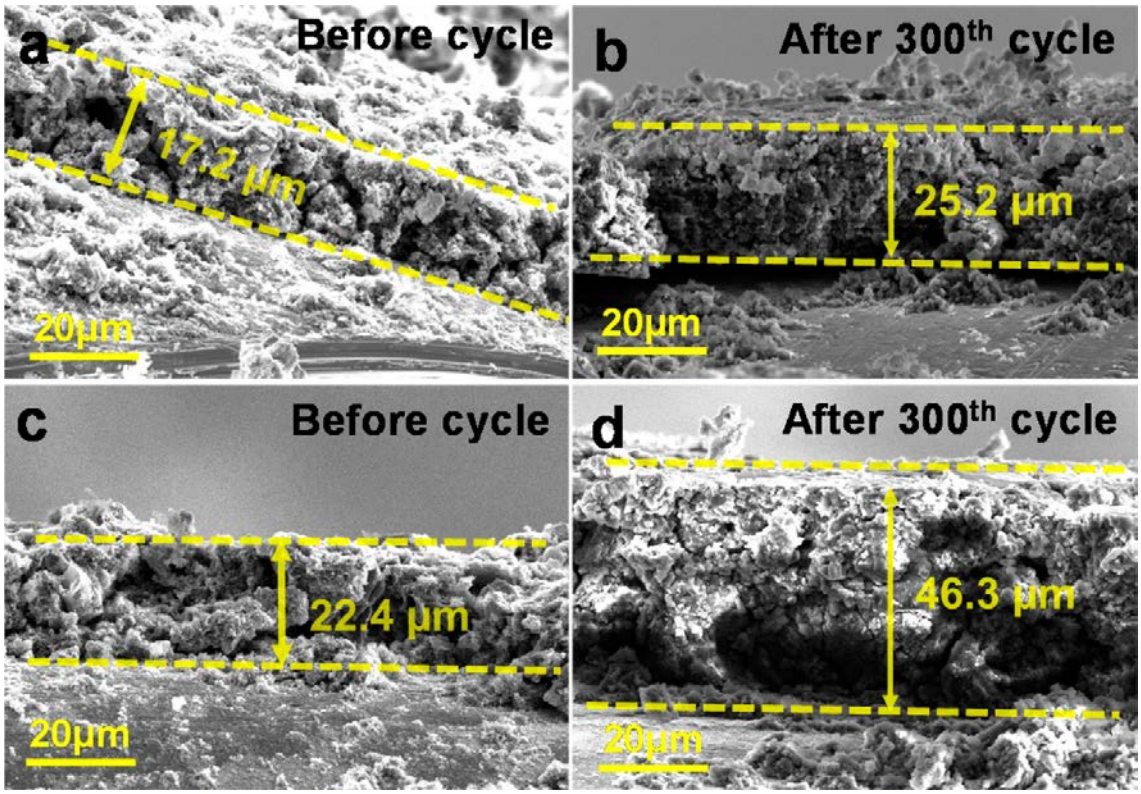

Figure 5-5. Cross-sectional SEM images of (a) m-Si HC before cycling, (b) m-Si HC after 300 cycles, (c) reference Si before cycling, and (d) reference Si after 300 cycles.

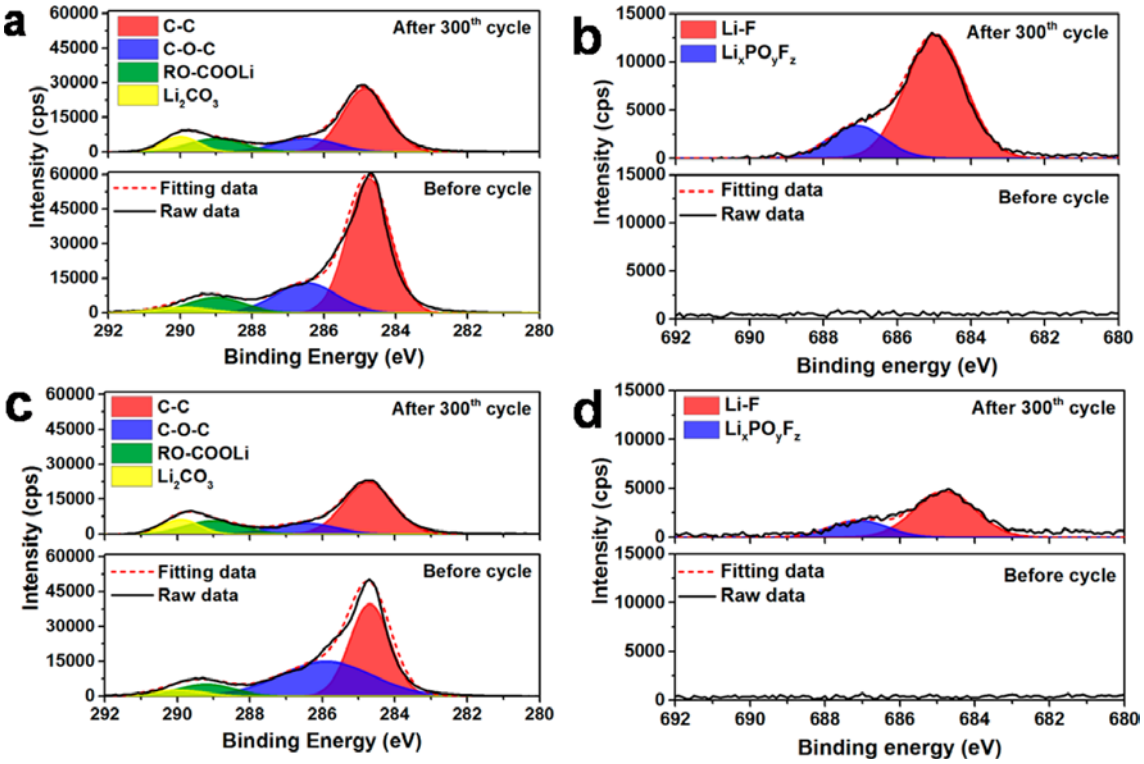

Figure 6-6. Core-level XPS spectra of m-Si HC for (a) C 1s before (bottom) and after (top) cycling and (b) F 1s before (bottom) and after (top) cycling. Core-level XPS spectra of reference Si for (c) C 1s before (bottom) and after (top) cycling and (d) F 1s before (bottom) and after (top) cycling.

5.4 Conclusion

In summary, we have developed a core–shell approach to synthesize mesoporous Si HCs derived from MOFs (ZIF-8). The 3D crystalline network of MOFs is an effective route to synthesize hollow Si materials because of its removable or sacrificial templates. This architecture was well preserved as the initial cube shape after various synthetic steps, including silica coating and chemical reduction. Each cell of well-designed m-Si HC was obtained having an internal void (~60 nm) and an external mesoporous shell (~15 nm) which is able to effectively accommodate the Si volume variations and form a stable SEI layer. Therefore, the resulting m-Si HC anode exhibited attractive electrochemical properties in LIBs, such as an excellent rate capability of 1050 $mAhg^{-1}$ at 15 C-rate, reversible capacity of 1728 $mAhg^{-1}$ at the first cycle, and long cycle stability of 850 $mAhg^{-1}$ after 800 cycles. Moreover, the full cell (m-Si HC & graphite/$LiCoO_2$, 2.9 $mAhcm^{-2}$) exhibited good cycle retention of 72% after 100 cycles at a 0.2 C-rate.

5.5 Reference

1. Liu, C.; Li, F.; Ma, L. P.; Cheng, H. M. Advanced materials for energy storage. *Adv. Mater.* **2010**, *22*, E28-E62.

2. Yoon, T.; Kim, K. S. One-Step Synthesis of CoS-Doped β-$Co(OH)_2$@Amorphous MoS_{2+x} Hybrid Catalyst Grown on Nickel Foam for High-Performance Electrochemical Overall Water Splitting. *Adv. Func. Mater.* **2016**, *26*, 7386-7393.

3. Armand, M.; Tarascon, J.-M. Building better batteries. *Nature* **2008**, *451*, 652-657.

4. McDowell, M. T.; Lee, S. W.; Ryu, I.; Wu, H.; Nix, W. D.; Choi, J. W.; Cui, Y. Novel size and surface oxide effects in silicon nanowires as lithium battery anodes. *Nano Lett.* **2011**, *11*, 4018-4025.

5. McDowell, M. T.; Lee, S. W.; Nix, W. D.; Cui, Y. 25th Anniversary Article: Understanding the Lithiation of Silicon and Other Alloying Anodes for Lithium-Ion Batteries. *Adv. Mater.* **2013**, *25*, 4966-4985.

6. Obrovac, M. N.; Christensen, L. Structural Changes in Silicon Anodes during Lithium Insertion/Extraction. *Electrochem. Solid-State Lett.* **2004**, *7*, A93-A96

7. Scrosati, B. Recent advances in lithium ion battery materials. *Electrochim. Acta* **2000**, *45*, 2461-2466.

8. Liu, X. H.; Zhong, L.; Huang, S.; Mao, S. X.; Zhu, T.; Huang, J. Y. Size-dependent fracture of silicon nanoparticles during lithiation. *ACS Nano* **2012,** *6*, 1522-1531.

9. Wu, H.; Chan, G.; Choi, J. W.; Ryu, I.; Yao, Y.; McDowell, M. T.; Lee, S. W.; Jackson, A.; Yang, Y.; Hu, L.; Cui, Y. Stable cycling of double-walled silicon nanotube battery anodes through solid-electrolyte interphase control. *Nat. Nanotechnol.* **2012**, *7*, 310-315.

10. Zhang, X.-W.; Patil, P. K.; Wang, C.; Appleby, A. J.; Little, F. E.; Cocke, D. L. Electrochemical performance of lithium ion battery, nano-silicon-based, disordered carbon composite anodes with different microstructures. *J. Power Sources* **2004**, *125*, 206-213.

11. Ge, M.; Rong, J.; Fang, X.; Zhou, C. Porous doped silicon nanowires for lithium ion battery anode with long cycle life. *Nano Lett.* **2012**, *12*, 2318-2323.

12. Park, M.-H.; Kim, M. G.; Joo, J.; Kim, K.; Kim, J.; Ahn, S.; Cui, Y.; Cho, J. Silicon nanotube battery anodes. *Nano Lett.* **2009**, *9*, 3844-3847.

13. Fu, K.; Yildiz, O.; Bhanushali, H.; Wang, Y.; Stano, K.; Xue, L.; Zhang, X.; Bradford, P. D. Aligned carbon nanotube-silicon sheets: a novel nano-architecture for flexible lithium ion battery electrodes. *Adv. Mater.* **2013**, *25*, 5109-5114.

14. Ryu, J.; Hong, D.; Choi, S.; Park, S. Synthesis of Ultrathin Si Nanosheets from Natural Clays for Lithium-Ion Battery Anodes. *ACS Nano* **2016**, *10*, 2843-2851.

15. Du, F. H.; Li, B.; Fu, W.; Xiong, Y. J.; Wang, K. X.; Chen, J. S. Surface binding of polypyrrole on porous silicon hollow nanospheres for Li-ion battery anodes with high structure stability. *Adv. Mater.* **2014**, *26*, 6145-6150.

16. Huang, X.; Yang, J.; Mao, S.; Chang, J.; Hallac, P. B.; Fell, C. R.; Metz, B.; Jiang, J.; Hurley, P. T.; Chen, J. Controllable synthesis of hollow Si anode for long-cycle-life lithium-ion batteries. *Adv. Mater.* **2014**, *26*, 4326-4332.

17. Yao, Y.; McDowell, M. T.; Ryu, I.; Wu, H.; Liu, N.; Hu, L.; Nix, W. D.; Cui, Y. Interconnected silicon hollow nanospheres for lithium-ion battery anodes with long cycle life. *Nano Lett.* **2011**, *11*, 2949-2954.

18. Lu, Z.; Liu, N.; Lee, H.-W.; Zhao, J.; Li, W.; Li, Y.; Cui, Y. Nonfilling carbon coating of porous silicon micrometer-sized particles for high-performance lithium battery anodes. *ACS Nano* **2015**, *9*, 2540-2547.

19. Li, X.; Yan, P.; Arey, B. W.; Luo, W.; Ji, X.; Wang, C.; Liu, J.; Zhang, J.-G. A stable nanoporous silicon anode prepared by modified magnesiothermic reactions. *Nano Energy* **2016**, *20*, 68-75.

20. Bok, T.; Choi, S.; Lee, J.; Park, S. Effective strategies for improving the electrochemical properties of highly porous Si foam anodes in lithium-ion batteries. *J. Mater. Chem. A* **2014**, *2*, 14195-14200.

21. Yaghi, O. M.; O'Keeffe, M.; Ockwig, N. W.; Chae, H. K.; Eddaoudi, M.; Kim, J. Reticular synthesis and the design of new materials. *Nature* **2003**, *423*, 705-714.

22. Jiang, Z.; Li, Z.; Qin, Z.; Sun, H.; Jiao, X.; Chen, D. LDH nanocages synthesized with MOF templates and their high performance as supercapacitors. *Nanoscale* **2013**, *5*, 11770-11775.

23. Han, Y.; Qi, P.; Zhou, J.; Feng, X.; Li, S.; Fu, X.; Zhao, J.; Yu, D.; Wang, B. Metal-Organic Frameworks (MOFs) as Sandwich Coating Cushion for Silicon Anode in Lithium Ion Batteries. *ACS Appl. Mater. Interfaces* **2015**, *7*, 26608-26613.

24. Song, Y.; Zuo, L.; Chen, S.; Wu, J.; Hou, H.; Wang, L. Porous Nano-Si/Carbon Derived from Zeolitic Imidazolate Frameworks@Nano-Si as Anode Materials for Lithium-Ion Batteries.

Electrochim. Acta **2015**, *173*, 588-594.

25. Han, Y.; Qi, P.; Feng, X.; Li, S.; Fu, X.; Li, H.; Chen, Y.; Zhou, J.; Li, X.; Wang, B. *In situ* growth of MOFs on the surface of Si nanoparticles for highly efficient lithium storage: Si@MOF nanocomposites as anode materials for lithium-ion batteries. *ACS Appl. Mater. Interfaces* **2015**, *7*, 2178-2182.

26. Yan, N.; Wang, F.; Zhong, H.; Li, Y.; Wang, Y.; Hu, L.; Chen, Q. Hollow porous SiO_2 nanocubes towards high-performance anodes for lithium-ion batteries. *Sci. Rep.* **2013**, *3*, 1568-1573.

27. Hu, L.; Chen, Q. Hollow/porous nanostructures derived from nanoscale metal–organic frameworks towards high performance anodes for lithium-ion batteries. *Nanoscale* **2014**, *6*, 1236-1257.

28. Jiang, Z.; Li, Z.; Qin, Z.; Sun, H.; Jiao, X.; Chen, D. LDH nanocages synthesized with MOF templates and their high performance as supercapacitors. *Nanoscale* **2013**, *5*, 11770-11775.

29. Park, K. S.; Ni, Z.; Cote, A. P.; Choi, J. Y.; Huang, R.; Uribe-Romo, F. J.; Chae, H. K.; O'Keeffe, M.; Yaghi, O. M. Exceptional chemical and thermal stability of zeolitic imidazolate frameworks. *Proc. Natl. Acad. Sci. USA* **2006**, *103*, 10186-10191.

30. Yang, H.; Kruger, P. E.; Telfer, S. G. Metal-organic framework nanocrystals as sacrificial templates for hollow and exceptionally porous titania and composite materials. *Inorg. Chem.* **2015**, *54*, 9483-9490.

31. Bao, Z.; Weatherspoon, M. R.; Shian, S.; Cai, Y.; Graham, P. D.; Allan, S. M.; Ahmad, G.; Dickerson, M. B.; Church, B. C.; Kang, Z.; Abernathy, H. W., 3rd; Summers, C. J.; Liu, M.; Sandhage, K. H. Chemical reduction of three-dimensional silica micro-assemblies into microporous silicon replicas. *Nature* **2007,** *446*, 172-175.

32. Sun, H.; Xin, G.; Hu, T.; Yu, M.; Shao, D.; Sun, X.; Lian, J. High-rate lithiation-induced reactivation of mesoporous hollow spheres for long-lived lithium-ion batteries. *Nat. commun.* **2014**, *5*, 4526-4533

33. Chen, Y.; Liu, L.; Xiong, J.; Yang, T.; Qin, Y.; Yan, C. Porous Si nanowires from cheap metallurgical silicon stabilized by a surface oxide layer for lithium ion batteries. *Adv. Funct. Mater.* **2015**, *25*, 6701-6709.

34. Wen, X.; Wei, X.; Yang, L.; Shen, P. K. Self-assembled FeS_2 cubes anchored on reduced graphene oxide as an anode material for lithium ion batteries. *J. Mater. Chem. A* **2015,** *3*, 2090-2096.

35. Li, Z.; Zeng, H. C. Surface and Bulk Integrations of Single-Layered Au or Ag Nanoparticles onto Designated Crystal Planes of ZIF-8. *Chem. Mater.* **2013**, *25*, 1761-1768.

36. Li, Z.; Zeng, H. C. Armored MOFs: enforcing soft microporous MOF nanocrystals with hard mesoporous silica. *J. Am. Chem. Soc.* **2014**, *136*, 5631-5639.

37. Jung, D. S.; Ryou, M. H.; Sung, Y. J.; Park, S. B.; Choi, J. W. Recycling rice husks for high-capacity lithium battery anodes. *Proc. Natl. Acad. Sci. USA* **2013,** *110*, 12229-12234.

38. Kim, K. H.; Lee, D. J.; Cho, K. M.; Kim, S. J.; Park, J. K.; Jung, H. T. Complete magnesiothermic reduction reaction of vertically aligned mesoporous silica channels to form pure silicon nanoparticles. *Sci. Rep.* **2015**, *5*, 9014-9020.

39. Himpsel, F.; McFeely, F.; Taleb-Ibrahimi, A.; Yarmoff, J.; Hollinger, G. Microscopic structure of the SiO_2/Si interface. *Phys. Rev. B* **1988,** *38*, 6084-6096.

40. Kim, H.; Seo, M.; Park, M. H.; Cho, J. A critical size of silicon nano-anodes for lithium rechargeable batteries. *Angew. Chem. Int. Ed.* **2010**, 49, 2146-2149.

41. Jia, Z. J.; Li, M.; Liu, Q.; Xu, X. C.; Cheng, Y.; Zheng, Y. F.; Xi, T. F.; Wei, S. C. Micro-arc oxidization of a novel Mg–1Ca alloy in three alkaline KF electrolytes: Corrosion resistance and cytotoxicity. *Appl. Surf. Sci.* **2014**, 292, 1030-1039.

42. Márquez, F.; Morant, C.; López, V.; Zamora, F.; Campo, T.; Elizalde, E. An alternative route for the synthesis of silicon nanowires *via* porous anodic alumina masks. *Nanoscale res. Lett.* **2011,** *6*, 1-7.

43. Kumar, R.; Jayaramulu, K.; Maji, T. K.; Rao, C. Hybrid nanocomposites of ZIF-8 with graphene oxide exhibiting tunable morphology, significant CO_2 uptake and other novel properties. *Chem. Commun.* **2013,** *49*, 4947-4949.

44. Li, M.; Hou, X.; Sha, Y.; Wang, J.; Hu, S.; Liu, X.; Shao, Z. Facile spray-drying/pyrolysis synthesis of core–shell structure graphite/silicon-porous carbon composite as a superior anode for Li-ion batteries. *J. Power Sources* **2014,** *248*, 721-728.

45. Veprek, S.; Sarott, F.-A.; Iqbal, Z. Effect of grain boundaries on the Raman spectra, optical absorption, and elastic light scattering in nanometer-sized crystalline silicon. *Phys. Rev. B* **1987,** *36*, 3344-3350.

46. Yang, L. Y.; Li, H. Z.; Liu, J.; Sun, Z. Q.; Tang, S. S.; Lei, M. Dual yolk-shell structure of carbon and silica-coated silicon for high-performance lithium-ion batteries. *Sci. Rep.* **2015,** *5*, 10908-10916.

47. Wang, J. W.; He, Y.; Fan, F.; Liu, X. H.; Xia, S.; Liu, Y.; Harris, C. T.; Li, H.; Huang, J. Y.; Mao, S. X.; Zhu, T. Two-phase electrochemical lithiation in amorphous silicon. *Nano Lett.* **2013,** *13*, 709-715.

48. Liu, X. H.; Wang, J. W.; Huang, S.; Fan, F.; Huang, X.; Liu, Y.; Krylyuk, S.; Yoo, J.; Dayeh, S. A.; Davydov, A. V.; Mao, S. X.; Picraux, S. T.; Zhang, S.; Li, J.; Zhu, T.; Huang, J. Y. *In situ* atomic-scale imaging of electrochemical lithiation in silicon. *Nat. Nanotechnol.* **2012,** *7*, 749-756.

49. Guo, J.; Sun, A.; Chen, X.; Wang, C.; Manivannan, A. Cyclability study of silicon–carbon composite anodes for lithium-ion batteries using electrochemical impedance spectroscopy. *Electrochim. Acta* **2011,** *56*, 3981-3987.

50. Li, M.-Q.; Qu, M.-Z.; He, X.-Y.; Yu, Z.-L. Effects of electrolytes on the electrochemical performance of Si/graphite/disordered carbon composite anode for lithium-ion batteries. *Electrochim. Acta* **2009,** *54*, 4506-4513.

51. He, Y.; Yu, X.; Wang, Y.; Li, H.; Huang, X. Alumina-coated patterned amorphous silicon as the anode for a lithium-ion battery with high coulombic efficiency. *Adv. Mater.* **2011,** *23*, 4938-4941.

52. Ko, M.; Chae, S.; Ma, J.; Kim, N.; Lee, H.-W.; Cui, Y.; Cho, J. Scalable synthesis of silicon-nanolayer-embedded graphite for high-energy lithium-ion batteries. *Nature Energy* **2016,** *1*, 16113-16120.

53. Choi, S.; Bok, T.; Ryu, J.; Lee, J.-I.; Cho, J.; Park, S. Revisit of metallothermic reduction for macroporous Si: compromise between capacity and volume expansion for practical Li-ion battery. *Nano Energy* **2015,** *12*, 161-168.

54. Nie, M.; Abraham, D. P.; Chen, Y.; Bose, A.; Lucht, B. L. Silicon Solid Electrolyte Interphase (SEI) of Lithium Ion Battery Characterized by Microscopy and Spectroscopy. *J Phys. Chem. C* **2013,** *117*, 13403-13412.

Chapter VI. Mechanical mismatch-driven structural deformation in Si/C nanosheet for rechargeable Li-ion battery

6.1 Introduction

Developing a high capacity electrode material for lithium-ion batteries (LIBs) has been a major concern owing to growing demands for electric vehicles (EVs) [1-4]. Previous studies have shown that structure modification in nanoscale, beneficial interface control, and introduction of external support on typical lithium alloying materials (*i.e*. Si, Ge, Sn, etc.) significantly improved the cycle stability and suppress the volume variation of electrodes [5-8]. Si, which delivers the highest gravimetric capacity of 3579 mAh g^{-1} at room temperature, has been extensively explored in their Li^+ storage properties by controlling the size and dimensions (0D, 1D, 2D, and 3D) where it becomes smaller under 150 nm of fracture point during lithiation and delithiation [9, 10]. Those nanostructured Si materials, including spherical particles, wires, films, tubes, and porous structures, facilitate stress relief and shorten the ionic/electric path [11-15]. Despite significantly enhanced performances such as cycle life and fast charging ability, there still remained dissatisfied factors to fully realize the commercialization of Si-based anodes with high-energy-density. For example, nano-scaled 0D Si has inevitably a low tap density that is an important factor of a full-cell design [16]. 1D Si materials are not suitable for mass production due to unveiled feasible approach with high production cost. Since 3D Si with multiple types of pores has high surface area, it consumes excess amounts of electrolyte which forms thick and irregular solid-electrolyte interphase (SEI), leading to a huge irreversible capacity loss [17-19]. Compared to other dimensions, 2D Si materials have been rarely investigated both in their synthesis, electrochemical behaviors upon Li^+ uptake, deformation mode, and stress distributions [20].

In this work, we prepared 2D Si using a chemical vapor deposition (CVD) process on a sacrificing inorganic template which can be re-used *via* recyclable process. After thin silicon layers are conformally coated on a relatively large inorganic substance, 2D Si is synthesized by etching out the template. For structural definition of 2D Si, the design of Si sheet is aimed at the nano-sized thickness and micron-sized lateral length. Thin sheet structure is electrochemically desirable under the critical point of a breakable Si size, then it also provides the short Li-ion diffusion length, enabling high rate capability [21]. In addition, the spacious horizontal dimension without pores can be accommodated the high tap density of anode material, then it also has little surface area to volume ratio, resulting in high initial coulombic efficiency (ICE). Typically, carbon

coating layer on the Si surface improved the electrochemical properties, However, few studies have parallelly conducted the fundamental-experimental approach related to chemo-electrochemo-mechanical properties between Si and carbon [22]. Beyond the improvement of electrochemical performance, this article deals with phenomena caused by the mechanical mismatch of carbon-coated Si through the *in-situ* transmission electron microscopy (TEM) and computational study. It will lead to an important consequence for the intensive analysis of substances and phenomena that have been studied less in-depth so far.

6.2 Experimental

Preparation of NaCl.

Commercial NaCl (SAMCHUN chemical, 99.0%) has a dimension of 1 x 1 x 1 mm^3. In order to downsize as the NaCl template which is suitable for battery active material, 20 μm of NaCl was prepared using a precipitation method. 200 mL of EtOH was rapidly introduced in 100 mL of saturated NaCl-deionized (DI) water solution with vigorous stirring for a second to promote the recrystallization of NaCl, then the solution turned opaque due to the precipitation of white NaCl crystals. Subsequently, NaCl was filtered and dried in vacuum [35, 36].

Preparation of 2D Si.

Silane gas with six nine (99.9999%) purity was thermally decomposed in a rotary furnace which contains NaCl as a template. The fixed variables are the decomposition temperature of silane (550°C), flow rate of silane gas (50 sccm), and amount of template (50 g), while the reaction time was controlled with 10 min, 15 min, 20 min and 90 min to obtain Si with thickness of 50 nm, 100 nm, 150 nm and 380 nm on NaCl [33]. After pyrolysis of silane, NaCl was selectively removed by intense stirring in DI water and subsequently 2D Si with each thickness was obtained after filtration and drying step. The resulting 2D Si sheet was uniformly coated by amorphous carbon by decomposition of acetylene gas (C_2H_2) at 900 °C for 5 min.

Recycle of NaCl.

NaCl is continuously reusable through the consecutive recrystallization of NaCl. After the template-removal step from Si-coated NaCl, the NaCl solution passed through the filter paper. Double volume of EtOH compared to the passed solution was added into the NaCl solution. Then, the NaCl crystals with identical size was precipitated within seconds. The weight percent of solidified NaCl crystal was about 27.7 wt.%, while the amount of unprecipitated NaCl, which still remains in solution, was about 71.3 wt.% in average. About 99.0 wt.% of template can be recycled every time, resulting in just 1% of loss.

Material characterization.

Microstructural evolution was investigated using scanning electron microscopy (SEM, Verios 460, FEI), transmission electron microscopy (JEM-2100F, JEOL), Raman (NRS-3000, JASCO spectrometer), XRD (Bruker D8-Advance) and Brunauer-Emmett-Teller analysis (BET, ASAP2020, Micromeritics Instruments).

Electrochemical characterization.

Electrochemical test was evaluated using 2032 coin-type cell. 2D Si-contained electrode was composed of 80 wt.% 2D Si as an active material, 10 wt.% binder ((poly(acrylic acid)/sodium carboxymethyl cellulose, PAA/CMC, 50 wt.%/50 wt.%, Sigma-Aldrich)) and 10 wt.% super-P (TIMCAL). The loading levels of series of 2D Si was about 1.1 mg cm^{-2}. The operating voltage window of 2D Si was from 0.005 and 1.5V at a 0.05-20 C-rate. Commercial LCO (L&F material) was used as a cathode active material and its electrode composition was 95:2:3 in weight (LCO : polyvinylidene fluoride (PVdF) : super-P) with 19.8 mg cm^{-2} of loading level. Graphite/2D Si blending electrode consisted of graphite, 50 nm 2D Si, styrene butadiene rubber (SBR), CMC and super-P (86.2 : 9.6 : 1.5 : 1.7 : 1, in weight) with 5.6 mg cm^{-2} of loading level. All electrodes were dried in vacuum at 110 ^{o}C overnight after slurry-spreading on current collector, Cu and Al foil for anode and cathode, respectively. The ethylene carbonate/diethyl carbonate (PANAX starlyte, 3/7 in volume) with 10 wt.% of fluoroethylene carbonate was used as an electrolyte. The full-cell design was about 1.1 of N/P ratio and was operated in the voltage range between 2.5 and 4.2V. All type of cells carried out using a cycle tester (WBCS3000 battery systems, Wonatech).

***In situ* EIS.**

A set of multiple impedance spectra were measured every 30 min by the galvanostatic EIS at a constant current mode (0.1C) during lithiation/delithiation, since the potantiostat of *in situ* EIS system consisted of two different channels: one was for measuring impedance spectra, the other was for recording voltage profiles. Input signals were generated by the superposition of sinusoidal current waves of 10mA amplitude at 200 kHz to 1 Hz (VSP-300, BioLogic).

***In-situ* TEM measurements.**

In-situ TEM measurements were carried out with a Nanofactory TEM-STM holder inside a Titan 80-300 scanning/transmission electron microscope (S/TEM). One probe consisted of 2DSi samples which were drop-cast onto a gold wire as a working electrode, and the other probe was a tungsten probe with a piece of Li metal attached to the tip as a counter electrode. The probes were affixed to the TEM holder in an Ar-filled glovebox and transported to the TEM in an airtight container, where the holder was then removed and inserted into the TEM. A native Li_2O layer formed by a short exposure (3-5s) of Li to air functions as a solid-state electrolyte [10, 37]. Inside the TEM, a piezo-positioner is used to move the Li/Li_2O electrode into contact with the 2DSi samples. After contact, a bias of −3.0 V was applied to initiate lithiation. Once lithiation was completed, a bias of 3 V was applied for delithiation. In order to drive the Li^+ ions through the solid electrolytes,

applied potentials are larger than those used in real Li-Si cell. However, this is common for in situ TEM studies; for example, *in situ* lithiation of Si requires the application of −2.0 V vs Li electrode, whereas the lithiation window in Li−Si half cells is 0 to +2.0 V vs Li/Li_2O. This difference does not appear to change the behavior of the material [37, 38].

6.3 Results and discussion

Synthesis and characterization of 2D Si

Schematic illustration in Fig. 1d shows the large-scale synthetic process of 2D Si using cost-effective recyclable inorganic templates. The starting material was a table salt (sodium chloride, NaCl) as an inorganic template (Fig. 1a). Subsequently, silane (SiH_4) gas was thermally decomposed at 550 °C, generating the uniform Si-coated NaCl (NaCl@Si, Fig. 1b,c) without any deformation of template. Then, NaCl was easily removed in deionized water (DI water) after vigorous stirring and the final 2D Si products are obtained by filtration [23]. As shown in Fig. 1e, f, and g, plane 2D Si is synthesized in a large scale. Depending on the size of template used, lateral length of 2D Si can be controllable for suitable range of active materials (<20 μm). Therefore, NaCl with various sizes were prepared through recrystallization method from micron to millimeter scale (Supplementary Fig. 1). In a typical procedure, ethanol non-solvent initiates recrystallization of saturated aqueous NaCl solution to precipitate NaCl in a target dimension. Furthermore, other inorganic templates can be substituted for NaCl such as KCl, Li_2SO_4 and Na_2CO_3 (Supplementary Fig. 2). They should be durable at the decomposition temperature of silane without any deformation and has both high water-solubility and insoluble in EtOH or acetone. After the synthesis of 2D Si, NaCl can be reusable by recrystallization of the unfiltered NaCl solution with only 1% of loss (Supplementary Fig. 3).

As-synthesized 2D Si has a flat film morphology (thickness in nanometer and length/width in micrometer) with negligible pores (Fig. 1h) and amorphous structure. The size of 2D Si is intentionally tunable *via* synthetic conditions such as decomposition time and temperature of silane, quantity of template, and dimension of template. For comparison, 50 nm, 100 nm, 150 nm, 380 nm-thick 2D Si were prepared with control of silane decomposition time (Supplementary Fig. 4). Surface area of each 2D Si material is varied ranging from 2.42 m^2/g (380 nm) to 10.79 m^2/g (50 nm 2D Si) as a function of thickness of 2D Si. It shows relatively lower value compared to that of 50 nm-sized Si particles (16.95 m^2/g). Micro-scaled lateral dimension of 2D Si contributes to the low surface-to-volume ratio unlike other nanomaterials. It is clearly confirmed that as-synthesized 2D Si is amorphous phase, while it shows phase transition into polycrystalline after carbon coating (2D Si@C) at 750 °C and 900 °C (Supplementary Fig. 6) as confirmed by X-ray diffraction (XRD, Fig. 1j) and Raman spectra (Fig. 1k). The temperature-induced peak shift in Raman spectrum occurs from 493 cm^{-1} to 516 cm^{-1} which is a fingerprint range of pure Si to determine their phase and typical crystal planes of Si powder are developed after thermal annealing as shown in XRD results [24]. It is further corroborated by selected area electron diffraction (SAED) patterns in TEM analysis, manifesting typical amorphous and polycrystalline

Si ring patterns before and after carbon coating process (Fig. 1g and Supplementary Fig.3) [25, 26]. Additionally, Fig. 1i shows the photographs of samples obtained at each synthetic sequence. This proposed design demonstrates that 2D Si materials can be produced in a scalable way, which utilizes recyclable salt templating and chemical decomposition.

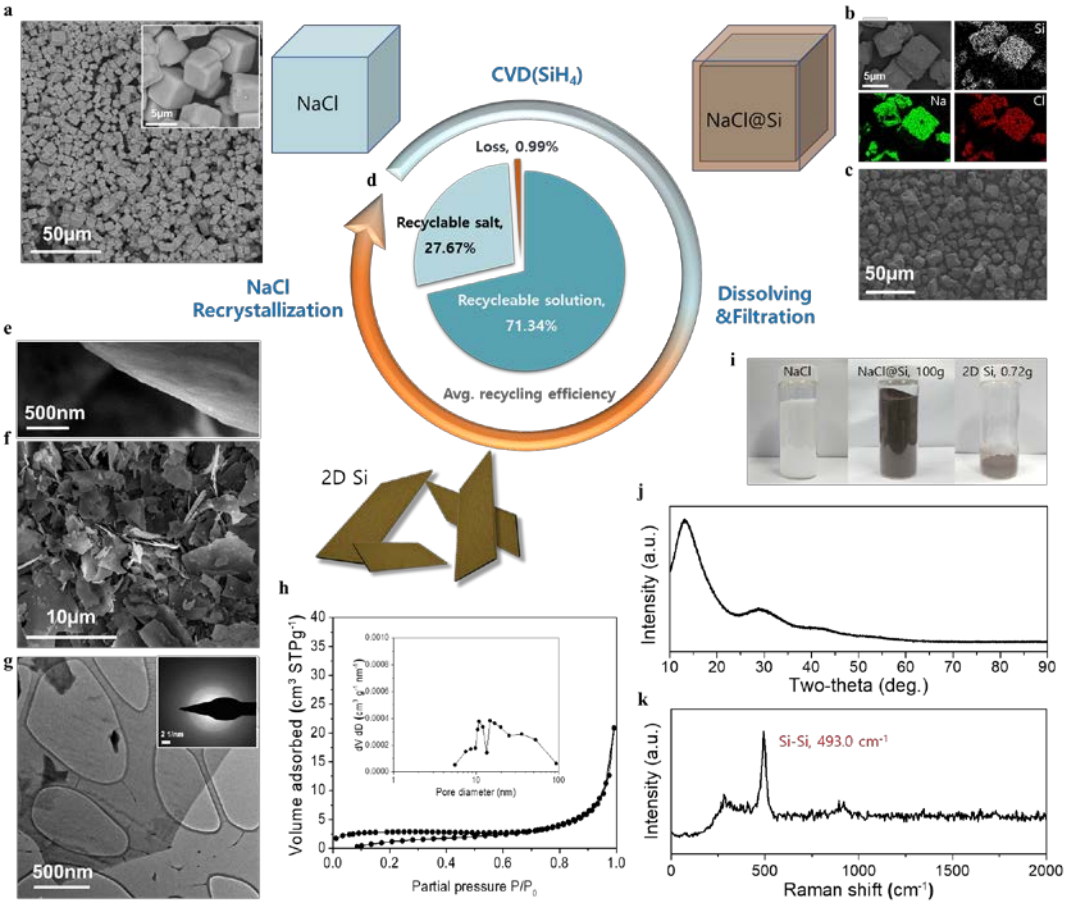

Figure 6-1. The schematic illustration of the synthetic process and characterization of each step. (a) SEM images of recrystallized NaCl by EtOH (inset: high-magnification) (b) Energy dispersive spectrometry (EDS) analysis and (c) SEM image of 50nm-thick Si-coated NaCl (d) Pie chart of NaCl recycle efficiency in average. (e) High, (f) low-magnification SEM image, (g) TEM image (inset: electron diffraction), (h) N2 adsorption-desorption isotherms (inset: BJH pore size distribution), (j) XRD pattern and (k) Raman spectra of 50nm-thick 2D Si.

Electrochemical performance of 2D Si

The series of galvanostatic test for 2D Si anodes were conducted with the thickness variation of 2D Si such as 50 nm, 100 nm, 150 nm and 380 nm (Fig. 2 and Supplementary Fig. 7). 380 nm-thick 2D Si achieved 2331 mAh g^{-1} of discharge capacity, corresponding to 46.3% of low ICE due to excessive threshold of a tolerable Si dimension on lithiation. On the contrary, 50 nm-thick 2D Si showed 2411 mAh g^{-1} of specific capacity and 90.0% of ICE in the first cycle owing to an electroactive thin sheet. 100 nm-thick 2D Si delivered the 2256 mAh g^{-1} and 92.3% in discharge capacity and ICE, respectively. Most of 2D Si anodes delivered over 90.0% of ICE, which records the highest value of ICE among previously reported other 2D Si anodes [27-31]. As expected, thickness-dependent electrochemical properties are revealed in the following cycles. The thinner the 2D Si (50 nm) is, the more superior capacity retention (85% after 200 cycles at 0.5 C-rate) and rate capability (91% at 10 C-rate and 75% at even 20 C-rate) is over other control samples. These outstanding performances are ascribed to well-designed dimensional approach. The thinner dimension of 2D Si in vertical direction accelerates a fast diffusion of Li^+ and simultaneously spacious extension in lateral direction leads to low surface-to-volume ratio which can suppress a large amount of side reactions. That is why thin and spacious layer can accommodate both high ICE value and high rate capability, despite a large degree of lithiation.

The above lithium storage properties are well matched with *in-situ* galvanostatic electrochemical impedance spectroscopy (EIS) results as shown in Fig. 2d [31, 32]. A conventional potentiostatic EIS cannot reflect the time-variant overall process between electrolyte and electrode during lithiation/delithiation, while a galvanostatic measurement of *in situ* EIS can define the rate-dependent kinetics of electrode by applying the sinusoidal current signal. Typical 'w' pattern implicitly indicates that the lithiation of Si is obviously shown as a function of state - of-charge (SOC). During an initial stage of SOC, the resistance gradually decreased due to the formation of crystalline lithiated Si (Li_xSi) that enhanced charge transfer kinetics consequently. On the other hand, when Si is fully charged with Li^+, it increases the resistance of a cell, because the fully charged lithium silicide ($Li_{15}Si_4$) surface obstructs additional diffusion of Li^+ inside. 50 nm-thick 2D Si shows 85% of SOC after 200 cycles and under 50Ω, while thicker 2D Si have less SOC (<60%) at same cycle number and higher resistance. It implies that 50 nm-thick 2D Si maintains better electric contact during repeated cycles. Interestingly, 50 nm-thick Si presents a stable long-term cycle life even at harsh conditions (1C-rate/1C-rate for lithiation/delithiation), in which the reversible capacity remains over 1070 mAh g^{-1} and 744 mAh g^{-1} after 500 and 1000 cycles, respectively.

Moreover, the CE of each cycle gradually increases and records the average coulombic efficiency of 99.76% over 1000 cycles, which implies that severe issues originated from

expansion of Si anodes does not occur such as electrolyte depletion and pulverization of active material from current collector. Such a stable capacity retention is also demonstrated by monitoring the change in electrode thickness through *ex situ* analysis. Fig. 2f and Supplementary Fig. S11 show the expansion ratio of electrode as a function of cycle number. The lithiation-induced swelling of 50 nm-thick 2D Si has only 49.3% after 100 cycles, whereas 100 nm-thick 2D Si shows 68.3%. It is critical mission to achieve cyclability and rate capability with high initial reversibility at the same time in conventional nanostructured Si anodes, which take great priority for full cell design [33]. Thus, our 2D Si anodes look quite suitable for full cell implementation. As a demonstration, the full cell comprising commercial $LiCoO_2$ (LCO) as a cathode and graphite/2D Si (600 mAh g^{-1} level, 10wt.% of 2D Si) blending anode was fabricated by coupling with 2D Si with highest ICE (Supplementary Fig. 12). To be in line with commercial electrode, blending systems are selected for precise comparison, since major companies still does not construct pure Si anodes for practical approach. The designed full cell exhibits the 3.16 mAh cm^{-2} of areal capacity with 89.94% of ICE at a 0.1C-rate in the operating voltage between 2.5 and 4.2V (Fig. 2g and Supplementary Fig. 13). Remarkably, it delivered over 2.0 mAh cm^{-2} of areal discharge capacity after 100 cycles at a 0.5C-rate. Its coulombic efficiency of each cycle was recorded in Fig. 2h and reached to 99.5% which is generally known as industrial standard to evaluate the full cell within the first 20 cycles.

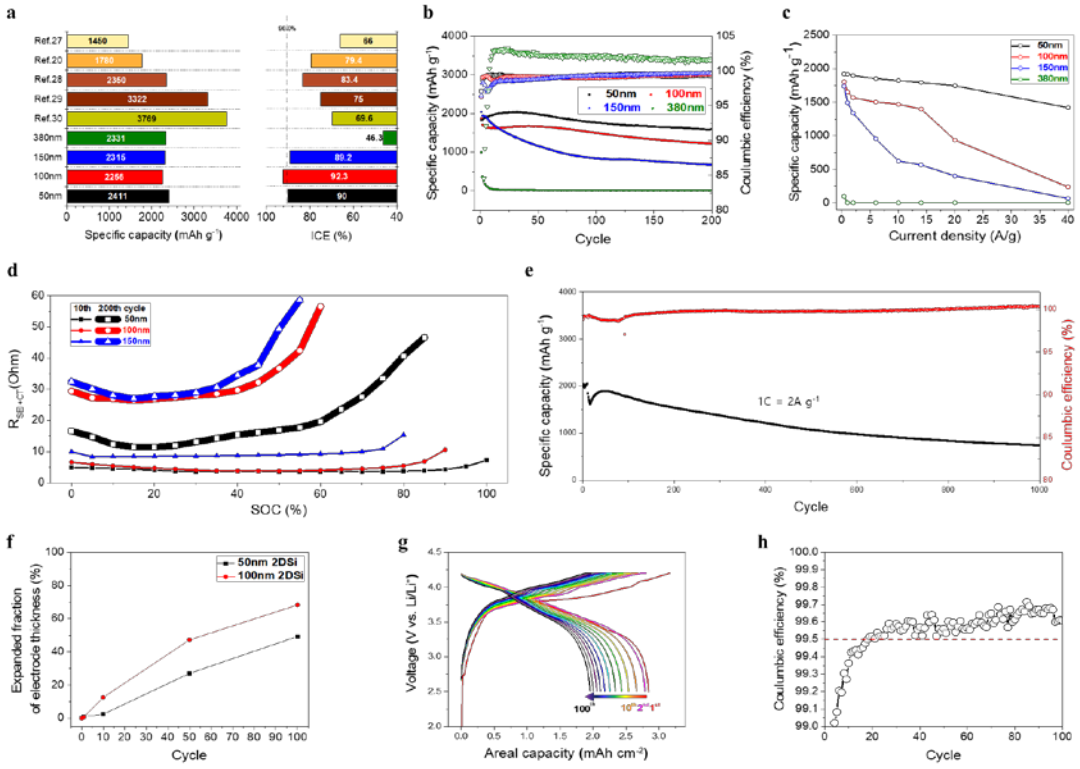

Figure 6-2. electrochemical performance of 2D Si. (a) the results of formation cycle for 2D Si. (b) cycle retention at a rate of 0.2C. (c) rate capability test operated from 0.2C to 20C. (d) Polarization resistance profiles of 2D Si during 10th and 200th lithiation. (e) long-term cyclability test at 1C/1C for charge/discharge. (f) Changes in thickness of electrode as a function of cycle. (g) series of voltage profile at a 0.2C for full-cell assembled the combination of LCO and graphite/2D Si blending. (h) An enlargement of full-cell coulombic efficiency with the red dash line at 99.5%.

Lithiation/delithiation behavior of 2D Si

Apart from macroscopic analysis, it does matter how single particle deforms upon lithiation/delithiation and expect that the resulting structures are incorporated in composite electrodes [34]. To the best of our knowledge, 2D Si materials have not been unveiled through *in-situ* TEM analysis to consider the above questions and gain fundamental understandings. We construct an electrochemical circuit of 50 nm-thick 2D Si as a working electrode (mounted on Pt) and Li/Li_2O as a solid electrolyte/counter electrode (mounted on W) similar to previous studies (Fig. 3a). During the first lithiation of polycrystalline 2D Si (Fig. 3d), it showed rather anisotropic changes in lateral and vertical ways (Fig. 3e). The lateral dimension of fully lithiated 2D Si expanded only 9.7%, which suggests that change in their thickness would be much larger, considering the formation of $Li_{15}Si_4$ phase in electron diffraction pattern (inset of Fig. 3d). Afterwards, delithiation starts from near edges of 2D Si to Li/Li_2O. As Li^+ is extracted from the lithiated 2D Si, evident wrinkles were formed on 2D Si and this unusual buckling caused the detachment of particle from the mounting electrode at the final stage of delithiation.

During the lithiation, decided by the atomic structure, the polycrystalline Si undergoes isotropic expansion in atomic scale [39], which is ~155% in each orthotropic direction (~370% in volume). However, since the volume change of the carbon upon lithiation can almost be ignored compared to that of Si, the carbon coatings strongly constrain the expansion of the 2D Si in the plane upon lithiation, resulting the lateral dimension of fully lithiated 2D Si expanded only 9.7%, as mentioned above. Therefore, unlike most nanostructures of Si which undergo degradation and pulverization upon lithiation, the coated 2D Si are compressed, which restrains the crack propagation and make the materials very hard to fracture during the charging process, as shown in Fig. 3i. This also explains the little lower specific capacity of coated 2D Si compared to the bare one, as in Fig. S10, because the strain energy caused by the compression rises up the chemical potential and restrain the diffusion of lithium ions [40].

With the tremendous difference of elastic modulus between the carbon coating and the Li_xSi, it is very easy for the compressed lithiated Si to reach the yield strength ($\sigma_Y = 1\mathrm{GPa}$) and consequently to flow plastically to the thickness direction. This plastic flow in thickness combined with the in-plane compression contributes to the “anisotropic expansion” overall of the 2D Si upon lithiation, which is that the ~370% volume expansion almost goes to the thickness direction rather than in plane, as mentioned above.

However, since the overall “anisotropic expansion” changes nothing with the atomic structure of lithiated Si and consequently its isotropy, then upon delithiation, the Li_xSi still shrinks ~155% in each orthotropic direction. Recalling that the in-plane expansion upon lithiation is only ~110%,

this means the delithiated 2D Si is smaller in plane than its original configuration. Since the carbon coating is nearly unchanged during the lithiated/delithiated cycles, this mismatch deformation between the 2D Si and its coating results in the tension in the former but compression in the latter. For a thin film, like the carbon coating, a compression condition is unstable, which means it is very easy for it to reach the critical strength, then buckle, and therefore release the strain energy of the whole system. The buckling forms wavy structures on the surfaces. These wrinkles reduce the compression in the coating layer, and also the tension in the delithiated Si, which makes the latter in a safer mode.

Theoretically, if we ignore the influence of the kinetic process and plastic flow on the strain energy and consider the wrinkle pattern in a 1D sinusoidal case, as shown in Fig. 3g, then the deflection is $w = A\cos(kx_1)$, where A is the amplitude and k is the wave number. When the compressed membrane force exceeds the critical value, $\left|N_1^0\right| > h\bar{E}f$, the strain energy of the whole system release to $U = U_0 - \frac{1}{2}h\bar{E}\left(\left|N_1^0\right|/(h\bar{E}) - f\right)^2$, where U_0 is the strain energy in the unbuckled state, $\bar{E}$ relates to the Young's modulus and Poisson's ratio of the carbon coating.[41] Here f is a function of the wave number, k, and also relates to the geometry and mechanical properties of both the carbon coating and Li_xSi.

To further validate the mechanism above, we set up chemo-mechanical mode to simulate the lithiation/delithiation in the coated 2D Si, which takes chemical and elato-plastic deformation into account [42, 43]. As in figure 4-3f and h, our simulation shows that no matter in 2D or 3D cases, and where the lithium sources are, the mismatch of deformation between the coating and Li_xSi always leads to the wavy structures after delithiation. In figure 4-4, we simulated the real condition of the lithiation/delithiation in coated and bare Si nanosheets. Our simulation validates the mechanism discussed above. The system of coated 2D Si shows "anisotropic expansion" overall, as shown in Figure 4-4d. The first principal stress, the positive value of which propagate the crack growth, is much larger in bare Si than in the coated during lithiation. Figure 4-4 also shows much smaller in-plane expansion of coated Si than that of the bare one.

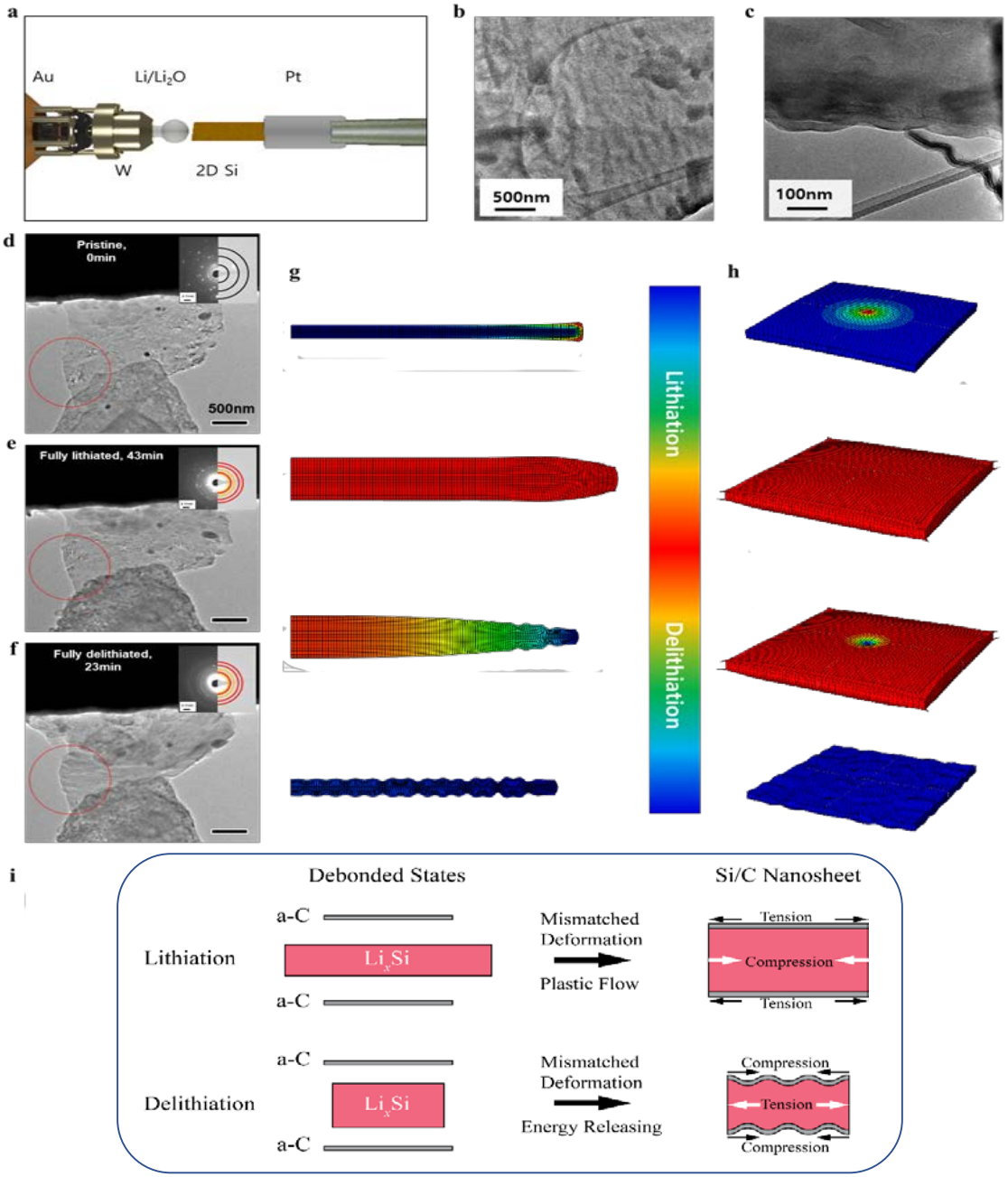

Figure 6-3. *in-situ* TEM characterization of 2D Si and its electrochemical behavior. (a) Schematization of in situ TEM cell. (b) Top-view and (c) Side-view of ex situ TEM images. (d-f) Time-variant captured images of in situ TEM video: pristine, 1st full lithiated state and 1st full delithiated state of 2D Si@C, respectively. The modeling of (g) horizontal and (h) longitudinal lithiation/delithiation behavior of 2D Si@C. (i) The sketch of mechanism on how mismatched deformation influence on the stress state in 2D Si@C during lithiation/delithiation process, which is compared to the imaginary debonded states.

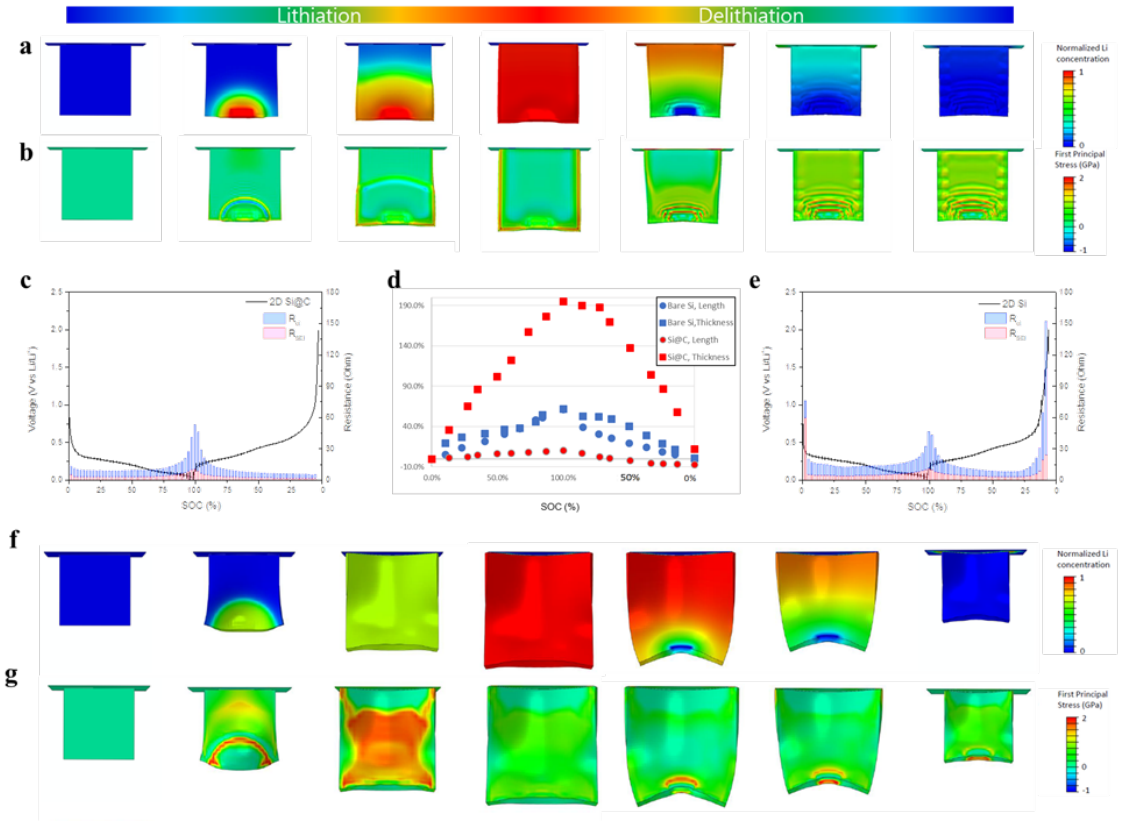

Figure 6-4. Comparison between 2D Si@C (a-d) and bare 2D Si (d-f) by the chemomechanical modelling and *in situ* EIS analysis during 1st lithiation/delithiation. A group of the lithium concentration of (a) 2D Si@C, (f) bare 2D Si and the first-principle stress of (b) 2D Si@C, (g) bare 2D Si and in situ EIS results of (c) 2D Si@C, (e) bare 2D Si during lithiation and delithiation process. (d) The change in dimensional figures versus SOC calculated from the modeling.

6.4 Conclusion

2D Si@C was simply synthesized through the cost-effective method with the variation of thickness *via* easy controls from 50 to 380nm. Based on the low surface area-to-volume ratio (~10m^2 g^{-1}), ICE value is the highest among the nanostructured 2D Si reported previously and delivered reversibly over 85% of initial charge capacity even at a 0.5 C rate. The electrochemical results were well reflected in the material design which had micro-scaled length in lateral and nano-scaled thickness in vertical. in addition, 2D Si@C also showed the unique mechano-electrochemical behaviors such as volume change, elasticity, and dimension on delithiation. It is proved that the expanded lithium silicide had a wrinkled surface after delithiation by *in-situ* TEM and computational study, while bare 2D Si maintained an initial morphology with cracks. Based on the modeling of 2D Si@C, we can calculate the morphology change, lithium concentration and stress distribution during cycles as a function of SOC. The normalized stress of 2D Si@C was standardized downward compared to bare 2D Si due to the kinetics and structural difference. Moreover, the real-time impedance during cycle was obtained to understand the relationship between the cell resistance and stress relief of silicon. In conclusion, as the wrinkled sheet was made from the difference of mechano-electrochemical properties during delithiation, lithiation-induced stress can be release into the structural evolution, leading fast kinetics.

6.5 Reference

1. M. Armand, J.-M. T., Building better batteries. *Nature* **2008,** *451* (7), 652-657.
2. Whittingham, M. S., Materials challenges facing electrical energy storage. *Mrs Bulletin* **2008,** *33* (4), 411-419.
3. Jeong, G.; Kim, Y.-U.; Kim, H.; Kim, Y.-J.; Sohn, H.-J., Prospective materials and applications for Li secondary batteries. *Energy & Environmental Science* **2011,** *4* (6), 1986.
4. Goodenough, J. B., Evolution of Strategies for Modern Rechargeable Batteries. *Accounts of Chemical Research* **2013,** *46* (5), 1053-1061.
5. Kim, H.; Seo, M.; Park, M. H.; Cho, J., A critical size of silicon nano-anodes for lithium rechargeable batteries. *Angewandte Chemie* **2010,** *49* (12), 2146-9.
6. Magasinski, A.; Dixon, P.; Hertzberg, B.; Kvit, A.; Ayala, J.; Yushin, G., High-performance lithium-ion anodes using a hierarchical bottom-up approach. *Nature materials* **2010,** *9* (4), 353-8.
7. Choi, S.; Kim, J.; Hwang, D. Y.; Park, H.; Ryu, J.; Kwak, S. K.; Park, S., Generalized Redox-Responsive Assembly of Carbon-Sheathed Metallic and Semiconducting Nanowire Heterostructures. *Nano letters* **2016,** *16* (2), 1179-85.
8. Ji, L.; Tan, Z.; Kuykendall, T.; An, E. J.; Fu, Y.; Battaglia, V.; Zhang, Y., Multilayer nanoassembly of Sn-nanopillar arrays sandwiched between graphene layers for high-capacity lithium storage. *Energy & Environmental Science* **2011,** *4* (9), 3611.
9. Li, J.; Dahn, J. R., An In Situ X-Ray Diffraction Study of the Reaction of Li with Crystalline Si. *Journal of The Electrochemical Society* **2007,** *154* (3), A156.
10. Xiao Hua Liu, L. Z., Shan Huang, Scott X. Mao, Ting Zhu, Jian Yu Huang, Size-Dependent Fracture of Silicon Nanoparticles During Lithiation. *ACS nano* **2012,** *6* (2), 1522–1531.
11. Song, J.; Zhou, M.; Yi, R.; Xu, T.; Gordin, M. L.; Tang, D.; Yu, Z.; Regula, M.; Wang, D., Interpenetrated Gel Polymer Binder for High-Performance Silicon Anodes in Lithium-ion Batteries. *Advanced Functional Materials* **2014,** *24* (37), 5904-5910.
12. Chan, C. K.; Peng, H.; Liu, G.; McIlwrath, K.; Zhang, X. F.; Huggins, R. A.; Cui, Y., High-performance lithium battery anodes using silicon nanowires. *Nature nanotechnology* **2008,** *3* (1), 31-5.
13. Wu, H.; Chan, G.; Choi, J. W.; Ryu, I.; Yao, Y.; McDowell, M. T.; Lee, S. W.; Jackson, A.; Yang, Y.; Hu, L.; Cui, Y., Stable cycling of double-walled silicon nanotube battery anodes through solid-electrolyte interphase control. *Nature nanotechnology* **2012,** *7* (5), 310-5.
14. Yu, C.; Li, X.; Ma, T.; Rong, J.; Zhang, R.; Shaffer, J.; An, Y.; Liu, Q.; Wei, B.; Jiang, H.,

Silicon Thin Films as Anodes for High-Performance Lithium-Ion Batteries with Effective Stress Relaxation. *Advanced Energy Materials* **2012,** *2* (1), 68-73.

15. Bok, T.; Choi, S.; Lee, J.; Park, S., Effective strategies for improving the electrochemical properties of highly porous Si foam anodes in lithium-ion batteries. *J. Mater. Chem. A* **2014,** *2* (34), 14195-14200.
16. Scrosati, B.; Hassoun, J.; Sun, Y.-K., Lithium-ion batteries. A look into the future. *Energy & Environmental Science* **2011,** *4* (9), 3287.
17. Yoon, T.; Bok, T.; Kim, C.; Na, Y.; Park, S.; Kim, K. S., Mesoporous Silicon Hollow Nanocubes Derived from Metal-Organic Framework Template for Advanced Lithium-Ion Battery Anode. *ACS nano* **2017,** *11* (5), 4808-4815.
18. Ryu, J.; Hong, D.; Shin, M.; Park, S., Multiscale Hyperporous Silicon Flake Anodes for High Initial Coulombic Efficiency and Cycle Stability. *ACS nano* **2016,** *10* (11), 10589-10597.
19. Choi, N.-S.; Yew, K. H.; Lee, K. Y.; Sung, M.; Kim, H.; Kim, S.-S., Effect of fluoroethylene carbonate additive on interfacial properties of silicon thin-film electrode. *Journal of Power Sources* **2006,** *161* (2), 1254-1259.
20. Ryu, J.; Hong, D.; Choi, S.; Park, S., Synthesis of Ultrathin Si Nanosheets from Natural Clays for Lithium-Ion Battery Anodes. *ACS nano* **2016,** *10* (2), 2843-51.
21. Kasavajjula, U.; Wang, C.; Appleby, A. J., Nano- and bulk-silicon-based insertion anodes for lithium-ion secondary cells. *Journal of Power Sources* **2007,** *163* (2), 1003-1039.
22. Zhang, S., Chemomechanical modeling of lithiation-induced failure in high-volume-change electrode materials for lithium ion batteries. *npj Computational Materials* **2017,** *3* (1).
23. Xiao, X.; Song, H.; Lin, S.; Zhou, Y.; Zhan, X.; Hu, Z.; Zhang, Q.; Sun, J.; Yang, B.; Li, T.; Jiao, L.; Zhou, J.; Tang, J.; Gogotsi, Y., Scalable salt-templated synthesis of two-dimensional transition metal oxides. *Nature communications* **2016,** *7*, 11296.
24. A.A. Sirenkoa, J. R. F., I.A. Akimov, X.X. Xi, S. Ruvimov, Z. Liliental-Weber, In situ Raman scattering studies of the amorphous and crystalline Si nanoparticles. *Solid State Communications* **2000,** *113*, 553-558.
25. McDowell, M. T.; Lee, S. W.; Harris, J. T.; Korgel, B. A.; Wang, C.; Nix, W. D.; Cui, Y., In situ TEM of two-phase lithiation of amorphous silicon nanospheres. *Nano letters* **2013,** *13* (2), 758-64.
26. McDowell, M. T.; Ryu, I.; Lee, S. W.; Wang, C.; Nix, W. D.; Cui, Y., Studying the kinetics of crystalline silicon nanoparticle lithiation with in situ transmission electron microscopy. *Advanced materials* **2012,** *24* (45), 6034-41.
27. Xu, K.; Ben, L.; Li, H.; Huang, X., Silicon-based nanosheets synthesized by a topochemical reaction for use as anodes for lithium ion batteries. *Nano Research* **2015,** *8* (8), 2654-2662.

28. Wan, J.; Kaplan, A. F.; Zheng, J.; Han, X.; Chen, Y.; Weadock, N. J.; Faenza, N.; Lacey, S.; Li, T.; Guo, J.; Hu, L., Two dimensional silicon nanowalls for lithium ion batteries. *J. Mater. Chem. A* **2014,** *2* (17), 6051-6057.
29. Fu, K.; Yildiz, O.; Bhanushali, H.; Wang, Y.; Stano, K.; Xue, L.; Zhang, X.; Bradford, P. D., Aligned carbon nanotube-silicon sheets: a novel nano-architecture for flexible lithium ion battery electrodes. *Advanced materials* **2013,** *25* (36), 5109-14.
30. Kim, W. S.; Hwa, Y.; Shin, J. H.; Yang, M.; Sohn, H. J.; Hong, S. H., Scalable synthesis of silicon nanosheets from sand as an anode for Li-ion batteries. *Nanoscale* **2014,** *6* (8), 4297-302.
31. Ko, Y.; Hwang, C.; Song, H.-K., Investigation on silicon alloying kinetics during lithiation by galvanostatic impedance spectroscopy. *Journal of Power Sources* **2016,** *315*, 145-151.
32. Lee, J.-I.; Ko, Y.; Shin, M.; Song, H.-K.; Choi, N.-S.; Kim, M. G.; Park, S., High-performance silicon-based multicomponent battery anodes produced via synergistic coupling of multifunctional coating layers. *Energy Environ. Sci.* **2015,** *8* (7), 2075-2084.
33. Ko, M.; Chae, S.; Ma, J.; Kim, N.; Lee, H.-W.; Cui, Y.; Cho, J., Scalable synthesis of silicon-nanolayer-embedded graphite for high-energy lithium-ion batteries. *Nature Energy* **2016,** *1* (9), 16113.
34. Liu, X. H.; Wang, J. W.; Huang, S.; Fan, F.; Huang, X.; Liu, Y.; Krylyuk, S.; Yoo, J.; Dayeh, S. A.; Davydov, A. V.; Mao, S. X.; Picraux, S. T.; Zhang, S.; Li, J.; Zhu, T.; Huang, J. Y., In situ atomic-scale imaging of electrochemical lithiation in silicon. *Nature nanotechnology* **2012,** *7* (11), 749-56.
35. Shi, L.; Chen, K.; Du, R.; Bachmatiuk, A.; Rummeli, M. H.; Priydarshi, M. K.; Zhang, Y.; Manivannan, A.; Liu, Z., Direct Synthesis of Few-Layer Graphene on NaCl Crystals. *Small* **2015,** *11* (47), 6302-8.
36. Wang, B.; Jin, P.; Yue, Y.; Ji, S.; Li, Y.; Luo, H., Synthesis of NaCl single crystals with defined morphologies as templates for fabricating hollow nano/micro-structures. *RSC Advances* **2015,** *5* (7), 5072-5076.
37. Liu, X. H.; Zheng, H.; Zhong, L.; Huang, S.; Karki, K.; Zhang, L. Q.; Liu, Y.; Kushima, A.; Liang, W. T.; Wang, J. W.; Cho, J. H.; Epstein, E.; Dayeh, S. A.; Picraux, S. T.; Zhu, T.; Li, J.; Sullivan, J. P.; Cumings, J.; Wang, C.; Mao, S. X.; Ye, Z. Z.; Zhang, S.; Huang, J. Y., Anisotropic swelling and fracture of silicon nanowires during lithiation. *Nano letters* **2011,** *11* (8), 3312-8.
38. Lee, S. W.; McDowell, M. T.; Choi, J. W.; Cui, Y., Anomalous shape changes of silicon nanopillars by electrochemical lithiation. *Nano letters* **2011,** *11* (7), 3034-9.
39. Yang, H.; Huang, S.; Huang, X.; Fan, F.; Liang, W.; Liu, X. H.; Chen, L.-Q.; Huang, J. Y.; Li,

J.; Zhu, T., Orientation-dependent interfacial mobility governs the anisotropic swelling in lithiated silicon nanowires. *Nano letters* **2012,** *12* (4), 1953-1958.

40. Chen, T.; Yang, H.; Li, J.; Zhang, S., Mechanics of electrochemically driven mechanical energy harvesting. *Extreme Mechanics Letters* **2017,** *15* (Supplement C), 78-82.
41. Huang, Z.; Hong, W.; Suo, Z., Nonlinear analyses of wrinkles in a film bonded to a compliant substrate. *Journal of the Mechanics and Physics of Solids* **2005,** *53* (9), 2101-2118.
42. Yang, H.; Fan, F.; Liang, W.; Guo, X.; Zhu, T.; Zhang, S., A chemo-mechanical model of lithiation in silicon. *Journal of the Mechanics and Physics of Solids* **2014,** *70*, 349-361.
43. Chen, T.; Zhao, P.; Guo, X.; Zhang, S., Two-Fold Anisotropy Governs Morphological Evolution and Stress Generation in Sodiated Black Phosphorus for Sodium Ion Batteries. *Nano letters* **2017,** *17* (4), 2299-2306.

Acknowledgement

이 학위를 받기까지 저를 항상 올바르게 지도해주신 박수진 교수님께 먼저 감사의 말씀을 전합니다. 부족한 저에게 이 학위는 저를 좋은 곳으로 안내해주리라 생각합니다. 이 학교를 나가서도 교수님의 그 연구자세와 인간미를 꼭 본받고 실천하겠습니다. 학위를 하는 동안 같이 진심으로 고민해주신 이상영 교수님, 송현곤 교수님, 최남순 교수님, 유자형 교수님, 곽상규 교수님, 김광수 교수님께 감사를 표합니다. 교수님들께 지식과 기술을 배울 수 있어서 즐겁게 할 수 있었습니다. 그리고 자랑스러운 Spark group 분들께 진심으로 감사합니다. 유승민 박사님 돈 많이 벌어서 밥사러 가겠습니다. 박형민 박사님 인트로 레퍼런스 221개 존경합니다. 이정인 박사님, 가정과 일 모두 잘해내시는 것이 정말 대단합니다. 신호형! 항상 최고였어요. 여자문제만 빼면요. 지금 같이 뭔가 할 수 있다면 재밌을 것 같은데, 지난 시간이 아쉽네요. 찬훈형 결혼 축하드립니다. 시끄러운 지은이는 남자들 그만 괴롭히고, 더 건강한 승희는 노답. 송우진 박사(진)님, 형! 한 수 배우고 갑니다. 레전드로 남아주세요. 같이 일을 못해서 아쉽네요. 명수야 골인하길 바란다! 성공할거야. 재건아 같이 하던 일을 마무리 못하고 가서 굉장히 미안하다. 자주 연락하자. 동기는 음..???? 규쨩 노답. 성희야 얼른 건강해지고 잘 마무리해, 큰성짝성우영tjrrmsdl영주노답.

또한 실리콘애노드를 같이 고민해준 동료들에게도 감사의 마음을 전합니다. 성주, Jeena, 지민, 치현, 태승, 세훈, 수환, 명준. 덕분에 즐겁게 일 할 수 있었습니다. 연구실 생활을 즐겁게 해준 축구인에게도 감사인사를 드립니다. 칼바람팟, 배그팟 모두 감사합니다.

마지막으로 가장 큰 힘이 되어준 우리 가족에게 이 고마움을 평생 갚으며 살아가겠습니다. 복태수 드림.